Electric Micromotor with Integrated Rotor Motion Sensors

by

Eckart Werner Jansen

B.S., Carnegie Mellon University (1988)
S.M., Massachusetts Institute of Technology (1990)
E.E., Massachusetts Institute of Technology (1991)

Submitted to the Department of
Electrical Engineering and Computer Science
in Partial Fulfillment of the Requirements
for the Degree of

Doctor of Philosophy

at the

MASSACHUSETTS INSTITUTE OF TECHNOLOGY

February 1996

©1996 Massachusetts Institute of Technology. All rights reserved.

Signature of Author ....
Department of Electrical Engineering and Computer Science
September 19, 1995

Certified by ....
Professor Jeffrey H. Lang
Thesis Supervisor

Accepted by ....
Frederic R. Morgenthaler
Chairman, Departmental Committee on Graduate Students

MASSACHUSETTS INSTITUTE
OF TECHNOLOGY

APR 11 1996

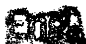

LIBRARIES

Electric Micromotor with Integrated Rotor Motion Sensors

by

Eckart Werner Jansen

Submitted to the Department of Electrical Engineering and Computer Science on September 19, 1995 in partial fulfillment of the requirements for the degree of Doctor of Philosophy in Electrical Engineering.

Abstract

In this thesis, optical sensors are integrated beneath the rotor of an electric micromotor to allow continuous real-time measurement of rotor motion. As the rotor moves under illumination its shadow modulates a photocurrent through embedded photodiode sensors. The resulting photocurrents are amplified and filtered by off-chip electronics before passing through an algorithm which extracts rotor position in time. A position measurement resolution of 1.1° at speeds up to 15000 rpm is demonstrated. Repeated acceleration from 0 rpm to 15000 rpm over 1 ms time periods is observed in gas jet driven rotors. The effects of rotor sticking are observed and characterized. Motion measurement of gas jet driven and gas levitated electrically excited rotors is shown. Excitation modes observed with the integrated sensors include forward stepping rotor motion, rotor breaking/clamping, and binary shuttering. A new design for high speed drive, motor control logic, and processing electronics is presented.

A new micromotor fabrication process is also developed to incorporate electronic devices with the associated passivation and shielding requirement needed to obtain useful signals from sensors operating in close proximity to stators switching at 100 volt electrical drive magnitudes in millisecond time frames. Motor bearing designs and processing techniques are furthered. A new type of bearing known as the flange-collar pin bearing is designed, fabricated, and tested. The results of fabrication attempts to incorporate new bearing materials: low stress silicon-rich nitride, gold, and selective tungsten are presented. The micromotor post-processing release step is improved for higher device yields through the use of hydrocarbon rinses.

Thesis Supervisor: Jeffrey H. Lang
Title: Professor of Electrical Engineering

Acknowledgements

The completion of this thesis was made possible with an enormous amount of support, patience, and encouragement I received from my family, friends, and colleagues. I would first like to thank my family, Werner, Ingrid, Richard, Petra, and Ann (Redsten) Jansen, for their love and encouragement. Your being there has made my journey up this mountain a wonderful experience.

I would like to acknowledge my thesis advisor Jeffrey Lang for his extraordinary level of support and patience as I progressed through this project. The freedom you gave me to pursue my own ideas allowed this work to become a true success. Thank you to thesis readers Martin Schmidt and Stephen Senturia for insightful comments and enthusiasm. Thank you to the rest of the EECS faculty and staff. Your guiding light continues to motivate me toward higher levels of awareness. Thanks especially to Markus Zahn, James Melcher, Ronald Parker, Jin Au Kong, Peter Hagelstien, Abraham Bers, Harold Edgerton, Eric Ippen, and Hermann Haus.

Thanks to Lee Tavrow, Stephen Bart, Mehran Mehregany, Keren Deng, and Vijay Dhuler for teaching me about the world of micromotors and for conversations on fabrication and testing. Thank you to David Volfson for gold bearing fabrication and processing assistance, Tony Amicangioli for the MMCAS system, David Leip for the capacitive sensing studies, and Daniel Gruhl for assisting with the stroboscopic measurements. Thank you to Malcolm Hathaway at ULVAC Technologies for providing selective tungsten processing and the associated SEMs.

A warm thank you to all my friends at MIT for being there through thick and thin. I especially thank Vern Shrauger for his unwavering friendship and support throughout the years. Thank you to Tony Amicangioli and Randall Pflueger for being great buddies. Thanks all everyone in DMSE and LEES for the great times. Thanks to the residents of East Campus 3E for providing a wonderful home for the past six years. Thank you to all the GRTs, housemasters, and the folks at RCA for many memorable experiences.

A large amount of recognition is deserved by the people who made it all work in practice, the MTL and Microlab staffs. Thanks especially to Pat Burkhart for your terrific ability to manage research lots. Thank you to our lab director Linus Cordes for your support. Thanks to everyone else, past and present, Dan Adams, Bernard Alamariu, Jim Bishop, Rob Cuikay, Joe DiMaria, Brian Foley, Octavio Hurtado, Rudy Lia, Jr., Velma McClure, Paul McGrath, Richard Perilli, Nestore Polce, Paul Tierney, Tim Tyson, David Volfson, Joe Walsh, Dick Westerberg, and Carrie Young. You are all wonderful people and I wish you the best.

This work was supported by the U.S. National Science Foundation under grant 9109343-ECS. Additional support was received through Corning Glass Fellowship, Harold Edgerton Fellowship, and ARPA contract J-FBI-92-196. All motor fabrication was performed in the Integrated Circuits Laboratory and Research Group Laboratories of the Microsystems Technology Laboratories at MIT. Selective tungsten bearings were deposited at ULVAC Technologies, Inc. (Andover, MA). Fabrication

of the gold bearings was performed in the MIT Microlab. Stroboscopic testing was performed in the MIT Strobe Lab.

Contents

1 Introduction **13**

1.1 Motivation and Goals 13

1.2 Background 14

1.2.1 Micromotors 14

1.2.2 Integrated Sensors 20

1.3 Overview of Thesis 21

2 Integrated Sensors **25**

2.1 Motion Sensing Techniques 25

2.1.1 Stroboscopic Dynamometry 25

2.1.2 Stator $v - i$ Sensing 27

2.1.3 Rotor Capacitance Sensing 29

2.1.4 Rotor Optical Sensing 32

2.2 Integrated Photodiode Sensors 34

2.2.1 Sensitivity 35

2.2.2 Response Speed 37

2.2.3 Noise 38

2.2.4 Position Extraction Algorithm 39

2.2.5 Signal Conditioning and Control Circuitry 41

3 Design and Fabrication **49**

3.1 Theory of Operation 49

3.2 Fabrication 53

3.3 Design and Process Improvements 61

3.3.1 Sensor Implant Thermal Processing Effects 62

3.3.2 Surface Passivation and Threshold Voltage Shift 63

3.3.3 Electrical Shielding 66

3.3.4 Gap Plug 67

3.3.5 Flange-Collar Pin Bearing Design 69

3.3.6 Post-Processing Release 74

3.3.7 Bearing Materials 80

4 Testing **85**

4.1 Overview 85

4.2 Photodiode Characterization 87

4.2.1 Diode IV response to AC modulated light source 87

4.2.2 Quantum efficiency 87

4.2.3 Ideality Factor 93

4.2.4 Reverse breakdown voltage 95
4.3 Time Response to a Strobed Light Source 97
4.4 Static Rotor Position Measurement 99
4.5 Sensor Response in Presence of Stator Switching 101
4.6 Motion of Gas Jet Driven Rotor without Electric Drive 105
4.7 Motion of Gas Jet Driven Rotor with Electric Drive 110
4.8 Motion of an Electrically Driven Rotor 114

5 Summary, Conclusions, and Future Work 119
5.1 Summary 119
5.2 Conclusions 122
5.3 Suggestions for Future Work 125

A Fabrication Process 129
A.1 Process Traveler 130
A.2 Photolithography 137
A.3 Wet Etches 137
A.3.1 7:1 Buffered Oxide Etch 137
A.3.2 Silicon-Rich Silicon Nitride Etch 138
A.3.3 RCA Clean 138
A.3.4 Piranha Clean 138
A.3.5 HF Release Etch 138
A.4 Dry Etches 139
A.4.1 Isotropic Polysilicon Etch 139
A.4.2 Anisotropic Polysilicon Etch 139
A.4.3 Anisotropic Oxide Etch 140
A.5 Diffusion, Oxidation, and Deposition 140

B SUPREM-III Model 149

C Capacitance Matrix Extraction from FASTCAP 153

D Computer Software 161
D.1 SENSOR.C 161
D.2 POSTCAP.C 172

References 179

List of Figures

1.1 Electric micromotor with integrated photodiode motion sensors. . . . 15

2.1 Stroboscopic dynamometry measurement technique. 27
2.2 Lumped parameter rotor capacitance sensing model for a micromotor. 29
2.3 Photograph of macroscopic capacitive sensing model. 31
2.4 Macromodel capacitance as a function of rotor position. 32
2.5 Solid model and conductor assignment for FASTCAP capacitance extraction in the micromotor. 33
2.6 FASTCAP with POSTCAP solution to capacitance between two opposing sensors as a function of rotor position in the micromotor model. 34
2.7 Flowchart of the position extraction algorithm. 40
2.8 Simulated sensor data having arbitrarily offset sinusoidal signals, arbitrary amplitude and added random noise. 42
2.9 Three computed angle positions for simulated sensor data. 43
2.10 Computed position average for simulated sensor data. 44
2.11 Schematic of off-chip sensor amplification, filter, and drive circuit . . 47

3.1 Cross-section of typical micromotor 50
3.2 Fabrication process. 54
3.3 Continued fabrication process. 55
3.4 Layout of a typical micromotor with sensors. 56
3.5 Layout of an entire micromotor mask layer. 57
3.6 SUPREME-III concentration before and after processing motor . . . 64
3.7 SEM of sensor interconnect showing shielding. 68
3.8 Oxide plug seals the rotor-stator gap before bearing material deposition. 71
3.9 Cross-section of a conventional unreleased hemispherical micromotor bushing. 72
3.10 Micromotor bearing designs. 72
3.11 Rotor underside with flange-collar pin bearing exhibiting dimple protrusions. 73
3.12 Sticking modes I and II. 76
3.13 Release yield in singly-clamped polysilicon cantilever beams exhibiting both mode I and mode II sticking. 77
3.14 Release yield in singly-clamped polysilicon cantilever beams exhibiting only mode II sticking. 78
3.15 Release yield in doubly-clamped polysilicon beams exhibiting only mode II sticking. 79
3.16 Silicon-rich silicon nitride bearings. 81
3.17 Gold bearings fabricated by a lift-off technique. 82

3.18 Incomplete bearing step coverage by e-beam evaporated gold. 83
3.19 Experimental selective tungsten bearings. 84

4.1 Plan view of motor and sensors for testing probe locations. 86
4.2 Photodiode $i - v$ response under incandescent AC light illumination. 91
4.3 Photocurrent measurement under HeNe laser illumination. 92
4.4 Equivalent circuit for the four layer dielectric film to the photosensitive junction. 92
4.5 Forward biased i–v characteristic of unilluminated sensor 94
4.6 Unilluminated photodiode i-v characteristic shows the onset of reverse breakdown at approximately -19V. The sharp negative current increase near -38 V occurs as the field region expands the diode area under the bonding pad though inversion. 96
4.7 Sensor and amplification circuit response to a strobed light signal . . 98
4.8 Sensor measured rotor angle position compared to protractor video recorded position 100
4.9 Four sensor responses to drive interference 103
4.10 Level-shift interference in sensor signal from stator drive 104
4.11 Sensor signals from nitrogen jet driven rotor. 106
4.12 Rotor motion in time for a nitrogen jet driven motor. 107
4.13 Rotor motion in time for a nitrogen jet driven motor. 108
4.14 Rotor motion in time for nitrogen jet driven motor showing sticking. . 109
4.15 Sensor data of a gas jet driven rotor in the presence of 100 V electric drive. 111
4.16 Motion of a gas jet driven rotor in the presence of 100 V stator electric drive where gas jet motive forces dominate electric drive forces. . . . 112
4.17 Braking and clamping by electric forces in a gas jet driven rotor. . . . 113
4.18 Rotor motion due to electrical excitation with binary shuttering motion. 115
4.19 Forward electrical stepping motion in a nitrogen gas jet levitated motor. 116
4.20 Reverse electrical stepping motion in a nitrogen gas jet levitated motor. 117

5.1 System level configuration of electric micromotor closed-loop position control. 127

C.1 Five electrode system. 154
C.2 Five concentric spherical conducting shells in free space. 158
C.3 POSTCAP run of five concentric shells example from exact analytical solution (in FASTCAP form). 160

List of Tables

2.1 Comparison of four motion sensing techniques. 26
2.2 Comparison between macroscopic model and micromotor dimensions. 30

3.1 Threshold voltage and implant parameters. 66

A.1 Standard resist coat recipe #11. 141
A.2 Standard resist develop recipe #20. 141
A.3 Isotropic SF_6 polysilicon plasma etch recipe. 142
A.4 Anisotropic SF_6 polysilicon plasma etch recipe. 142
A.5 Anisotropic CHF_3/CF_4 oxide plasma etch recipe. 142
A.6 220 Å dry thermal gate oxide recipe 230 in tube A2. 143
A.7 3000 Å dry-wet-dry thermal oxide recipe 114 in tube B5. 143
A.8 3000 Å LPCVD low temperature oxide (LTO) deposition recipe 430. . 144
A.9 1.0 μm LPCVD low temperature oxide (LTO) deposition recipe 432. . 144
A.10 1500 Å LPCVD polysilicon deposition recipe 423. 145
A.11 2.5 μm LPCVD polysilicon deposition recipe 427. 145
A.12 $POCl_3$ doping recipe 315 for 90 minutes. 146
A.13 $POCl_3$ doping recipe 316 for 5 hours. 146
A.14 Silicon-rich silicon nitride recipe for the vertical thermal reactor (VTR). 147

Chapter 1

Introduction

1.1 Motivation and Goals

This thesis describes the integration of optical motion sensors into an electric micromotor to allow continuous real-time measurement of rotor motion for use in precision micromotion control applications. As a consequence of their small physical dimension, micromechanical systems are dominated more by area-scaled forces than by volume-scaled forces. For this reason, micromotors have been found to be highly susceptible to load changes from particles, air currents, and mechanical agitation visible experimentally as motors skip poles or freeze momentarily [87]. Rotor motion is difficult to predict in real time because of this high dependence on static and dynamic loading. Current motion sensing techniques can only view these effects by sampling and averaging over many rotations from which detailed motion information is not available [7, 4, 59, 87]. Motion sensors operating in a closed-loop control system could improve motor performance, allow asynchronous operation, and improve velocity and torque control. The ability to sense rotor motion would permit optimal voltage phasing to increase drive torque and reduce ripple. The availability of detailed motion information would enable scientific study of motor loading effects. Accurate rotor motion sensors are therefore a necessary foundation for the development of micromotor control systems and the scientific study of micromotion.

The primary goal of this thesis is to develop the ability to extract precise real-time rotor motion information in an electrically driven micromotor. This goal involves the integration of electronic motion sensing devices operating in close proximity to high voltage switching actuator electrodes fabricated within the confines of the micromechanical process.

Secondary goals are the improvement of existing motor bearing designs, bearing fabrication techniques, bearing materials, and release processing.

1.2 Background

1.2.1 Micromotors

Electric motors create mechanical motion through the electroquasistatic force interaction between charges on rotating and stationary members. The electric motor is related to the conventional magnetic motor through a duality between the electroquasistatic and magnetoquasistatic limits of Maxwell's equations [48]. To date large electric motors have been studied but have failed to proliferate because larger gaps exhibited dielectric breakdown at lower electric field strengths limiting attainable torques in motors with traditional dimensions [92, 43]. Magnetic motors able to achieve higher magnetic field energy density variation have dominated the world of motors. Recent advances in microfabrication technology today allow the gap precision necessary to attain energy densities comparable to a magnetic motor. Sub-millimeter scale electric motors have been re-discovered as actuators for microelectromechanical systems (MEMS).

The electric micromotor shown in Figure 1.1 is a sub-millimeter scale planar actuator driven by electrostatic forces that are enhanced by micron-size gaps which are machined from silicon-based materials above a silicon substrate [25, 26, 23, 64, 67, 60, 59, 82, 83, 81, 88, 86, 87]. These micromotors have planar rotors which spin around a central bearing. The bearing overhangs its rotor to hold the rotor in place within the motor at the substrate. The micromotor has stator electrodes which encircle the rotor in its plane of motion. These electrodes are driven by external voltage phases to electrically excite the rotor, putting it into motion. Friction between the rotor and substrate is reduced through the use of dimple or collar bushings which act to minimize the rotor-to-substrate contact area. Friction between the rotor and

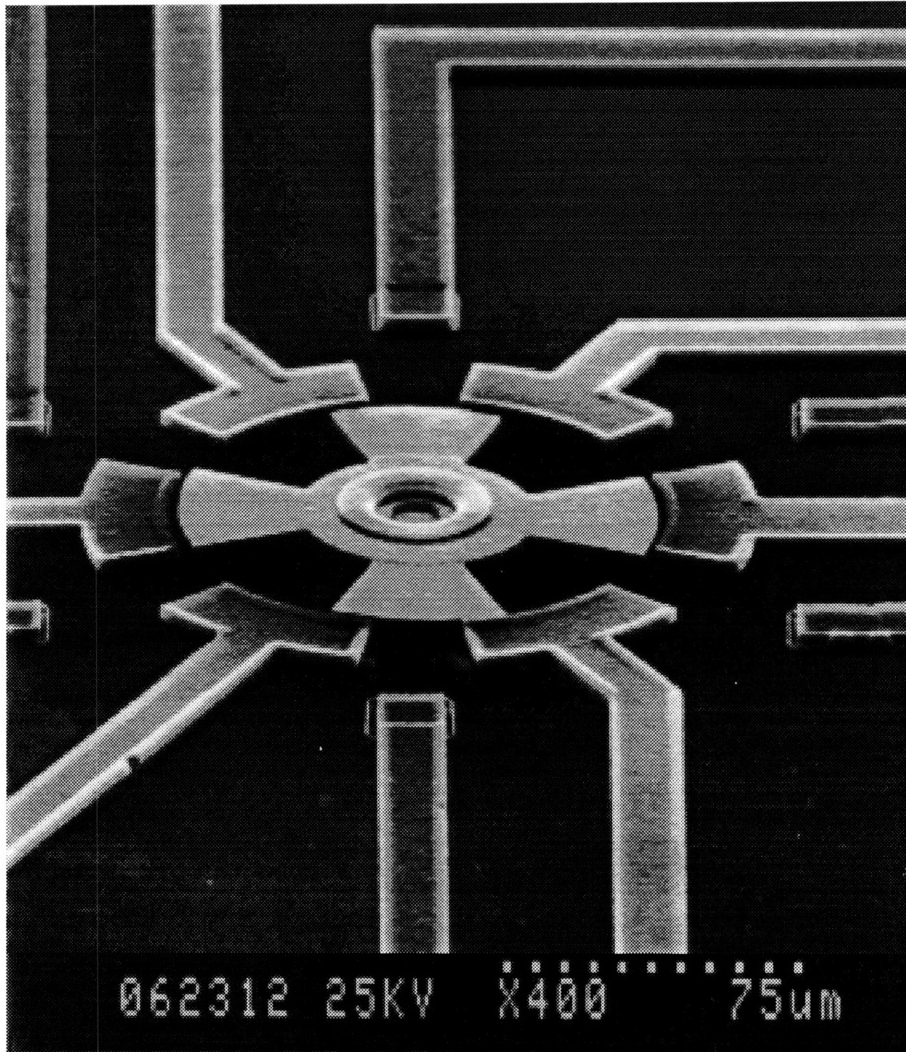

Figure 1.1: Scanning electron micrograph of an electric micromotor with integrated photodiode motion sensors beneath its rotor. Typical dimensions are rotor diameter of 100 μm, rotor thickness of 2.5 μm, and rotor-stator gap of 1.5 μm. Typical three-phase bipolar stator excitation voltage amplitudes are 70 V to 100 V.

bearing may be modified through the use of different bearing materials which act to modify the contact friction at the bearing.

Initial design considerations of micromachined electric motors [91, 5] postulated both variable-capacitance and induction drives with maximum rotor speeds in the millions of rotations per minute. The first operational micromotors were fabricated and demonstrated in 1988 at UC Berkeley by Fan [24, 26, 23] and Tai [82, 83, 81]. Soon after, operational micromotors were demonstrated at MIT by Mehregany [61, 64, 60, 59, 67] and Tavrow [88, 86, 87]. This first generation of micromotors had short operational lifetimes, and were electrically driven open-loop because integrated motion sensors were not yet available.

A robust micromotor fabrication process has evolved at MIT through the iterative improvement of the original processes. The first fabrication attempts by Lober [54, 55] showed little operational success and presented several challenges to overcome including rotor instability, thin film warpage due to intrinsic stress gradients, sticking, and fabrication complexity. The next MIT motors resulted in two different microfabrication processes by Mehregany [61, 64, 60, 59, 67] and Tavrow [88, 86, 87]. The early problems were solved through the use of less aggressive geometries and redesigns of the fabrication processes. Side-radial-drive geometries were used instead of axial-top/bottom-drive geometries. Fabrication processes were developed for multilayered resist and local oxidation of silicon (LOCOS)-based surface micromachining to increase planarity. A variety of functioning salient-pole and harmonic variable-capacitance side-drive micromotors were built and tested with the new processes. A functioning electrohydrodynamic induction pump demonstrated the motive principle of an induction micromotor [8].

Experimental studies of these micromotors showed that friction and wear pose limitations to their practical application [31, 65, 66, 59, 6, 4, 87, 84, 53, 17]. In-use rotor sticking effects were found to make open-loop motion control difficult. Accurate rotor motion sensors are therefore needed to sense friction and wear effects during rotor motion and enable their control. Friction acting as an undesirable load opposing

useful work can present a 10% to 20% load in a mechanically uncoupled motor during its acceleration compared to the frictional load of only 0.01% in conventional magnetic motors [4]. The need for lower friction material combinations and wear resistant materials became apparent.

Bart first developed the basic dynamic motor models and measurement techniques [4]. The successful operation of micromotors prompted the development of these dynamic models and measurement techniques to allow analysis of the electromechanical dynamics of variable-capacitance and induction micromotors [4, 87]. Drive torque and side-pull forces on the rotor could then be optimized in the design of motors within their fabrication limits [87]. A stroboscopic dynamometry technique was developed to experimentally measure the motion of salient-pole variable-capacitance micromotors and the resulting data was used to determine frictional torques, confirm drive torque, and determine side-pull forces [6, 4, 59, 87]. Optimized fits to the dynamic models yielded coefficients of sliding friction for polysilicon-on-polysilicon and silicon nitride-on-polysilicon [6, 4, 87]. However, the stroboscopic technique gathers sampled time-average motion transient data over several revolutions as opposed to continuous sensing over a single revolution. The detailed effects of friction can not be observed experimentally using this technique.

Micromotor research has continued internationally with the development of new motor technologies that could all be enhanced with the availability of continuous rotor motion sensing techniques. The fabrication of functional variable reluctance magnetic micromotors has been demonstrated using the LIGA technique [34] and with fully integrated stator and coils [2]. Recent magnetic micromotors incorporate micromachined nickel-iron rotors with toroidal meander-type integrated inductors to generate flux at the stator poles. These motors could exhibit torques of magnetic origin two to three orders of magnitude higher than electric micromotors [2]. Motor operation in liquid environments has been demonstrated in various hydrocarbon liquids, deionized water, and silicone lubricating oil [19, 62, 16]. Increases in motive torque were observed with the increased relative dielectric constant in the gap. A

simple fabrication process for polysilicon side-drive motors has been developed incorporating only three lithography steps allowing rapid prototyping of new motor geometries and materials [18]. On-chip high voltage generator circuits as power supplies for electrostatic micromotors have been demonstrated providing approximately 50 V output with TTL level inputs [44]. The ability of a harmonic drive micromotor to mechanically couple and drive a microreduction planar gear train module has been demonstrated giving a power output of 1μW [71]. Bottom drive axial gap wobble motors with nNm range torques have been demonstrated incorporating a ball bearing and an unobstructed side with the ability to couple to an external mechanical system [50].

The development of millimeter-scale micromotors, or millimotors, shows promise for the use of micromotors in real world applications. Continuous rotor motion sensing would provide the ability to drive these devices closed-loop. Piezoelectric ultrasonic motors using ferroelectric thin films have been demonstrated toward the realization of autonomous microrobots [29]. The application of polysilicon electric millimotors with an etched diffraction grating in a chemomechanically polished rotor has been demonstrated as an optical bar code scanner without need for an external lens system [95]. A mechanical platform for use in chip-sized high density data storage systems incorporating millimotors that drive an AFM-based recorded disk and read/write arm has been demonstrated for millimeter sized data storage devices [27].

Micromotors are fabricated using standard integrated circuit technologies by machining a silicon wafer surface and bulk. These techniques were used as early as 1967 at Westinghouse Research Laboratories where electric forces were used to mechanically resonate beams in the Resonant Gate Transistor [69]. The fabrication process described in this thesis similarly incorporates standard IC materials and processes available in the MIT Microsystems Technologies Laboratories. Deposition and etch recipes have been optimized to enable mechanical features such as high aspect ratio side-walls and thick structural films. First generation micromotor processes at MIT were restricted to strictly standard IC related processes, materials, and thicknesses

prescribed by the baseline process [89]. Standard process steps were limited to eliminate contamination by oxide permeable elements such as sodium and potassium and deep-level silicon donors such as gold and copper. Standard process steps also allowed better monitoring of equipment drift and time variation. However it was found that early micromotor processes were adversely affected by the thin 5000 Å standard polysilicon recipe which had a tendency to deflect [54, 55, 56]. Film thickness constraints were relaxed allowing more rigid structural components in the motor design. This thesis continues to advance the micromotor fabrication process by demonstrating the development of new bearing fabrication techniques and new materials. Lift-off techniques allow new bearing materials not available in the fabrication clean room such as gold to be incorporated after wafers are removed from the clean room.

In the final steps of many surface micromachining processes, a sacrificial material is removed after structures are completed. Known as release, these steps acts to produce the rigid freely-moving rotor in the micromotor. In an ideal materials system, removal of the sacrificial material does not affect the other materials by etching them or leaving etch residues on their surfaces. An optimal materials system requires films with compatible mechanical characteristics yet complimentary chemical etch characteristics. Mechanically rigid films must be stress matched to allow structures to remain unwarped after being thermally cycled during chemical vapor depositions and anneals as high as 1200°C. Isolated electrically insulating and conducting regions are required to attain multiphase electrical excitation and sensing of the rotor. As a result, a materials system for a micromotor consists of at least three materials: sacrificial, conducting, and insulating materials. With the addition of integrated electronic devices for sensors, impurity doped single crystal semiconductor materials allow integrated pn-junctions and transistors. Several possible complementary materials system combinations exist including polysilicon and silicon oxide [41, 40, 35], tungsten and oxide [13], molybdenum and aluminum [12] and epitaxial GaAs and AlGaAs [38]. The polysilicon and silicon oxide system is used in this work is a well characterized system for use in MEMS that exploits the high etch resistance of silicon

to hydrofluoric acid (HF) and the complementary etchability of silicon dioxide. HF resistant and electrically insulating silicon nitride was introduced to complement the electrical conductivity of doped polysilicon. In this thesis cantilever beam release yield is studied on different substrates. The release technique is improved through the use of hydrocarbon post-rinses.

1.2.2 Integrated Sensors

In many conventional magnetic motors, rotor position sensing and drive control are achieved through the use of mechanically commutating brushes. Brushes degrade with use and frequently need to be replaced [28], leaving excess wear material in the motor. As a consequence, devices such as shaft encoders and resolvers were developed to enable electronic commutation in conventional magnetic motors. Brush commutation is not practical in a micromotor because of fabrication complexity, friction, and wear particle generation. A variety of rotor motion sensing techniques exist which might be suitable for micromotors, including stroboscopic dynamometry, stator $v - i$ sensing, rotor capacitive sensing, and rotor optical sensing. This thesis evaluates these techniques and employs an optical sensing technique as its final implementation for rotor motion sensors.

Microfabricated sensors transduce a physical quantity into another measurable quantity such as a voltage, charge or current which may be amplified and read-out by an electronic circuit. A wide variety of microfabricated sensors exist to measure physical quantities such as pressure [73, 85, 21, 22, 33, 46, 76] shear stress [77, 78, 70], acceleration [75, 58], chemical ion concentration [9], flow rate [74, 20], vapor concentration [42], and atomic position on surfaces [3]. Photodiode sensors are used in many applications from TV remote control to optical fiber signal transmission. These sensors are illuminated p-n diodes where the reverse bias current is proportional to the illumination. As a motion sensor, a photodiode converts variations in light intensity from the shadow of a moving object into electrical variations that are amplified by external circuitry. Optical position sensing using photodiodes in a shear stress sensor

has been demonstrated [70]. The first integrated sensors to be incorporated into electrostatic micromotors were light sensitive but not able to resolve rotor motion [88]. Guckel incorporated photodiode velocity sensors into a micro-assembled magnetic LIGA-based variable reluctance motor. Photodiode sensors producing 100 mV signal swings driven with 735 nm LEDs observed magnetically actuated rotor motion at velocities up to 30000 rpm in 285 μm diameter rotors [34]. These photodiode sensors were not located in the presence of integrated high voltage switching stator electrodes.

1.3 Overview of Thesis

The thesis describes the development of integrated optical motion sensors in an electric micromotor to allow continuous real-time measurement of rotor motion for use in precision micromotion control applications and the scientific study of friction details. The primary goal of this thesis is to develop the ability to extract real-time rotor motion information in an electrically driven micromotor. This goal involves the integration of electronic motion sensing devices operating in close proximity to high voltage switching actuator electrodes fabricated within the confines of the micromechanical process. Secondary goals are the improvement of existing motor bearing designs, bearing fabrication techniques, bearing materials, and release processing.

To this end, Chapter 2 presents an analysis of four rotor motion sensing methods for potential use in micromotor systems, including stroboscopic dynamometry, stator $v - i$ sensing, rotor capacitive sensing, and optical sensing. Optical photodiode motion sensors are chosen for implementation in the micromotor fabrication process. The performance and design requirements for the integrated optical sensors are determined. Designs for off-chip sensing and control circuitry are developed in conjunction with an algorithm to determine rotor motion from the sensor signals. The challenges for real-time implementation are discussed. The chapter concludes with a specification for a sensor system to be incorporated into the fabrication process.

Chapter 3 describes the design and fabrication of an improved micromotor using a robust process that allows incorporation of electronic devices with the passivation

and shielding steps necessary to obtain useful sensor signals. The theory of micromotor operation is reviewed and the new fabrication process is described in the areas of electronics integration, surface micromachining, and post-processing release. Improvements to the micromotor design are presented including surface passivation, threshold voltage shift implants, electrical shielding layers, gap plug oxide, and new bearing fabrication.

Chapter 4 describes experimental testing of the fabricated micromotors with integrated photodiode motion sensors. The photodiode sensor sensitivity to light variations is established and device operating parameters are measured for use in signal and noise analysis. The functionality of sensors working as a group demonstrates the ability to detect static positions of the rotor. These experiments verify that each sensor is individually functioning, that the off-chip amplification and signal conditioning electronics are functioning, and that the position extraction algorithm is correct. The ability of a sensor to respond to rapid light variation in time is demonstrated. Response to strobed light pulses gives an indication of motion information acquisition bandwidth and is determined to be of sufficiently fast time resolution for subsequent motion studies. Sensor operation in the presence of switching stator drive voltages is explained. Two types of electrical switching interference are observed in the sensor signal. The first type of interference observed is a transient above-substrate capacitive coupling between the stator drive probes and sensors. The second interference is a polarity dependent level-shifting coupling to the drive voltage explained by parasitic transistor action in the device. Rotor motion driven by gas jet and electrical excitation are measured and rotor position, velocity and acceleration are quantified. Several case studies of electrical excitation are presented including electrical rotor clamping/braking, binary shutter excitation, and forward stepping motion in gas levitated motors.

In Chapter 5, the contents of the thesis are summarized. Major conclusions from the research are presented in the areas of choosing a motion sensing technique, integration of electronic photodiode devices into a micromechanical fabrication process,

shielding requirements for operation of sensors in close proximity to high voltage switching actuator electrodes, improved post-processing rotor release techniques, and preliminary fabrication methods for new bearing materials. Suggestions for future work are made toward the incorporation of sensors into closed-loop micropositioning systems.

Appendix A details the micromotor fabrication process with integrated photodiode sensors. A formal process traveler is listed with standard baseline and non-baseline operation sets used in the MIT Integrated Circuits Laboratory. The photolithography technique, wet and dry etch processing are described. Diffusion, oxidation, and deposition recipes are presented. Appendix B gives a typical SUPREM-III input file for thermal processing and threshold voltage shift studies. Appendix C gives the derivation of an alternative capacitance matrix from the capacitance extraction code FASTCAP [68], and is useful for electromechanical analyses. Appendix D lists the source code SENSOR.C for the position data extraction algorithm used to interpret the raw data of three sensor signals to give rotor position in time. The source code POSTCAP.C is listed which implements the alternative capacitance matrix formulation of Appendix C.

Chapter 2

Integrated Sensors

This chapter presents an analysis of four rotor motion sensing techniques for possible use in micromotor systems. The techniques shown in Table 2.1 are based on stroboscopic dynamometry, stator $v - i$ relations, rotor capacitance variation, and optical shadowing by the rotor. Optical photodiode motion sensors are chosen for implementation in the micromotor fabrication process. The performance and design requirements for integrated optical photodiode sensors are determined. Designs for off-chip sensing and control circuitry are developed in conjunction with an algorithm for extracting rotor motion from the sensor signals. The challenges for real-time implementation are discussed. Throughout the chapter specifications for sensor fabrication are given and are incorporated into the fabrication process in the following chapter.

2.1 Motion Sensing Techniques

2.1.1 Stroboscopic Dynamometry

Stroboscopic dynamometry shown in Figure 2.1 is performed by modifying a microprobe station light assembly to support a strobe light with an adjustable time delay. The light is triggered to flash by the on-transition of one motor drive phase. After the adjustable delay time the strobe flashes with a persistence of 3 μsec, effectively stopping the rotor motion and capturing its position in a video frame. As the adjustable delay is swept, a time-average transient of an open-loop driven motor is recorded. Afterwards, recorded video data are analyzed manually frame-by-frame by averaging the position data in several frames for each delay time. Here each video

Technique	Advantages	Disadvantages
Stroboscopic Dynamometry	No extra sensors No circuitry No rotor load	Too slow for real time control Time averaged data only Limited bandwidth due to bulb persistence
Stator $v - i$	Fewer motor leads No extra sensors No light necessary	Parasitic capacitances greater than sensor capacitance changes Reduced closed–loop robustness Electronics needed to measure $v - i$ Processing speed requirements for estimator
Rotor Capacitive	No light necessary	Pull-down forces from sense electrodes Parasitic capacitances greater than sensor capacitance changes Needs on-chip FET buffer
Rotor Optical	High bandwidth No rotor load	Requires broadcast light Device processing complexity Off-chip electronics and processing

Table 2.1: Comparison of four motion sensing techniques.

frame samples a different, but assumed identical, motor transient. Data analysis is performed using statistical methods because some sticking noise is associated with the stepping motion. Motor transients are in fact not identical over each frame so that averaging is necessary.

Nonetheless, stroboscopic dynamometry is a useful method for the measurement of salient-pole micromotor rotor open-loop motion dynamics under periodic excitation [7, 4, 59, 87]. Data of angular position in time has been taken of rotor step transients and undriven rotor spin-down. The stroboscopic technique has the primary advantage that integrated sensors and special electronic circuitry are not necessary. Since the technique is optical, it adds no extra load torque to the rotor such as from pull-down forces present in a driven-electrode capacitance sensing method. The major disadvantage of the stroboscopic technique is that data are not acquired continuously over a single revolution, rather it is sampled over many revolutions and averaged. Thus, detailed friction information is not visible through this process. The method also imposes a heavy computational burden for data analysis. For these reasons

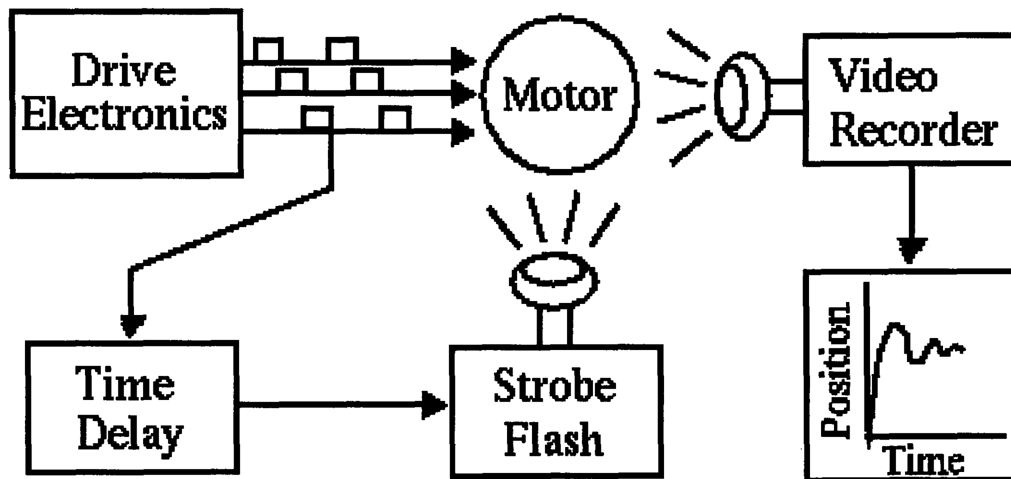

Figure 2.1: Stroboscopic dynamometry measurement technique.

stroboscopic dynamometry will not be considered further as a method for integrated rotor motion measurement.

2.1.2 Stator $v - i$ Sensing

Stator $v - i$ sensing used in a micromotor attempts to compute the rotor-stator capacitance from the terminal voltage and current measured at the stator. Under a quasistatic approximation, the rotor-stator capacitance is a function of angular rotor position and is not dependent on excitation. Assuming the rotor-stator capacitance can be measured, angular position could be estimated.

Consider, for example, a 6:4 (stator-poles:rotor-poles) micromotor as shown in Figure 1.1 traveling at 10000 rpm such that each stator undergoes 1333 phase switchings/sec. The following argument shows that voltage and current measurement noise makes the determination of the rotor-stator capacitance difficult. Assume the stator is switched from 0 V to 100 V, or 100 V to 0 V, over a time interval of 1 μsec. A current i flows onto the stator as the grounded rotor spins, moving charge to the rotor-stator capacitance C which varies between 10^{-16} F and 0 F; parasitic capacitances from interconnect to ground and probe/bonding pad to ground are on the order of 10^{-12} F. Further assume that the noise floor is approximated to be 10^{-9} A

for current measurement. Ignoring any phase resistance, the current to be measured is

$$i = v\frac{dC}{dt} + C\frac{dv}{dt} \tag{2.1}$$

First, evaluate the left term of Equation 2.1. For $v = 100$ V and the assumed variation in C of 10^{-16} F which varies eight times per revolution, with each revolution occurring in 100 μsec, the left term in Equation 2.1 evaluates to approximately 1/13 of the 10^{-9} A noise floor. Next, evaluate the right term of Equation 2.1. For $C = 10^{-16}$ F as the voltage v varies from 0 V to 100 V over 1 μsec. The right term evaluates to be equal to 10^{-8} A, which is close to the 10^{-9} A noise floor. As velocity decreases, current measurement gets worse. Since the level of current measurement can fall below the noise floor, stator $v - i$ sensing is not possible for this set of parameters.

The stator $v - i$ technique operates under the assumption that stator voltages and currents contain sufficient information from which an estimator can generate rotor position and velocity. Stator $v - i$ sensing has been successfully applied to magnetic motors obtaining cost savings by eliminating motion sensors [45, 37]. The major advantage of $v - i$ techniques in macro-scale motors are that they do not require complex motion sensors. As a result, the sensor signal lines are eliminated and only power leads enter the motor. The main disadvantage to the technique is the difficulty in distinguishing the small rotor-stator capacitance variation from the large probe and ground parasitic capacitances so close to the current noise floor. Other disadvantages of this technique are a reduction of control loop robustness through the addition of an estimator to derive position and velocity. The stability and convergence of the estimator are important, as contrasted with direct position sensing techniques where the stability of the fed back position signal is insured. Further, the estimator must run at a higher speed than the motor to insure correct and timely feedback of position information. A converter circuit is required to convert the terminal $v - i$ signals into a digital signal useful for a control circuit. Additional sensors are needed to measure the $v - i$ signals at the motor terminals. For these reasons, the stator $v - i$ technique is not considered further as a possible rotor motion sensing method.

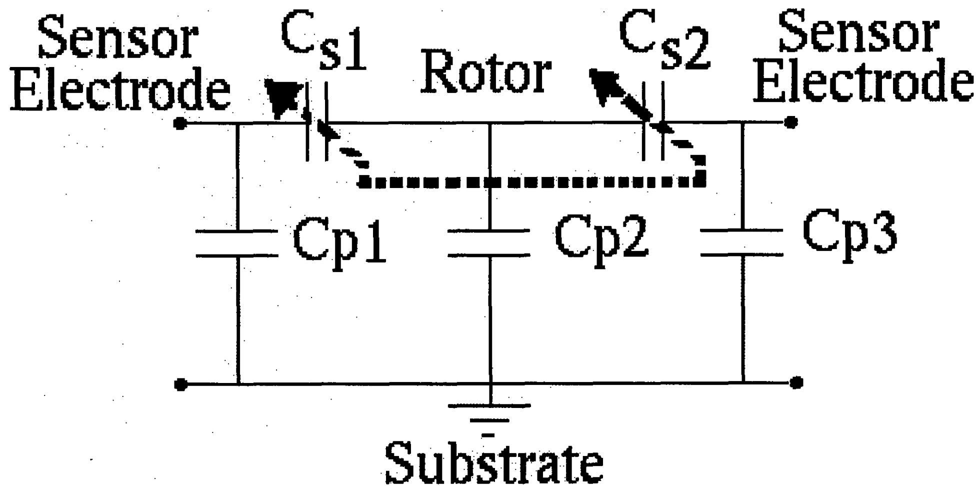

Figure 2.2: Lumped parameter rotor capacitance sensing model for a micromotor. Parasitic capacitances are represented by C_{p1}, C_{p2}, and C_{p3}. Sensor capacitances are represented by C_{s1} and C_{s2}.

2.1.3 Rotor Capacitance Sensing

Rotor motion may be measured through capacitive coupling between a moving rotor and sensor electrodes beneath the rotor. This is referred to as capacitive rotor position sensing. Capacitive sensing has been successfully used to measure displacement and motion in many micromechanical systems [78, 58, 46, 21]. In a micromotor, as the conducting rotor moves in close proximity to two integrated electrodes in the substrate beneath the rotor, the capacitance between the electrodes changes. Figure 2.2 shows a simple lumped parameter model for capacitive sensing in the micromotor. The capacitance function of position is inverted to derive position for each measured capacitance.

The capacitive rotor sensing technique was verified in a macroscopic model of a moving conducting rotor with sensor electrodes constructed to a scale approximately 3 orders of magnitude larger than a typical micromotor to demonstrate capacitive motion sensing. Figure 2.3 shows a photograph of the model and Table 2.2 gives a comparison between the macroscopic model and typical micromotor dimensions. The model was designed to have a pole count, rotor angular sweep, and sensor electrode angular sweep the same as the actual micromotor. The model rotor was constructed

Dimension	Macro–model	Micromotor	Scale Factor
Rotor Diameter	15 cm	100 μm	1500
Rotor Thickness	3 mm	3 μm	1000
Rotor–Sensor Thickness	6 mm	1 μm	200
Sensor–Substrate Thickness	0.5mm	0.5 μm	100
Rotor Pole Angle	$4 \times 45°$	$4 \times 45°$	1
Sensor Angle	$6 \times 20°$	$6 \times 20°$	1

Table 2.2: Comparison between macroscopic model and micromotor dimensions.

from pressboard and covered with copper tape to make its entire surface conducting. A 18 cm $\times$ 18 cm plate of aluminum was used as a ground plane with an overhead transparency laminated on its upper surface, insulating the sensor electrodes. Sensor electrodes were shaped from copper tape and attached to the insulating transparency layer. A plate of plexiglass was glued to the groundplane/sensor assembly to act as a rotor–sensor spacer and dielectric. A pin bearing was fashioned allowing the rotor to spin freely and float electrically. Capacitance was measured as a function of stationary rotor position using an HP impedance analyzer. The plot of capacitance between opposing sensor electrodes as the rotor sweeps through a quarter turn is shown in Figure 2.4. In the macroscopic motor model however, parasitic capacitances are significantly smaller than in the case of a micromotor. The macroscopic model has a parasitic to rotor-stator capacitance ratio of approximately 40:1 as opposed to a similar ratio of 1000:1 in the micromotor. At this point it appeared feasible to sense rotor position using capacitance variations. Analysis of the sensor and parasitic capacitances on a microscopic scale became necessary.

To gain more insight into the capacitance variation on a microscopic scale with a moving rotor, the FASTCAP capacitance extraction program [68] is employed in conjunction with a new post-processor POSTCAP described in Appendix C with source code listing given in Appendix D. The solid model shown in Figure 2.5 reduces the micromotor to a collection of 15 perfect conductors in free space. After analysis by FASTCAP, and after postprocessing by POSTCAP, at several static rotor positions

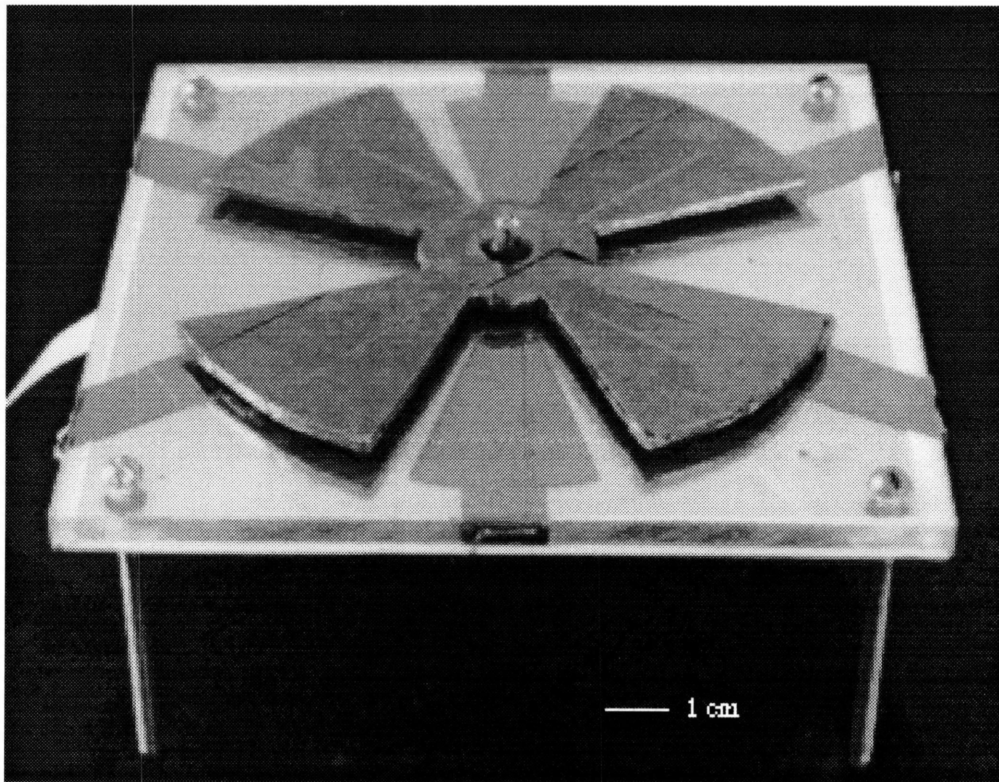

Figure 2.3: Photograph of a macroscopic capacitive sensing model used to demonstrate the capacitive rotor position sensing technique.

gives the complete capacitance matrices for all conductors. The capacitance of interest, namely the capacitance between two opposing sensors such as between conductors 10 and 14 shown in Figure 2.5, as the rotor passes over them is shown in Figure 2.6. From these results the capacitance variation is observed to be on the order of 1 fF. Parasitic capacitance associated with the measurement is, however, typically on the order of 1 pF, or 1000 times larger. The large parasitic capacitances make it difficult to measure the small rotor variations without the use of on-chip integrated buffer circuitry [51].

The advantages of the capacitance sensing technique are that sensors are integrated and can give real time electronic feedback to control circuitry. No light is necessary for the operation of capacitive sensing. The disadvantages are that large parasitic capacitances make measurement of the relatively small sensor capacitance variation difficult without the use of on-chip integrated buffers [51]. In the micro-

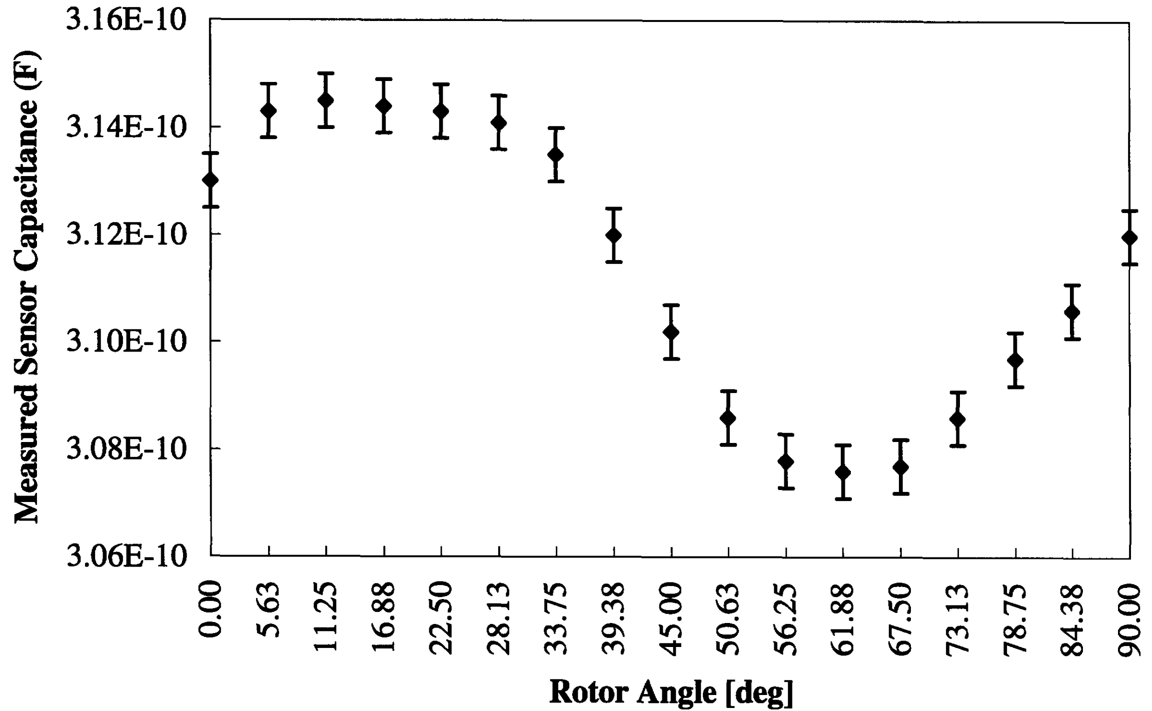

Figure 2.4: Plot of statically measured capacitance between two opposing sensor electrodes in the macro–model as the rotor sweeps through a quarter turn.

motor system, the capacitive sensor must be able to detect changes on the order of femtoFarads in the presence of parasitic capacitance of picoFarad size. The sensing action must occur at a frequency fast enough to maintain accurate position information of the moving rotor. The capacitive rotor sensing technique was not further pursued because of the fabrication complexity associated with the on-chip transistor buffers.

2.1.4 Rotor Optical Sensing

The final motion sensing technique to be considered is direct electro-optical sensing. This method was ultimately adopted for use in the micromotor. Direct electro-optical sensors are of three types. First, junction-based sensors involve photon generation of electron-hole pairs in the depletion region of the junction which can be used

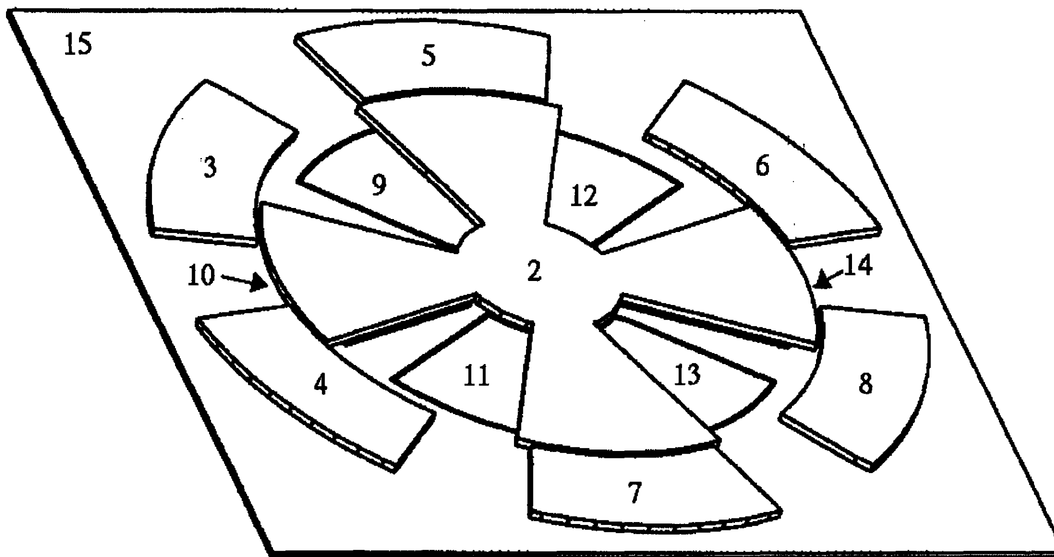

Figure 2.5: Solid model and conductor assignment for FASTCAP capacitance extraction in the micromotor.

in conductive mode or voltaic mode. Second, bulk conductivity sensors involving photon generated carriers that lower the bulk resistance where no junction is necessary. Third, photoemissive sensors that involve the release of an electron from a cathode when energized by a photon of sufficient energy. Junction-based photodiode sensors are chosen for use in the micromotor because light sensitive depletion regions were compatible with the motor fabrication process and could be selectively placed beneath the rotor through lithographic techniques. Photodiode sensors are used in many applications from TV remote control to optical fiber signal transmission. The sensors operated as illuminated p-n diodes where the reverse-bias current, directly proportional to the illumination, is independent of the applied terminal voltage. The sensors convert the variations in light intensity from the shadow of the moving rotor into electrical variations that are amplified by external circuitry. Further they appear to have none of the disadvantages of the sensors presented earlier. The only disadvantage is the need for a light source above the micromotor.

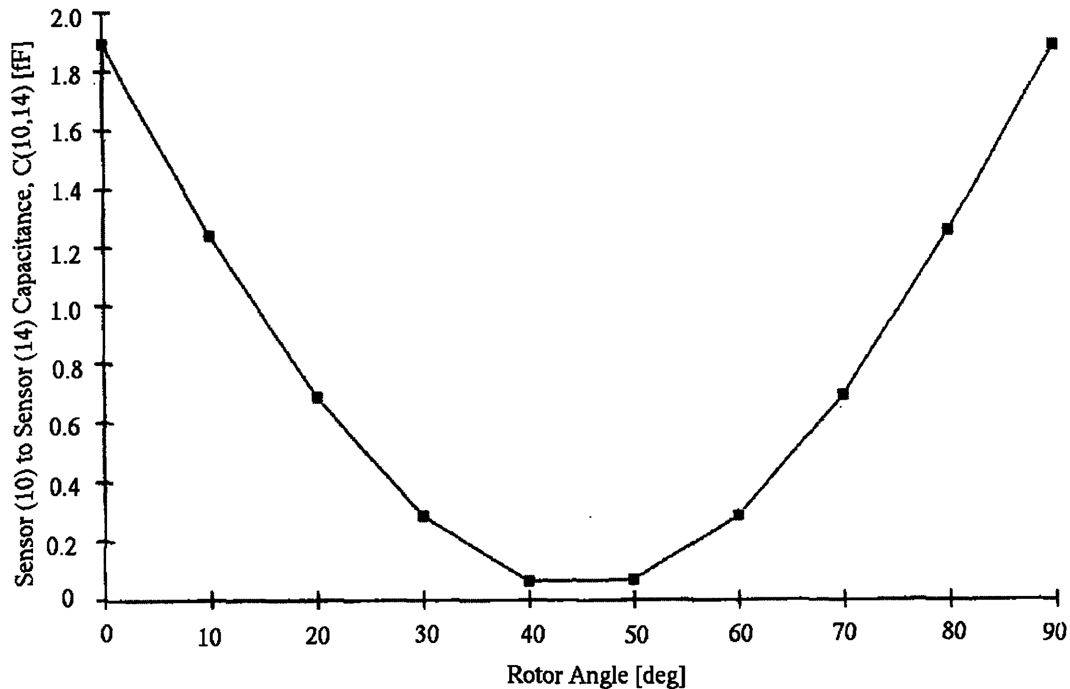

Figure 2.6: FASTCAP with POSTCAP solution to capacitance between two opposing sensors as a function of rotor position in the micromotor model.

2.2 Integrated Photodiode Sensors

This section describes design considerations for the photodiode sensors with respect to sensitivity, response time, and noise. Implications for sensor layout, processing parameters, incident light wavelengths, and rotational velocity ranges of the rotor are given. Further, the position extraction algorithm is presented which is used to extract rotor position in time from three equi-angularly spaced sensor signals. A set of three artificial sensor signals of arbitrary amplitude and offset with random noise ripple is constructed to simulate a moving rotor, and is fed into the position extraction algorithm to verify its correct operation. Finally, an off-chip amplification and filtering circuit used to read out photosensor signals and to provide the electrical drive excitation to the stator electrodes is described. The circuit contains a comparator function that allows self-switching for future closed-loop self-excitation.

2.2.1 Sensitivity

When an un-illuminated p-n junction is reverse-biased, a very small current on the order of picoamperes typically results. As the p-n junction is illuminated, the current can increase several orders of magnitude to levels readable through off chip circuitry. The generalized exponential model expressing the current-voltage $(i - v)$ characteristic of a p-n junction under both light and voltage applied is [30]

$$i = I_S(e^{qv/nkT} - 1) - I_p \tag{2.2}$$

where the ideality factor n and the saturation current I_S fully specify the characteristics of the un-illuminated contribution of current, and I_p is the photocurrent. The ideality factor n is experimentally determined in Chapter 4 to be 1.3. The applied junction voltage is v, and kT/q is the thermal voltage. The optically generated current I_p is created when electron-hole pairs are generated from incident photons with energy greater than or equal to the band-gap of the semiconductor material which enter the depletion region. Ideally, the photogeneration occurs in the depletion region of the p-n junction where incident light has been absorbed. The high electric field in the depletion region causes electrons and holes to separate, sweeping them in opposite directions and creating a drift current. Carriers generated outside the depletion region that are on average within a diffusion length of the depletion region diffuse into the depletion region and are collected across the junction.

The diode quantum efficiency η is a measure of the number of carrier pairs generated for each incident photon. The quantum efficiency will generally be high if the depletion region is thick enough to absorb most of the incident light. Assuming direct band-to-band transitions with no absorption due to impurity levels or traps, the photo current produced by incident light of power P_0 is [49]

$$I_L = P_0 \frac{q(1-r)}{h\nu}(1 - e^{-\alpha_0 \omega}) \tag{2.3}$$

where α_0 is an absorption coefficient at wavelength λ, q is the electronic charge, $h\nu$ is the photon energy ($h\nu = 1.24/\lambda$ eV), r is the Fresnel reflection coefficient at the silicon/air interface, and w is the width of the absorption region.

The quantum efficiency η is defined as the ratio of carrier pairs generated to the number of incident photons [49]

$$\eta = \frac{I_p/q}{P_0/h\nu} \tag{2.4}$$

Substituting Equation 2.3 into Equation 2.4

$$\eta = (1-r)(1-e^{-\alpha_0 \omega}) \tag{2.5}$$

In the ideal photodiode, $\eta \to 1$ and all incident photons generate carrier pairs. To achieve high quantum efficiency, w should be wider than $1/\alpha_0$ and also wide enough so carriers generated beyond the depletion region can diffuse back into it to be collected. The quantum efficiency of the fabricated photodiodes, corrected for multi-layer dielectric light filtering of the insulator, shield and passivation layers, is experimentally determined in Chapter 4 to be 65%.

The amount of photocurrent I_p generated by incident light also depends on the energy of incident photons and the band gap of the semiconductor material. Photons with too little energy (too long in wavelength) do not have sufficient energy to excite electrons into the conduction band. Photons with energy too high (too short in wavelength) will be absorbed quickly at the semiconductor surface by recombination before they are able to diffuse into the depletion region where they would create a photocurrent. Silicon photodiodes respond to light of wavelengths between 0.7 and 0.9 μm [30]. If the p-n junction is placed very close to the semiconductor surface, for example by shielding photogenerated carriers from surface recombination effects, the sensitivity in silicon may be extended to the visible spectrum from 0.4 to 0.7 μm [30]. Longer wavelengths may be sensed by using different semiconductor materials such as indium gallium arsenide and germanium which have smaller energy gaps. The depth of the photojunction is constrained by the light wavelength. In Chapter 3 the

selection of a sensor implant species for low thermal diffusivity is examined to obtain shallower photojunctions allowing photocurrent generation.

In order to increase diode sensitivity to light, the illuminated junction area should be made large to maximize the number of incident photons. The junction should also be placed near the top surface since only the photogenerated minority carriers diffusing to the edge of the depletion region will contribute to the photocurrent. It is desirable to have a large depletion region, since photons entering the depletion region that generate hole-electron pairs will cause the holes and electrons to be swept across the junction as a photocurrent. An alternative to increasing the depletion region size is to place an undoped layer between the p and n type sides of the junction, forming a p-i-n diode. The top ohmic contact of the diode should be placed away from the sensor region so as not to block incident photons. The area of the contact should be small to minimize carrier recombination at the contact. The sensor surface also can act as a recombination site and may be engineered to minimized this effect by increasing the potential barrier near the surface with a thin, heavily doped region there. The potential barrier keeps minority carriers away from the surface, preventing their recombination and increasing the diode's sensitivity to light.

2.2.2 Response Speed

The speed at which a photodiode and its read-out electronics responds depends on at least three factors. First, diode response speed depends on the RC time constant of the output circuit, including capacitances in the photodiode such as depletion and diffusion capacitance. Second, response speed depends on the diffusion time of carriers generated outside of the depletion region. Third, response speed depends on the transit time of photo-generated carriers in the depletion region. The dominant time constant determines the limiting speed of the diode.

The first response speed factor is the time constant of the read out circuit. It dominates over the intrinsic charge storage mechanisms in series with resistance which exist in the pn diode. The off chip read out circuit is engineered to have a time

constant of 250 μs in order to filter undesirable high-frequency electronic noise picked up at the sensor probes. If the off chip circuit time constant were reduced, the charge-storage mechanisms in the pn-junction could dominate. The depletion and the diffusion capacitances are nonlinear functions of voltage that can be linearized about an operating point. Any series resistance determines the charging behavior of the two nonlinear capacitors and hence the response speed of the diode.

The second factor limiting response speed depends on the time for carriers to diffuse outside of the depletion region. Typical hole diffusion times are on the order of 40 ns through 10 μm [49]. This is much faster than the external electronics. The third factor is the drift transit time across the depletion region. The need for a thick depletion layer to maximize photon capture is traded off with the need for a thin depletion region for shorter carrier drift times. Typical electric fields greater than 2×10^4 V/cm cause carriers to attain a scattering-limited saturation velocities of approximately 10^7 cm/sec in silicon [49]. For a sub-micron depletion width, the transit time can be less than 10 ps giving response in the gigahertz range. Again this is very fast, thus the dominant response speed limiting mechanism is the time constant of the off-chip readout circuitry.

2.2.3 Noise

Noise in the p-n photodiode sensors can degrade the optical measurement signal and worsen the feedback response of the sensor. Various sources of noise are present in both the detection and amplification of the shuttered optical signal. Background radiation is a possible source of noise, but is negligible in the micromotor system. The noise generated from various spectral components of the incoherent light source beating together is taken as insignificant due to the large number of modes transmitted and received. If the incandescent lamp source is driven by a line AC signal, light intensity varies at a frequency of 120 Hz which can distort motion measurements near this frequency. A DC lamp source drive is used instead to remove this component from the light. The dark-current noise and surface-leakage current noise of the photosensor

can be reduced by careful design and fabrication of the sensor system. For example, the wafer surface can be passivated with a thin oxide to reduce surface leakage. The quantum noise due to intrinsic fluctuations of charge carriers sets the ultimate limit on the sensor sensitivity. Noise present in the amplification of the diode signal is the dominant noise source and is measured in Chapter 4 to be 10 mV.

2.2.4 Position Extraction Algorithm

This section presents a description of the algorithm listed in Appendix D used to extract rotor position in time from three equi-angularly spaced sensor signals. Their outputs should be approximately three symmetric sinusoids, but they may in general have different biases and amplitudes. A set of three artificial sensor signals of arbitrary amplitude and offset with random noise ripple is constructed to simulate a forward moving rotor at uniform velocity. The simulated data is fed into the position extraction algorithm to verify its correct operation.

The position extraction algorithm shown in flowchart form in Figure 2.7 first loads the digitized raw sensor signals from three data files into internal arrays. The simulated data loaded in the verification test is shown in Figure 2.8 for a motor spinning at uniform angular velocity of 1200 rpm. This simulated data has arbitrary DC offset and amplitude. A random signal of 10% of the sinusoidal amplitude is added to each sinusoidal signal to simulate sensor noise. The algorithm first blanks electrical drive coupling over narrow windows which straddle the stator drive voltage transitions, and then linearly interpolates the data from one side of the window to the other. Given the data in Figure 2.8, this step is unnecessary, but its ultimate necessity is demonstrated in Chapter 4. Next the algorithm passes each sensor signal through an averaging window filter which is ten samples wide to smooth any high frequency noise. The high and low values in each data stream are found and used to normalize the sensor signal to unity amplitude and remove any DC offset.

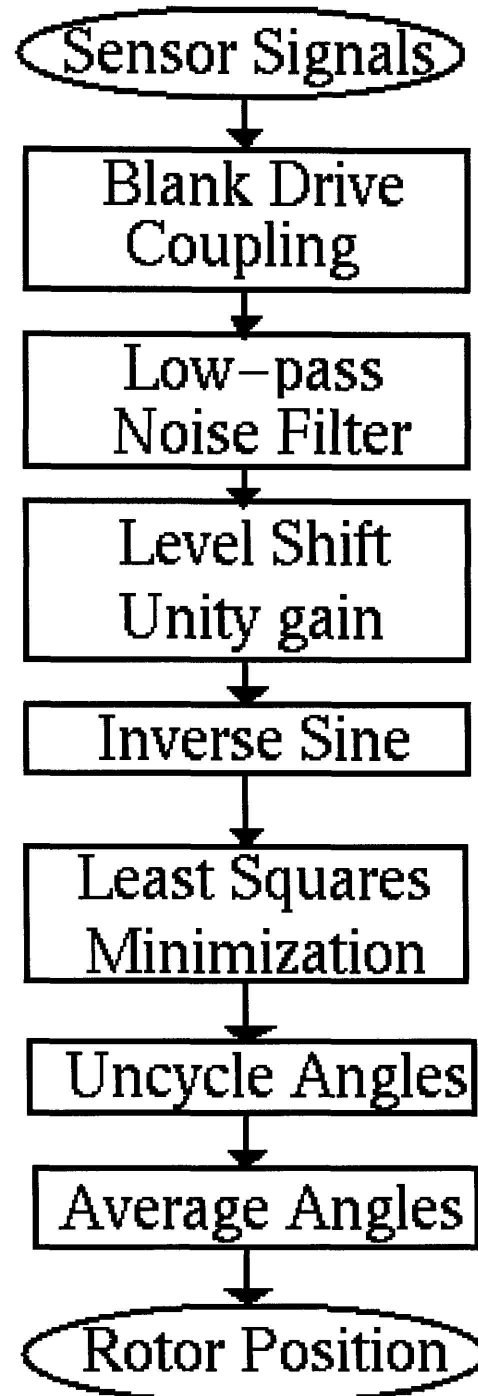

Figure 2.7: Flowchart of the position extraction algorithm.

Each sensor data array is assumed to be a pure sinusoidal function of rotor angle. For each sensor data point, two possible inverse sine angles exist. The algorithm takes both values of the inverse sine and stores them. Next, all angles are shifted in integer multiples of 2π to lie between 0 and 2π radians. For each possible set of three angles at a given time, the nearest distances on a circle between an angle to its two nearest neighbors is stored, along with the angle and the mean of the set of three angles. The sum of squares of differences from the mean give a mean-squared error. At the minimum mean-squared error, that set of three sensor angles are the correct physical angle of the rotor.

A trickle-down tree determines the minimum mean square error to give the correct physical angles of the rotor. Data is unwrapped in time by adding multiples of 2π as the rotor travels more than one revolution giving position data moving forward in time. This is called uncycling. Spikes in the data that result during the uncycling process from angles lying greater than 180 degrees apart are smoothed by averaging with their previous and next values. The angles given by each sensor signal are shown from the simulated data in Figure 2.9 and track each other well. A better approximation of the rotor position is calculated by averaging, with equal weight, the three angles at each time point. Figure 2.10 shows the average of the three position values at each time step to give the rotor position in time. As would be expected from the simulated data, the rotor moves forward in time at a uniform velocity.

2.2.5 Signal Conditioning and Control Circuitry

The off-chip amplification and filtering circuit shown in Figure 2.11 is used to read out photosensor signals and to provide the electrical drive excitation to the stator electrodes. The circuit contains comparators that allow it to be switched into a closed-loop configuration for micromotor self-excitation. This method, however, is not used in this thesis.

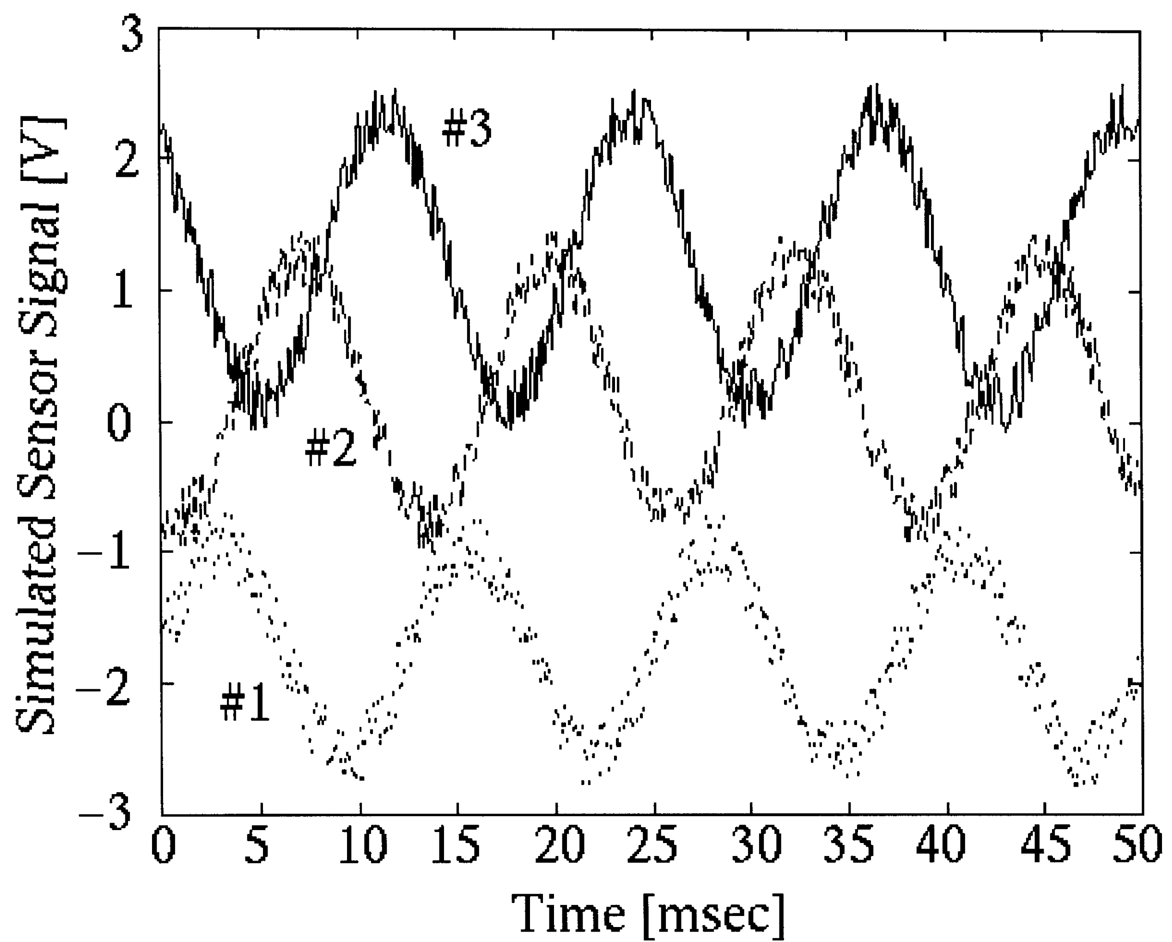

Figure 2.8: Simulated sensor data having arbitrarily offset sinusoidal signals, arbitrary amplitude and added random noise.

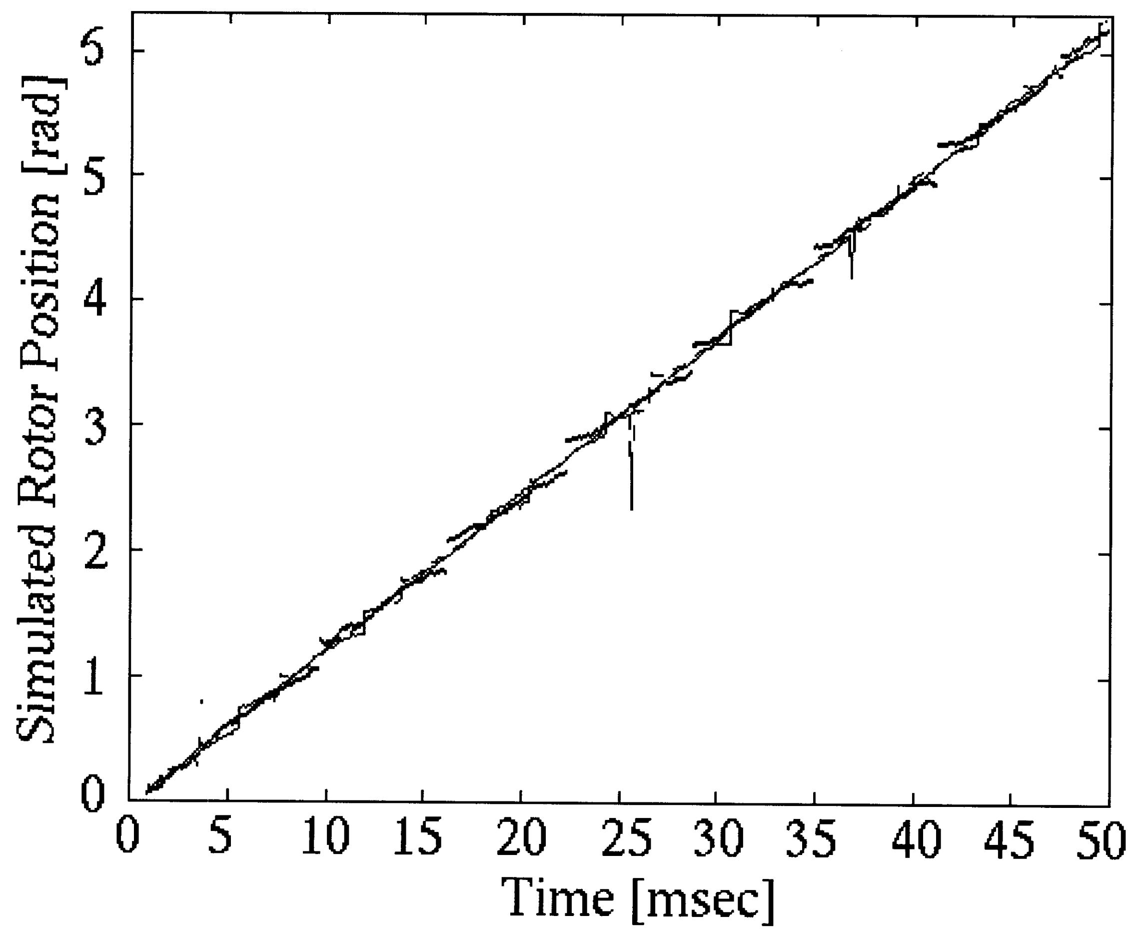

Figure 2.9: Three computed angle positions for simulated sensor data.

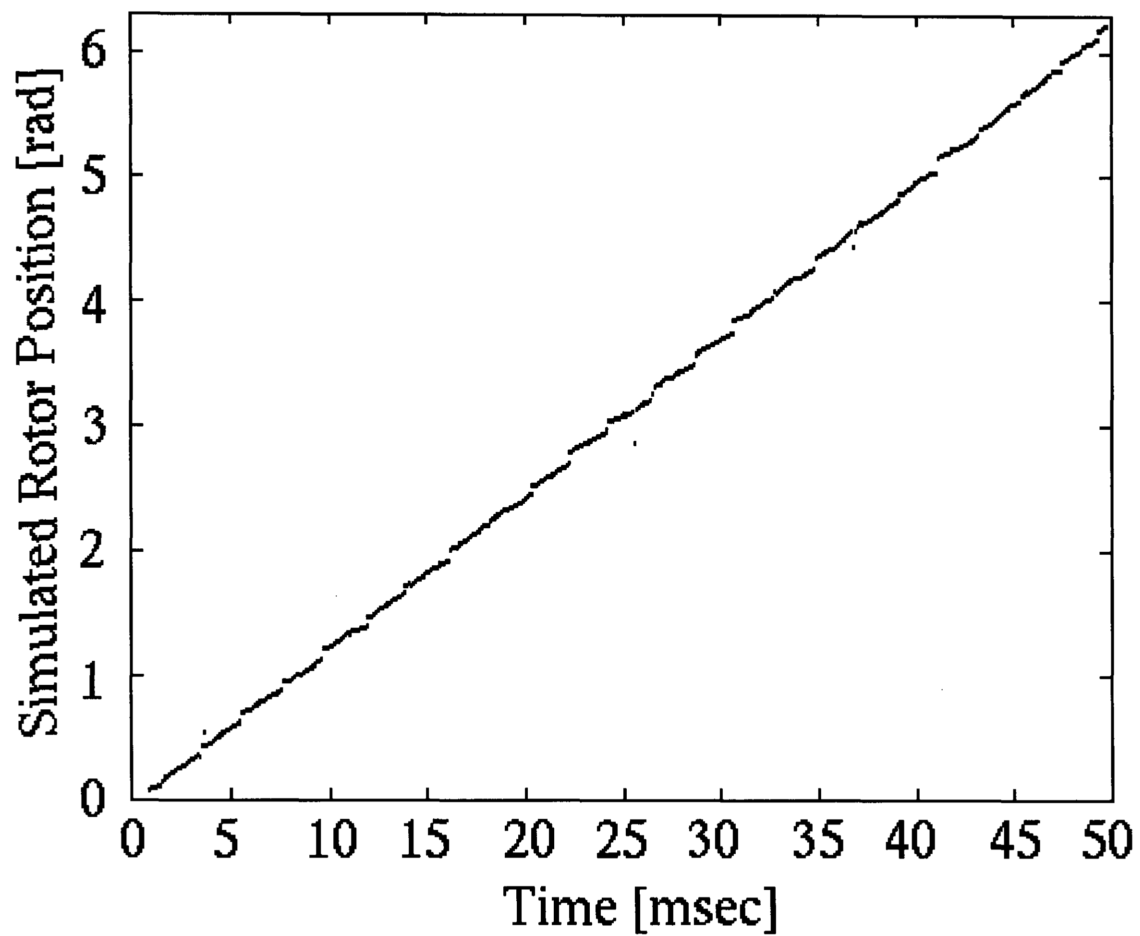

Figure 2.10: Computed position average for simulated sensor data.

The photodiodes are biased at zero volts at the inverting input the first amplifier (OP270) and held to virtual ground. Any photo current is mirrored by the amplifier and forced through variable resistance R1. Resistance R1 is used to tune the signal amplification to lie in the linear range of amplifier operation. Next the amplified photocurrent signal, now represented as a voltage, is passed through a second amplification stage which inverts the voltage and boosts it by a factor of 800. The second amplifier has a parallel capacitor in its feedback loop which creates a low-pass filter necessary to prevent external high-frequency electronic noise from saturating the amplifier. The time constant of the low-pass filter is chosen to be 250 μsec and may be varied by adjusting the capacitance. The two stages of amplification as shown in the dotted box in Figure 2.11 are isolated and shielded from the rest of the circuitry. This was found to be necessary because of electronic coupling between these circuits and the subsequent high-voltage amplifier stages. The three signals coming out of the dotted box may be sampled and digitized with a TDS540 oscilloscope and passed through the position extraction algorithm discussed above, or they may be compared to one another by three LT1016 high-speed comparators to determine the proper rotor phase to be excited in a closed-loop configuration. The comparator outputs or the input from a three phase bi-directional variable speed TTL counter circuit is OR-gated and passed to six high-speed opto-coupler circuits which translate the TTL level signal in the high positive and negative drive signals. The TTL variable speed, bidirectional counter circuit is used to generate drive phase timing for the open-loop motion studies. This is the method of amplification used in this thesis.

The off-chip sensor amplifier, filter and drive circuit shown in Figure 2.11 may be extended to allow real-time implementation of the entire position extraction algorithm for the purposes of closed-loop control. Analog level-shifting and amplitude-adjustment stages can be added to each channel to give the three signals equal amplitude and offset. Alternatively, these functions might best be performed by a digital processor. The decision logic and extraction of position could be implemented in a ROM look-up table that takes digitized sensor signals as its input. Or, if the preced-

ing stages are implemented in a digital processor, then the final stages should be too. In any case, the sampling of the sensor signals must occur at a rate much faster than the peak electrical speed of motor so that motion detail is not lost. The output of the ROM look-up table or digital processor would then drive a PID controller or give rotor angle in real time.

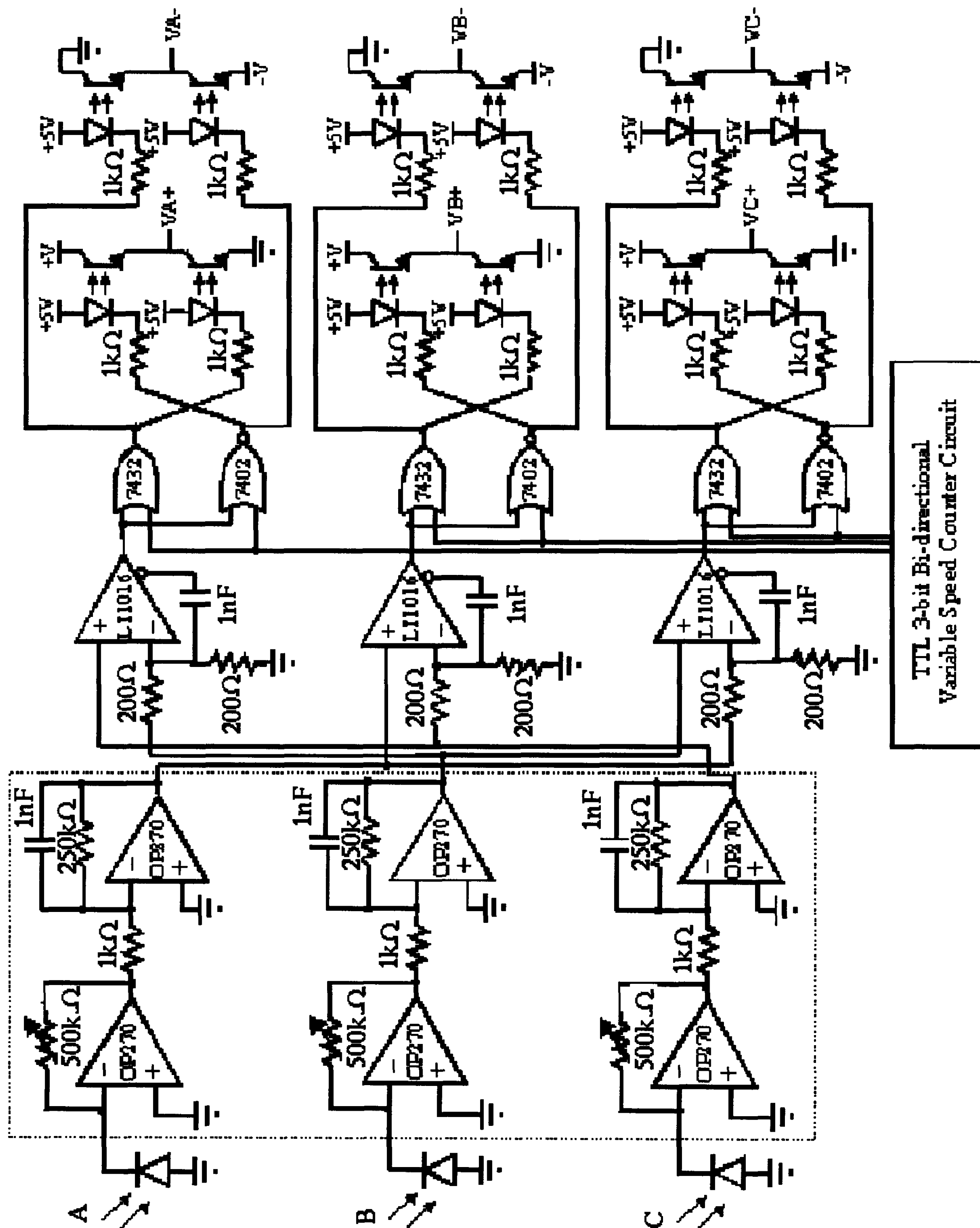

Figure 2.11: Schematic of off-chip sensor amplification, filter, and drive circuit. The section in the dotted box is isolated in a separate shielded enclosure and is used to amplify the sensor signals.

Chapter 3

Design and Fabrication

This chapter describes the design and fabrication of an improved micromotor using a robust process that allows incorporation of electronic devices with the passivation and shielding steps necessary to obtain useful sensor signals. In the first section of this chapter, the theory of micromotor operation is reviewed. In the second section, the new fabrication process is described in the areas of electronics integration, surface micromachining, and post-processing release. In the third section, specific changes to the micromotor design are presented including surface passivation and threshold implants, electrical shielding layers, gap plug oxide, post-processing release, and new bearing designs and materials. micromotor design are presented including surface passivation and threshold implants, electrical shielding layers, gap plug oxide, post-processing release, and new bearing designs and materials.

3.1 Theory of Operation

The electric micromotor shown in Figure 1.1 is surface micromachined from silicon-based materials above a single crystal silicon substrate. As seen in the cross section of Figure 3.1, this motor is a planar actuator with a conducting polysilicon rotor 2.5 μm thick and 100 μm in diameter. The micromotor may be electrically driven by electrostatic forces which appear across the 1.5 μm wide rotor-stator gaps. The planar rotor spins around a central bearing of a diameter typically equal to or greater than 10 μm which overhangs its rotor by 5 μm to hold the rotor in place at the substrate. The clearance between the bearing and rotor is approximately 0.3 μm. The stator electrodes, which are fabricated of the same material and thickness as the rotor, encircle the rotor in its plane of motion and are anchored to the electrical isolation

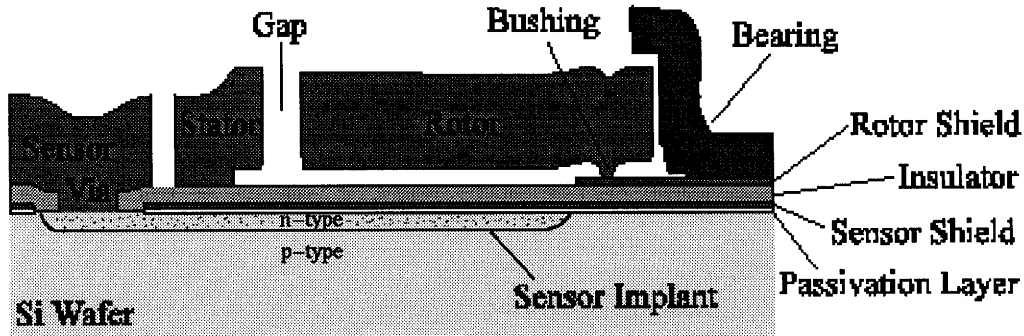

Figure 3.1: Half cross-section of typical micromotor. The vertical scale has been exaggerated.

layer. The stators are driven by external voltage phases, electrically exciting the rotor and putting it into motion. Friction between the rotor and substrate is reduced through the use of bushings that take the form of 1.0 μm tall dimples, collars, or flat steps beneath the rotor. They act to minimize the rotor-to-substrate contact area and minimize the radius of contact for lower frictional torque.

The bearing is anchored to a 0.15 μm thick conducting polysilicon rotor shield layer which is secured to the insulator layer. The rotor shield layer decouples the rotor from vertically-directed electric fields that could exist if the rotor and substrate were at different electric potentials. These fields could cause the rotor to pull-in to the substrate and increase the frictional torque acting on the rotor. With the shield layer making electrical contact to the rotor through the bearing or bushings, fields between the rotor and substrate are reduced or eliminated, in turn reducing or eliminating pull-down forces on the rotor and reducing the frictional torque acting on the rotor.

A 4000 Å thick insulator layer of silicon-rich silicon nitride electrically insulates the stator electrodes from the conducting substrate. The maximum potential difference, before breakdown, across the silicon nitride is measured to be 280 V. Below the insulator layer is a 1500 Å thick conducting polysilicon sensor shield. The sensor shield acts to isolate the sensor implants from capacitive coupling with the stator electrodes as they switch their drive voltages which may be as large as 100 V. The

sensor shield also serves to rapidly discharge to ground any charge accumulated at the nitride-oxide interface. Below the sensor shield lies a 220 Å thermal oxide passivation layer which insulates the sensor shield from the substrate and passivates the silicon surface. The insulator, sensor shield, and passivation layer are thin enough to be transparent to visible light, allowing the sensors to detect the moving rotor shadow.

Variable-capacitance micromotors with radially-directed gaps are fabricated in this thesis. The type of motor studied shown in Figure 1.1 is the ordinary side-drive motor identified by its characteristic rotor saliency. This motor has salient stator poles which are driven by external circuitry. Excitation in the ordinary micromotor occurs as opposing bipolar voltage phases induce charges of opposite polarity on the rotor pole nearest those of the exciting phase. A torque of electric origin results as the rotor is forced to align its charged poles with the excited stator poles. The bipolar phase voltages are timed to synchronously and sequentially step the rotor around the bearing. As amplitude and timing of the excitation are varied, a coarse degree of open-loop motion control is possible. It is desirable to minimize friction between the rotor and bearing to reduce frictional torque and maximize electromotive torque.

Micromotors are able to overcome frictional torque and rotate because of the enhanced electric field strength associated with their micron-scale gaps. It is well known that air environments at standard temperature and pressure support electric field strengths up to 3×10^6 V/m before the onset of electrical breakdown. As a result the maximum energy storage capacity of the gap in an electric motor of comparable dimension to a conventional magnetic motor is limited to approximately 10^{-4} of the magnetic motor [5]. The maximum energy density, which scales as the square of electric breakdown strength, has been observed to be greatly increased as the gap decreases below 6 μm in air [72]. Electric micromotors exploit this increased maximum energy density in their micron-scale gaps which are able to support electric fields up to 10^8 V/m, removing the 10^{-4} energy storage disadvantage when compared to magnetic motors.

Motive electric torque in a micromotor is typically limited by the electrical break-

down strength of the rotor-stator gap, occurring via two different mechanisms. The first mechanism occurring at lower field strengths is an avalanche process known as Townsend breakdown. Townsend breakdown limits the maximum electric field as charged particles accelerated by the electric field collide with neutral particles generating more charged particles to result in a large current or arc [94] . The avalanching process becomes self-supporting when each charged particle ionizes at least one neutral particle before impacting the opposing electrode. The second mechanism occurring at much higher field strengths is field emission where electrons are pulled directly from the electrodes and drift across the gap. The electric breakdown across a gap has been shown to depend on the number of gas particles in the gap [15]. A gap under perfect vacuum has no particles and is limited to the field emission mechanism of its surfaces which has been measured to be as high as 10^9 V/m for smooth clean surfaces [94]. At these field strengths the electric energy densities would be comparable to energy densities found in magnetic motors [5] but surface imperfections limit such high fields in practice [11].

The breakdown strength of a gap depends on both the spacing and the number of particles in the gap. Early studies in vacuum electrostatic engineering described the benefits of a vacuum gap in higher maximum breakdown fields and reduced windage on a moving rotor [92]. However, vacuum engineering is challenged by the difficulties of vacuum containment and coupling [92]. Higher maximum breakdown strengths may be approached by reducing the gap spacing at standard pressure. Paschen's curve for the breakdown strength of air shows the minimum level of pressure-spacing product with the amount of ionizing particles in the gap at the onset of self-supporting avalanching [15]. In air at standard temperature and pressure the gap spacing occurs at 6 μm. The minimum in the Paschen curve indicates that breakdown will not occur in air below 340 V regardless of gap size until field emission mechanisms begin. Paschen's minimum is also the maximum voltage that can be applied to gaps below 6 μm because higher voltages, even though withstood by the minimum gap would cause nearby gaps larger than 6 μm to breakdown unless they were shielded by insulators.

In operational micromotors the effects of maximum allowable field is further limited by the accumulation of wear particles which effectively reduce the gap spacing. In this thesis, typical micromotor excitation voltages in the range of 70 V to 100 V over gaps of 1.0 μm to 1.5 μm create field strengths on the order of 10^8 V/m without breakdown.

3.2 Fabrication

Fabrication exploits standard integrated circuit materials and process steps. Film thicknesses have been increased in many steps beyond levels typically found in integrated circuits to insure structural rigidity of the mechanical components and to maintain the necessary spacings in the motor geometry. Several plasma etch recipes and implants described here have been custom developed for the micromotor and sensor devices. A formal process traveler with standard baseline and non-baseline operation sets used in the MIT Integrated Circuits Laboratory (ICL) and detailed lithography, etching, diffusion, oxidation, and deposition recipes may be found in Appendix A. The processing sequence is graphically shown in Figures 3.2 and 3.3. The fabrication of integrated pn-junction photodiode sensors is described with surface passivation, field implants, and electrical shielding steps necessary to electrically isolate the sensor signals from the high voltage drive. Surface micromachining of the major structural components in the motor including the rotor, stators, bushings, and bearings follows sensor integration.

The micromotor fabrication process begins with the creation of masks which are used to define patterns on each thin film layer and are used to transfer this pattern to the wafer surface during fabrication. Masks begin as layouts designed on a KIC CAD system [10]. Figures 3.4 and 3.5 show typical layouts of an individual motor with pads and an entire mask layer.

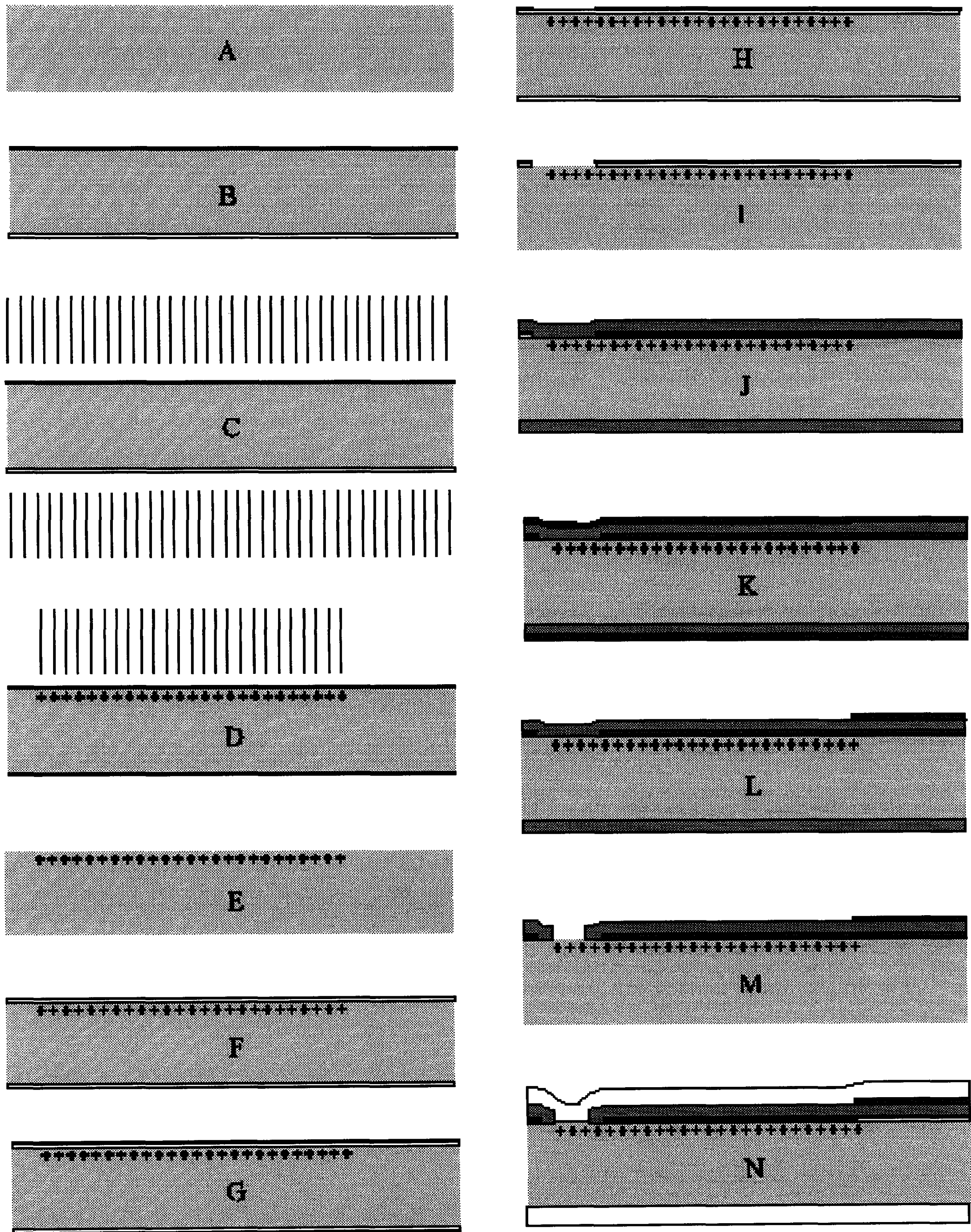

Figure 3.2: Fabrication process.

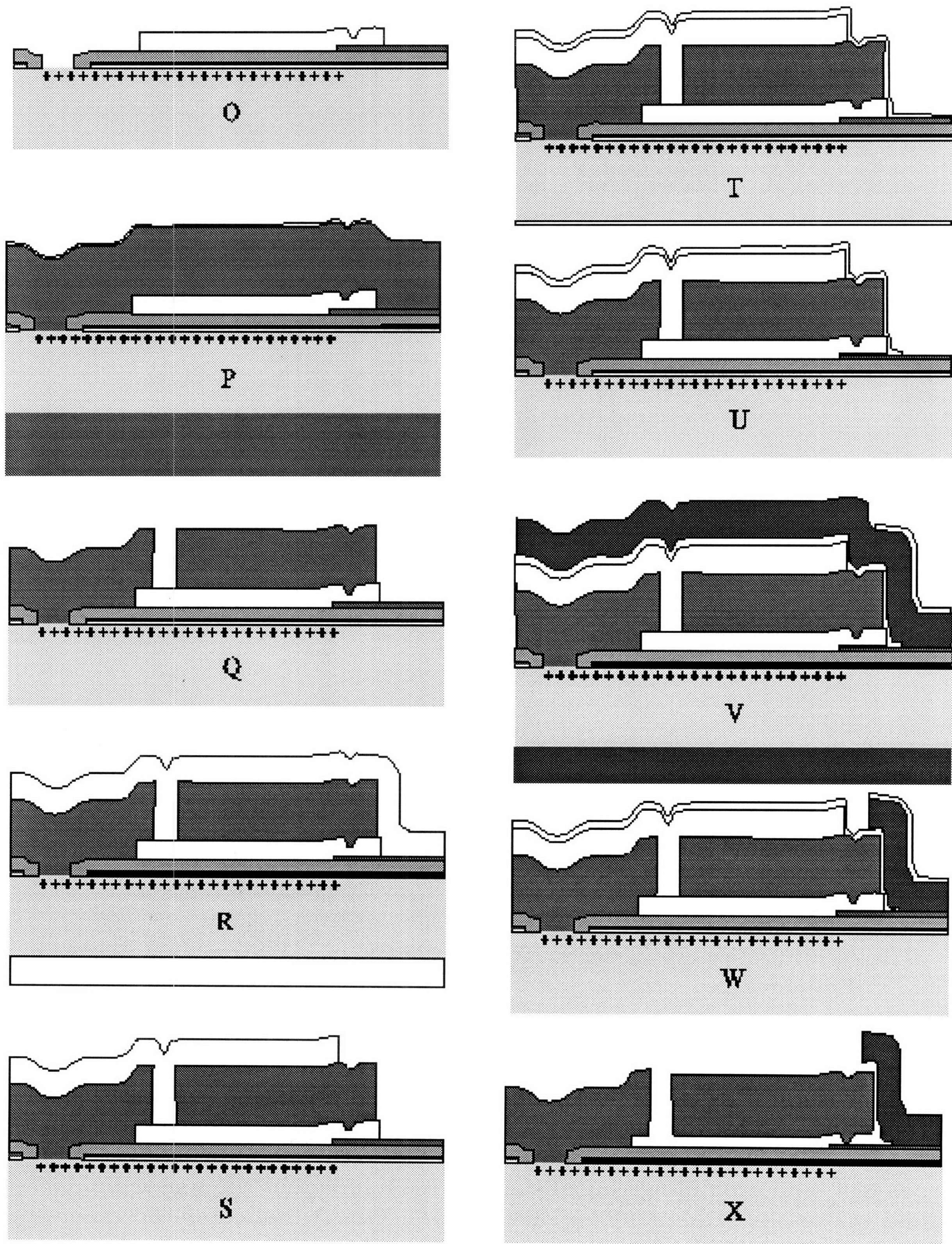

Figure 3.3: Continued fabrication process.

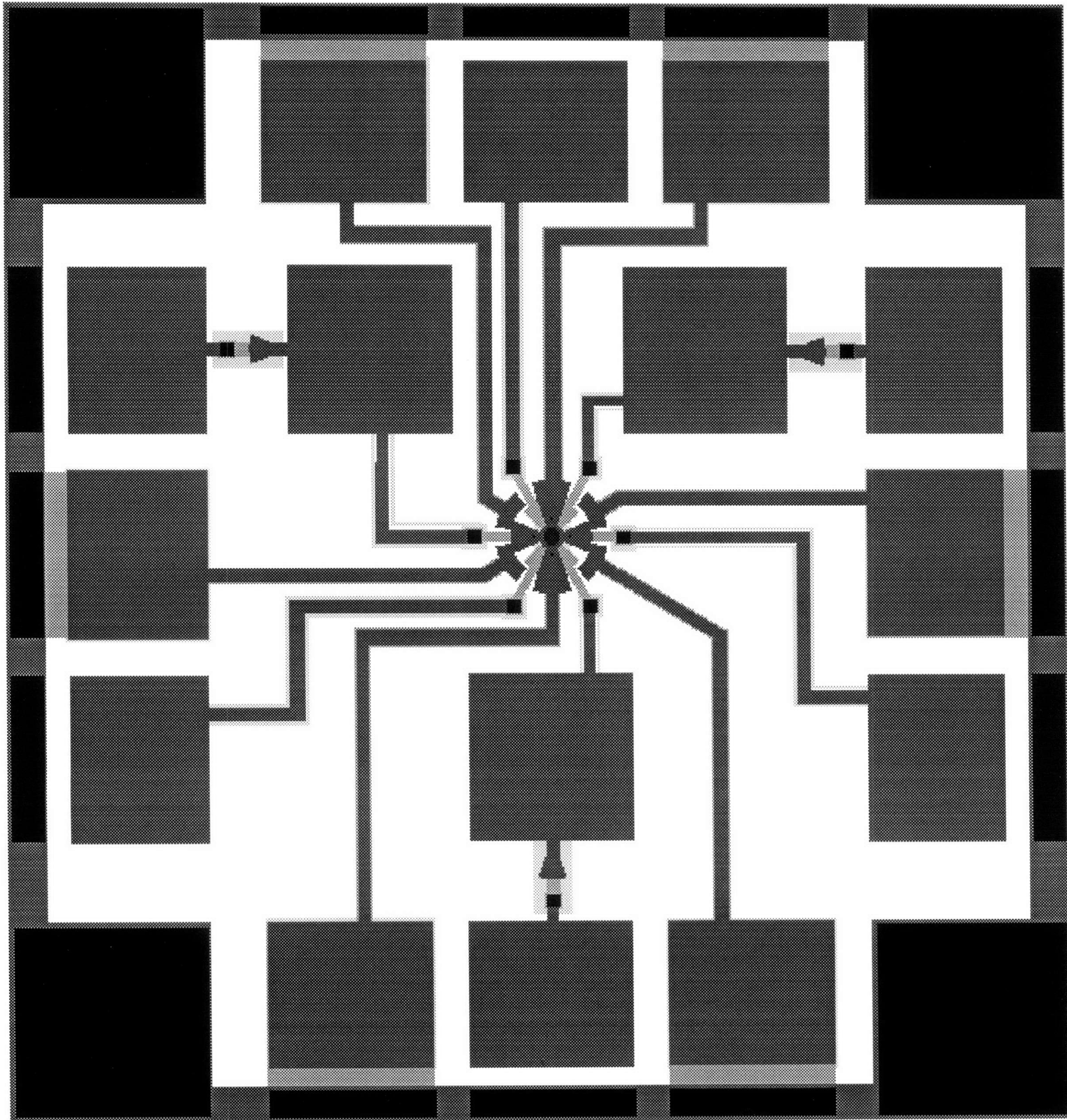

Figure 3.4: Layout of a typical micromotor with sensors. BLACK indicates the location of bushings, vias connecting polysilicon sensor interconnect to sensor diffusions, and vias connecting the polysilicon grounding-ring to the stator-shield implants. VERY DARK GRAY indicates the bearing. DARK GRAY indicates the polysilicon of the rotor, stator, sensor interconnect, and grounding-ring. LIGHT GRAY indicates the sensor implant and stator-shield implant. VERY LIGHT GRAY indicates the absence of the polysilicon sensor-shield. WHITE is the polysilicon sensor-shield, located everywhere except at VERY LIGHT GRAY.

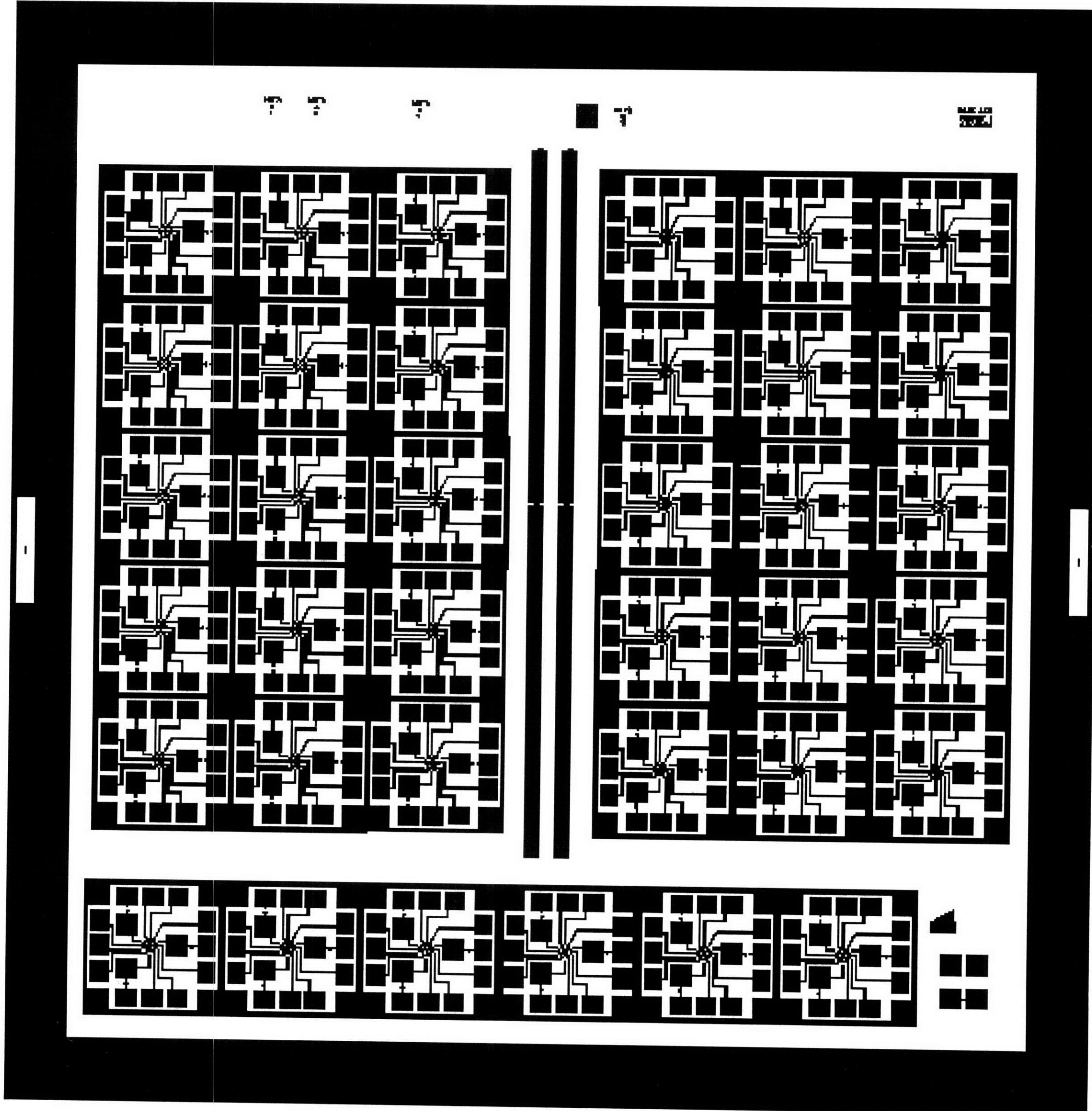

Figure 3.5: Layout of an entire micromotor mask layer.

The starting material shown in cross-section A of Figure 3.2 is a 100 mm diameter p-type boron-doped (100) oriented single crystal silicon wafer with a resistivity in the range of 10 – 20 Ω-cm. This wafer is polished on the front-side only. Mask alignment marks are transferred to the front-side silicon substrate using an isotropic SF_6-based plasma etch. A dummy thermal oxide 220 Å thick is grown at 950°C for 35 minutes in dry oxygen to protect the wafer surface from ion implant damage during the implants that adjust electrical characteristics of the wafer surfaces and define the sensors as shown in cross-section B of Figure 3.2. The dummy oxide protects the front surface from scratching during the back-side implant.

The first implant is a shallow p-type blanket of boron to adjust the field threshold voltage and prevent an inversion layer from forming that could electrically connect sensor regions together with the stator shield implant regions. The wafers are flipped and receive a blanket back-side p+ ion implant of BF_2 to allow good back-side electrical contact to the substrate during motor testing as shown in cross-section C of Figure 3.2. The front-side is masked with photoresist and a selective n+ implant of arsenic forms the sensor regions and the electrical stator shield beneath the stators as shown in cross-section D of Figure 3.2. The implant mask is plasma ashed and the wafers are piranha cleaned to remove any remaining photoresist that may have baked on during the high energy implant. The dummy oxide is stripped using 7:1 Buffered Oxide Etch (BOE) for 180 seconds as shown in cross-section E of Figure 3.2.

A new oxide 500 Å thick is grown under the same conditions as the dummy oxide as shown in cross-section F of Figure 3.2. The new oxide passivates the wafer surface, activates the implants, and serves as an electrical isolation between the implant regions and the first polysilicon shield layer. The oxide also acts as an etch stop for the isotropic polysilicon plasma etch used to pattern the sensor shield layer. The sensor shield is LPCVD polysilicon deposited to a 1500 Å thickness at 625°C followed by phosphorus doping using a liquid $POCl_3$ source for 90 minutes with 15 minutes of dry oxygen at 925°C as shown in cross-section G of Figure 3.2. The resulting phosphorus doped glass is removed (deglazed) in a wet strip etch using 7:1 BOE for 180

seconds. The sensor shield layer is patterned with photoresist and etched using the isotropic SF_6-based plasma etch as shown in cross-section H of Figure 3.2. It serves as a grounded electrical shield to isolate the stators from the sensor implants. After the sensor shield is etched, the wafer front-side receives a protective coat of photoresist to prevent scratching during front-side handling and is flipped for a polysilicon plasma etch, removing the back-side polysilicon in the isotropic SF_6-based plasma etch.

The thermal passivation oxide layer is masked with patterned photoresist and etched in 7:1 BOE for 60 seconds creating the vias which connect the polysilicon interconnect with the sensor implants, and allowing connection to the outer ground ring with the stator shield implants as shown in cross-section I of Figure 3.2. A 4000 Å LPCVD silicon-rich silicon nitride layer with low intrinsic stress is deposited as an electrical insulator between the sensor shield layer, sensor implants, and substrate as shown in cross-section J of Figure 3.2. The silicon nitride insulation layer protects the thermal passivation oxide layer during subsequent HF-based etches. A second 1500 Å LPCVD polysilicon shield is deposited, $POCL_3$ doped, and deglazed in an identical manner to the first polysilicon shield as shown in cross-sections K of Figure 3.2. The rotor shield is masked with patterned photoresist and etched using the isotropic SF_6-based etch recipe as shown in cross-section L of Figure 3.2. The polysilicon rotor shield makes electrical contact to the rotor via the bushings and shares charge with the rotor, while acting to minimize electrostatic coupling between the rotor and the grounded sensor shield.

A low temperature oxide (LTO) hard-mask is deposited to a thickness of 5000 Å masked, and etched in 7:1 BOE for 140 seconds to pattern the electrical vias through the silicon nitride insulation layer. The silicon nitride insulator is wet etched in 175°C boiling phosphoric acid for 100 minutes to create the vias as shown in cross-section M of Figure 3.2. This nitride etch also removes any nitride on the wafer back-side allowing backside electrical contact. The via holes are patterned to be smaller than the thermal passivation oxide holes to seal the oxide in. A nitride wet etch rather than a dry plasma etch has been chosen for better etch selectivity preventing overetch

into the silicon substrate that would penetrate the shallow implant regions at the via contact.

A 1 μm LPCVD LTO is deposited on top of the oxide hard-mask as shown in cross-section N of Figure 3.2. This oxide together with the nitride hard-mask oxide form the sacrificial oxide support for the rotor. Bushing molds 1 μm deep are wet etched into the oxide using a timed 7:1 BOE etch leaving approximately 5000 Å oxide beneath the bushings. The sacrificial oxide is patterned and wet etched in 7:1 BOE for 6 minutes creating anchors for the bearing, stators, interconnect, and pads as shown in cross-section O of Figure 3.3.

The rotor, stators, interconnect, and pads are machined from 2.5 μm LPCVD polysilicon, $POCl_3$ doped for 3 hours, then deglazed in a 7:1 BOE. A thermal oxide of 2000 Å is grown on the polysilicon to form an oxide hard-mask. The oxide hard-mask is masked with patterned photoresist and plasma etched using an anisotropic oxide etch as shown in cross-section P of Figure 3.3. The polysilicon is then plasma etched with the anisotropic polysilicon etch as shown in cross-section Q of Figure 3.3. The machining of straight side-walls during this etch is critical for the the prevention of electrical breakdown during operation and to maximize gap energy storage for greater motive torque.

A 1 μm LPCVD LTO is deposited to fill in the narrow rotor/stator gap and acts as a gap oxide plug during the bearing deposition as shown in cross-section R of Figure 3.3. This step increases motor yield since the bearing material is often difficult to remove completely from the narrow rotor/stator gaps. The plug oxide is masked with patterned photoresist to cover all but the bearing region. The gap plug oxide is removed at the bearing region in 7:1 BOE as shown in cross-section S of Figure 3.3. A 5000 Å LPCVD LTO layer deposited approximately 3500 Å thick on the sidewalls becomes the spacer oxide for the bearing gap as shown in cross-section T of Figure 3.3. Another photoresist mask is used to pattern bearing anchors using 7:1 BOE shown in cross-section U of Figure 3.3.

At this point, wafers lots may be split into sub-lots for different bearing materials.

Low-stress silicon nitride bearings are deposited with 1 μm thick 10:1 of SiH_2Cl_2:NH_3 flow-ratio silicon-rich silicon nitride. These bearings are used for the motion studies in this thesis because of their superior low frictional characteristics compared to other bearings. Polysilicon bearings may be deposited with 1 μm LPCVD polysilicon. Both polysilicon and nitride bearings are patterned with 5000 Å LTO oxide hard-mask as shown in cross-section V of Figure 3.3. Polysilicon bearings are etched using the isotropic SF_6-based plasma etch. Silicon nitride bearings are wet etched in 175°C boiling phosphoric acid for 6 hours as shown in cross-section W of Figure 3.3. Additional bearing materials not allowed in the main processing facility such as gold may be created using ultrasonic lift-off. A photoresist inverse bearing mask is deposited and gold is e-beam evaporated on the inverse mask. The resist is dissolved in acetone and the wafer is agitated using an ultrasonic bath which lifts-off residual material around the bearings. Experimental tungsten bearings have been grown using a selective CVD tungsten process and if successful, would not require a patterning step.

Motor wafers are die-sawed into 8×8 dies. Motor dies are placed into concentrated liquid HF and etched for 15 minutes to insure undercut of the sacrificial oxide and full release of the rotor at the bearings as shown in cross-section X of Figure 3.3. Dies are rinsed in deionized water and then with 2,2-propanol using the procedure described in Appendix A.3.5. The die is then gently dried under a nitrogen jet for 1 minute and is ready for testing.

3.3 Design and Process Improvements

This section describes design and process improvements in the micromotor and sensors. First, thermal diffusion effects on the sensor implants due to subsequent micromachining steps are examined using two dopant species with differing thermal diffusivities. Arsenic is chosen as a superior implant species because of its low thermal diffusivity. Second, an analysis of surface interfacial charge effects between sensors on threshold voltage indicates that a threshold shift implant is necessary to prevent

surface inversion which short circuits all sensors. A worst-case shift implant is chosen for the fabrication process to be used in conjunction with a thin passivating oxide at the wafer surface. Third, the different types of electrical shields and their uses is discussed. Fourth, the use of the sacrificial gap plug oxide during processing is described. Fifth, a new bearing/bushing design is evaluated. Sixth, the post-processing release step is studied in cantilever and doubly clamped beam arrays on three different underlying surfaces. Release yields are presented with and without the use of a hydrocarbon post-rinse. Finally, the fabrication of gold bearings by a lift-off technique and attempts to fabricate selective CVD tungsten bearings is described.

3.3.1 Sensor Implant Thermal Processing Effects

In most microelectromechanical processes incorporating integrated electronics beneath mechanical structures, electronic devices are fabricated before the mechanical structures are built. Thermal cycling during the construction of the mechanical structure often affects the electronics through thermal diffusion of electronic implants. In the micromotor process, thermal processing after sensor implants have been created can render sensors inoperable if sensor regions diffuse into one another, or if the photosensitive pn-junction diffuses beyond the depth of light penetration at the silicon surface. When designing a sensor process it is desirable to minimize high-temperature cycling and to use implant species with low thermal diffusivity.

SUPREM-III is used to examine one-dimensional diffusion profiles of the sensor and shield implant regions through the micromotor process sequence [39]. The micromotor process is modeled using both phosphorus and arsenic implants. Implant profiles are determined by SUPREM-III using process models such as then one given in Appendix B. Plots a) and c) in Figure 3.6 show the electronically active phosphorus concentrations at a dose of 5×10^{15} cm^{-2} and energy of 90 keV before the motor process steps and after the motor processing, respectively. The phosphorus junction has moved approximately 0.5 μm to a depth greater than 1 μm as a result of motor processing. Plots b) and d) in Figure 3.6 show the electronically active arsenic con-

centrations at a similar dose of 5×10^{15} cm^{-2} and energy of 90 keV before the motor process steps and after the motor processing, respectively. The arsenic junction has moved only 0.15 μm to a depth of 0.4 μm. As would be expected from its lower thermal diffusivity, the arsenic junction moves less as a result of motor processing. Arsenic is therefore chosen as the implant species because the lateral distance between some neighboring sensor implants can be as small at 1 μm. Since lateral implant diffusion can be 75%-85% of the vertical diffusion distance [32], the use of a phosphorus implant would risk neighboring sensors diffusing together. Another reason for choosing arsenic is that a junction operating as a photodiode at wavelengths of visible light is constrained to be within the photo transmission depth of the silicon substrate, which is typically 0.5 μm or less. If phosphorus had been used, the pn-junction would have moved by thermal diffusion outside the range of incident photon penetration reducing photodiode sensitivity.

3.3.2 Surface Passivation and Threshold Voltage Shift

To prevent unintended inversion at the silicon surface which could electrically connect neighboring sensor regions, the starting wafers receive a blanket boron ion implant to shift the threshold voltage toward deep depletion. An analytical analysis is used to compute the necessary implant dose and voltage threshold shift. A substrate doping of $N_A = 10^{15}$ cm^{-3} for the p-type wafer and a doping $N_D = 10^{20}$ cm^{-3} for the n-type polysilicon gate are typical process values. The thickness of the silicon nitride layer is $t_{Si3N4} = 4000$ Å. The interfacial ion surface charge concentration Q_{ss}/q is unknown and depends on the number of dangling bonds and trapped charge at the silicon surface. Four different interfacial ion concentrations are chosen for the computation: $Q_{ss}/q = 10^{10}, 10^{11}, 10^{12}$, and 10^{13} cm^{-3}. At a well passivated surface in a typical CMOS process, Q_{ss}/q is on the order of 10^{10} cm^{-3} [30]. Here an increase of up to three orders of magnitude in the interfacial charge concentration for LPCVD Si_3N_4 is hypothesized at the interface. As a process improvement, a 220 Å thick layer of thermal oxide is grown before nitride deposition to passivate the surface. The

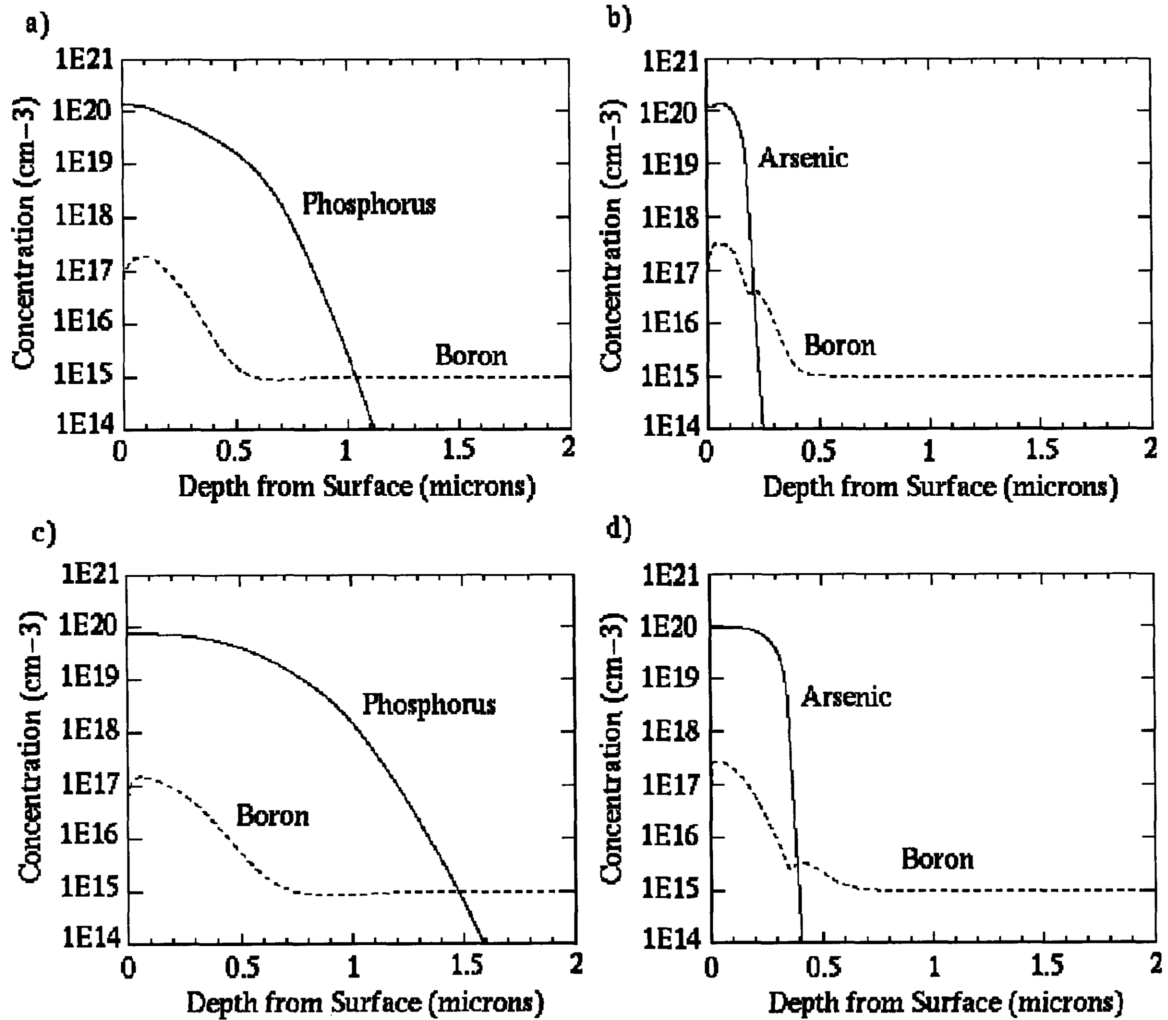

Figure 3.6: SUPREM-III active concentrations of a) phosphorus before micromotor process steps, b) arsenic before micromotor process steps, c) phosphorus after micromotor process steps, d) arsenic after micromotor process steps.

silicon nitride dielectric constant is $\epsilon_{Si3N4} \approx 4.8\epsilon_0$ where the permittivity of free space is $\epsilon_0 = 8.85 \times 10^{-14}$ F/cm.

The threshold voltage may be estimated as a sum of the gate-substrate work function difference, and voltages due to the substrate work function, the charge stored at the source/body depletion region at zero bias, and the interfacial surface charge

concentration [30]. This sum yields

$$V_T = \phi_{GC} - 2\phi_F(subst) - \frac{Q_{B0}}{C_{Si3N4}} - \frac{Q_{SS}}{C_{Si3N4}} \tag{3.1}$$

where ϕ_{GC} is the gate-substrate work function difference, $\phi_F(subst)$ is the substrate work function, C_{Si3N4} is the capacitance per unit area of the gate to substrate, Q_{B0} is the charge stored in the source/body depletion region at zero bias, and Q_{SS} is the interfacial charge concentration. The work functions of the substrate and gate are

$$\phi_F(subst) = \frac{kT}{q}\ln\frac{n_i}{N_A} \tag{3.2}$$

$$\phi_F(gate) = \frac{kT}{-q}\ln\frac{n_i}{N_D} \tag{3.3}$$

Evaluating the work functions with typical process parameters gives $\phi_F(subst) = -0.29$ V and $\phi_F(gate) = 0.59$ V. The difference in work function potentials is

$$\phi_{GC} = \phi_F(subst) - \phi_F(gate) \tag{3.4}$$

Evaluating this with the micromotor parameters gives a work function difference of $\phi_{GC} = -0.88$ V. The capacitance per unit area of the gate to the substrate is computed using the parallel plate capacitor approximation

$$C_{Si3N4} = \frac{\epsilon_{Si3N4}}{t_{Si3N4}} \tag{3.5}$$

Evaluating this capacitance with the micromotor parameters gives $C_{Si3N4} = 1.08 \times 10^{-8}$ F/cm^2. The charge stored in the source/body depletion region at zero bias [30] is given by

$$Q_{B0} = -\sqrt{2qN_A\epsilon_{Si}\left|-2\phi_F(subst)\right|} \tag{3.6}$$

Evaluating this charge density with the micromotor parameters yields $Q_{B0} = -1.4 \times 10^{-8}$C/cm^2. The source/body contribution to threshold voltage is then $Q_{B0}/C_{Si3N4} = -1.30$ V. The interfacial charge contribution to the threshold volt-

Q_{ss}/q [cm^{-2}]	Q_{ss}/C_{Si3N4} [V]	V_T [V]	Implant dose for $V_T = 0$ [cm$^-3$]
10^{10}	0.15	0.53	0
10^{11}	1.50	-0.82	5.5×10^{10}
10^{12}	15.0	-14.3	9.7×10^{11}
10^{13}	150	-149	1.0×10^{13}

Table 3.1: Surface charge concentration, contribution to threshold voltage, threshold voltage, and implant dose to shift to zero threshold voltage.

age $Q_{SS}/C_{Si3N4} = 0.15, 1.50, 15.0$, and 150 V for $Q_{SS}/q = 10^{10}, 10^{11}, 10^{12}$, and 10^{13} cm^{-2}, respectively. Finally, computing the threshold voltage from Equation 3.1 yields $V_T = 0.53, -0.82, -14.3$, and -149 V, respectively.

To shift the threshold voltage of the channel region, an implant of dose N_I may be used such that

$$\Delta V_T = \frac{N_I q}{C_{Si3N4}} \tag{3.7}$$

To shift the threshold voltage to zero (for no inversion layer) the threshold shift is set equal to the threshold voltage given by Equation 3.1, from which N_I is determined. The implant dose is then $N_I = 0, 5.5 \times 10^{10}, 9.7 \times 10^{11}$, and 1.0×10^{13} cm^{-2} for respective Q_{SS}. Only three implants are computed because one V_T is already positive. Since the actual Q_{SS} is unknown, an implant dose of 5×10^{12}cm^{-2} is chosen for the worst case of the most interfacial charge. Table 3.1 gives a summary for the various surface charge concentrations.

3.3.3 Electrical Shielding

Three electrical shields are necessary for operation of the micromotor and sensors. They are the rotor shield, sensor shield, and stator diffusion or implant shield. The rotor shield shown in Figure 3.1 is a 1500 Å polysilicon layer with sheet conductivity 20 $\Omega/\Box$. It is secured to the nitride insulator layer. The rotor shield layer decouples the rotor from vertically directed electric fields that could exist if the rotor and substrate were at different electric potentials. These fields could cause the rotor to pull-in to the substrate and increase the frictional torque acting on the rotor. With the shield

layer making electrical contact to the rotor through the bearing or bushings, electric fields between rotor and substrate are reduced or eliminated, in turn reducing or eliminating pull-down forces on the rotor and hence the frictional torque acting on the rotor.

The sensor shield shown schematically in Figure 3.1 is a 1500 Å optically transparent polysilicon layer with sheet conductivity 20 $\Omega/\Box$ placed on the die everywhere except via holes and beneath stators. The sensor shield acts to isolate the sensor implants from capacitive coupling with the stator electrodes as they switch. Figure 3.7 is an SEM of the sensor shield at a sensor interconnect via near a stator electrode. No sensor shield is placed at the via and in a small moat around the sensor interconnect from the via. This moat serves to limit lateral current that might be induced beneath the sensor interconnect. The sensor shield also serves to rapidly discharge to ground any charge accumulated at the nitride-oxide interface. The sensor shield is tied to four outer ground pads and the stator diffusion regions by at an outer grounding ring shown in the motor layout of Figure 3.4.

A stator shield created from arsenic implant regions beneath the stators, stator interconnect, and stator pads is formed from the same implant as the sensors. This stator diffusion shield acts as a low conductivity path to ground for charge induced at the silicon surface from the high-voltage switching of the stator electrodes.

3.3.4 Gap Plug

Bearing material sometimes remains in the rotor-stator gaps after an incomplete bearing etch as shown in Figures 3.8a and 3.8b. In the released gap, the residual bearing material acts as a wedge to impede rotor motion. It has been found useful to deposit a gap plug oxide to seal the gaps before bearing deposition as shown in cross-section R in Figure 3.3. The gap plug oxide eliminates potential problems of rotor obstruction due to residual bearing material. Before deposition of the bearing clearance spacer oxide, the etched gaps are filled with 1 μm low temperature oxide to seal the rotor-stator gap as shown in Figure 3.8d, and is removed at the bearing to

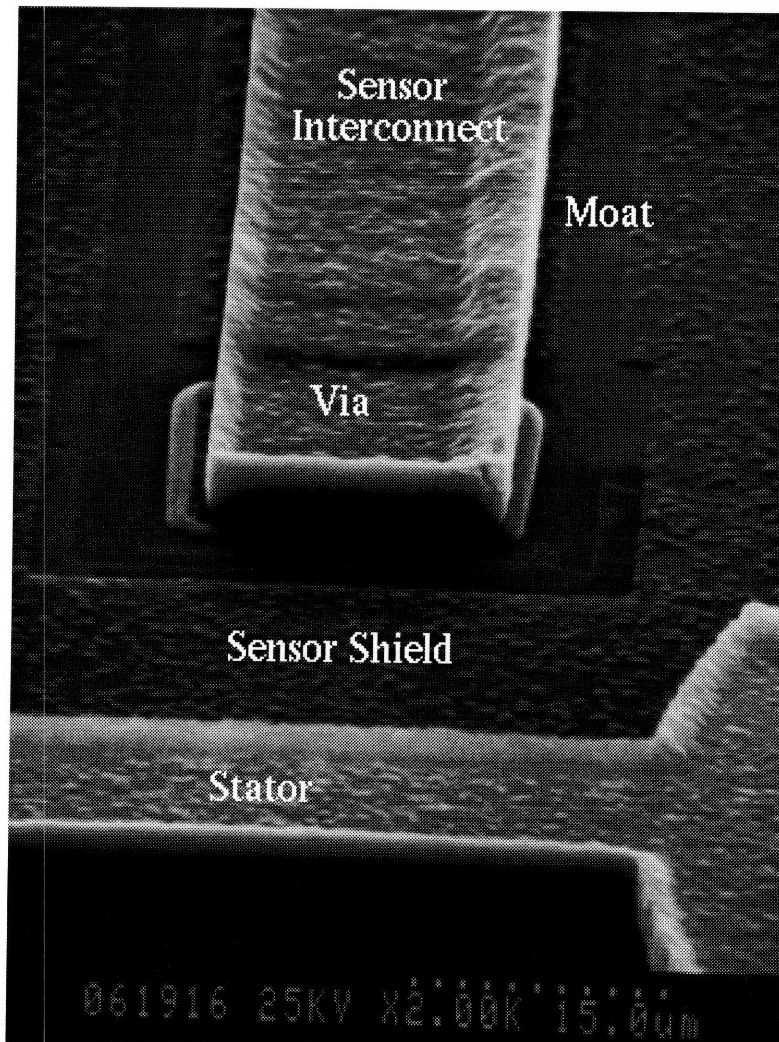

Figure 3.7: SEM of sensor interconnect showing sensor shield layer and moat. Below the via lies stator interconnect and electrode.

allow deposition of a thinner bearing gap clearance spacer oxide as shown in Figure 3.8c.

3.3.5 Flange-Collar Pin Bearing Design

The design of proper bearings and bushings is important to maximize motor lifetime and available drive torque. Macro-scale mechanical bearings permit smooth low-friction rotary or linear movement between two surfaces and are traditionally evaluated on how much load they can carry, at what speeds they carry this load, how long they will serve under specified conditions, friction, start-up torque/force, ability to withstand impact, rigidity, size, cost, and complexity [57, 90]. Often, macro-scale bearings consist of lubricated balls with friction minimizing contact pairs, often a hard surface in contact with a soft one. On the macro-scale, sliding bearings usually perform well up to moments before violent failure, as opposed to rolling bearings which give ample warning that they are approaching failure. A similar effect is observed in the micromotor where bearings fail violently when a wear particle gets stuck in the bearing gap or the rotor-stator gap [87]. In the micromotor, bearing/rotor wear has been shown to limit motor lifetime to as little a one minute [81].

The bearing requires the finest tolerances in the motor design since the bearing clearance must be less than the rotor-stator gap to prevent mechanical obstruction and electrical breakdown. Mask layout and etching introduce non-circularities in the bearing which further reduces the bearing clearance. Through self-alignment techniques the bearing is fabricated with a bearing clearance of 3000 Å determined by the sacrificial oxide film deposited laterally in the bearing hole of the rotor. In all bearing designs the retarding frictional torque is determined by the bearing radius which sets the retarding lever arm. It is desired that this radius be as small as possible.

Two main types of micromotor bearings have been fabricated in the past: the pin bearing shown in Figure 3.10a and the flange bearing shown in Figure 3.10b. Bearing designs may be varied by changing the location and size of the frictional contact

points or bushings. Conventional hemispherical micromotor bushings, as shown in Figure 3.9, are formed by time etching an underlying oxide layer to provide molds that form the later rotor polysilicon deposition [63, 87]. When the rotor is released, it rests on the hemispherical polysilicon bushings in contact with the underlying plane. Typically, 3 or 4 evenly spaced hemispheres or an annular ring are placed around the rotor just outside the bearing overhang at the smallest radius possible to decrease the lever arm and associated frictional retarding torque [59, 87]. Static experiments have not yet shown an area dependence effect on bushing friction [64]. Little frictional difference was shown between hemispherical bushings and an annular ring [59] supporting the theory that surface nonuniformities contact the supporting substrate or shield at three points. An annular ring has at any time three points of contact to stabilize the rotor. Similarly, the flange bearing has three points of contact to the substrate.

The new bearing design fabricated in this thesis is the flange-collar pin bearing shown in Figure 3.10c. The design goal of the flange-collar pin bearing is to combine the advantages of both traditional pin and flange bearings, providing greater tilt stability, and bringing frictional contacts close to the bearing to minimize the retarding torque level arm. Flange-collar bearings were found to behave similarly to standard pin bearings. A rotor with pin-flange bearing was removed and its underside is observed in the scanning electron micrograph shown in Figure 3.11. Sub-micron diameter protrusions were observed on the flange collar surface which may be acting as dimple bushings. The flange collar bearing rests on three points of contact, possibly at the dimple protrusions observed in Figure 3.11. In later fabrication runs the flange-collar pin bearing was replaced by the traditional hemispherical bushing pin bearings to simplify fabrication, since the flange-collar pin bearing offered no significant advantage over the standard pin bearing.

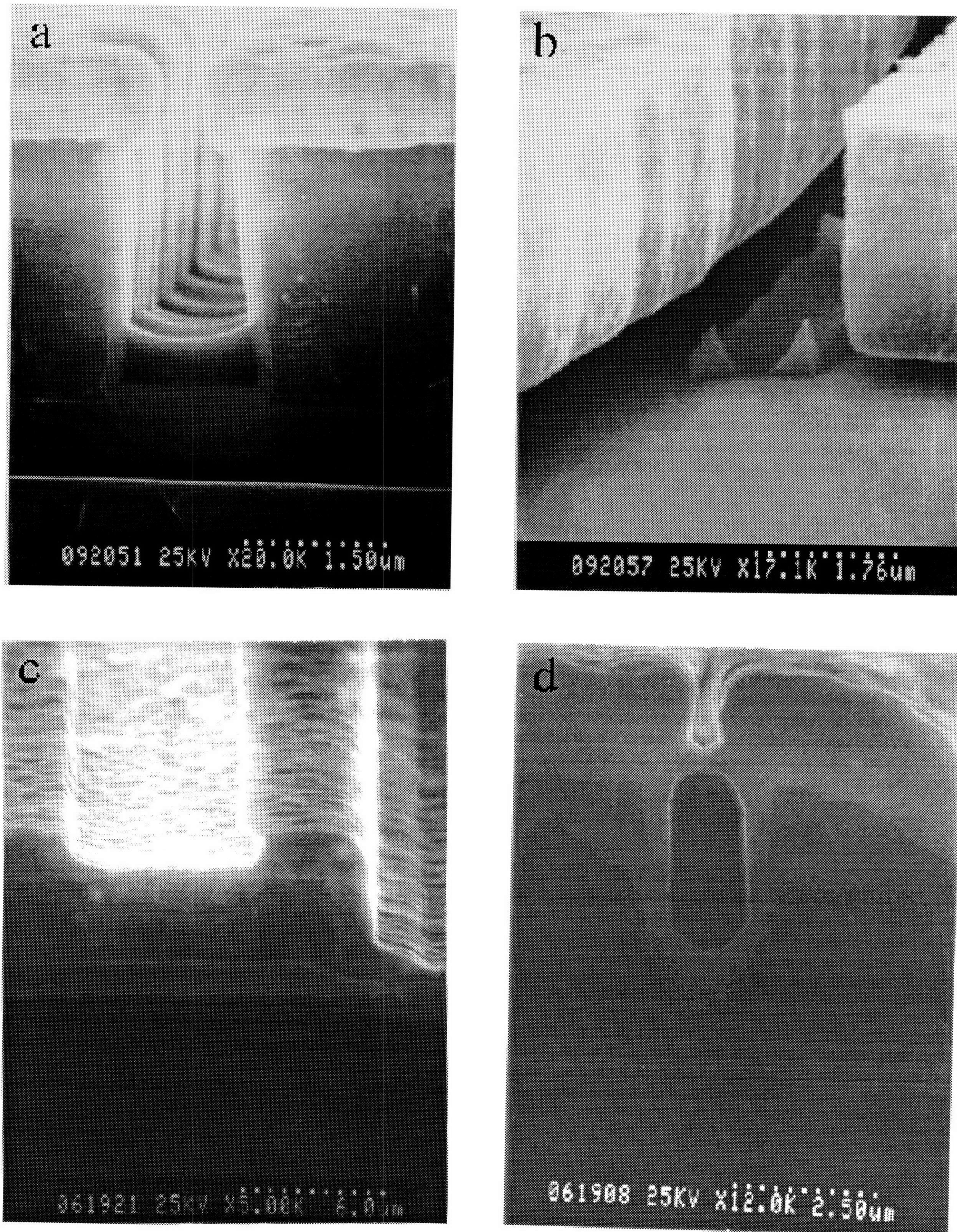

Figure 3.8: An oxide plug seals the rotor-stator gap before bearing material deposition. a) Unreleased gap cross section without plug oxide shows residual bearing material. b) Released gap with residual bearing material wedging rotor. c) Gap plug oxide and bearing. d) Unreleased gap with plug oxide seals gap.

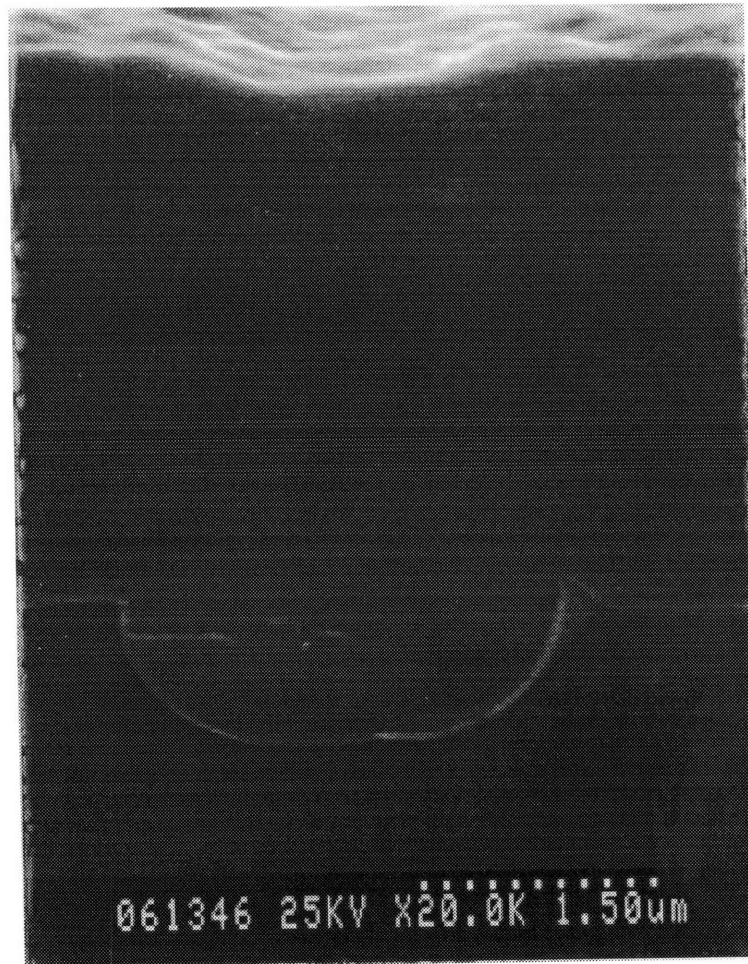

Figure 3.9: Cross-section of a conventional unreleased hemispherical micromotor bushing.

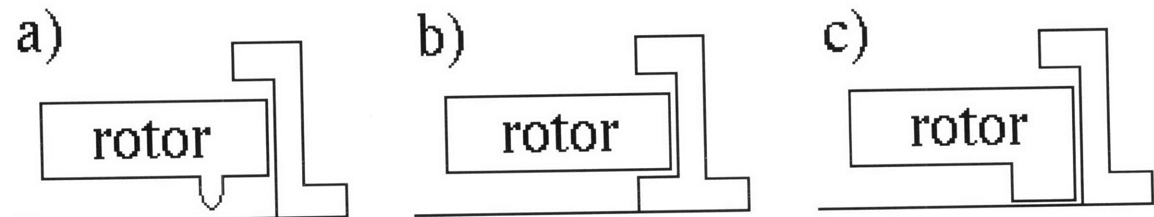

Figure 3.10: Micromotor bearing designs: a) pin bearing with dimple or collar bushing, b) flange bearing, and c) flange-collar pin bearing.

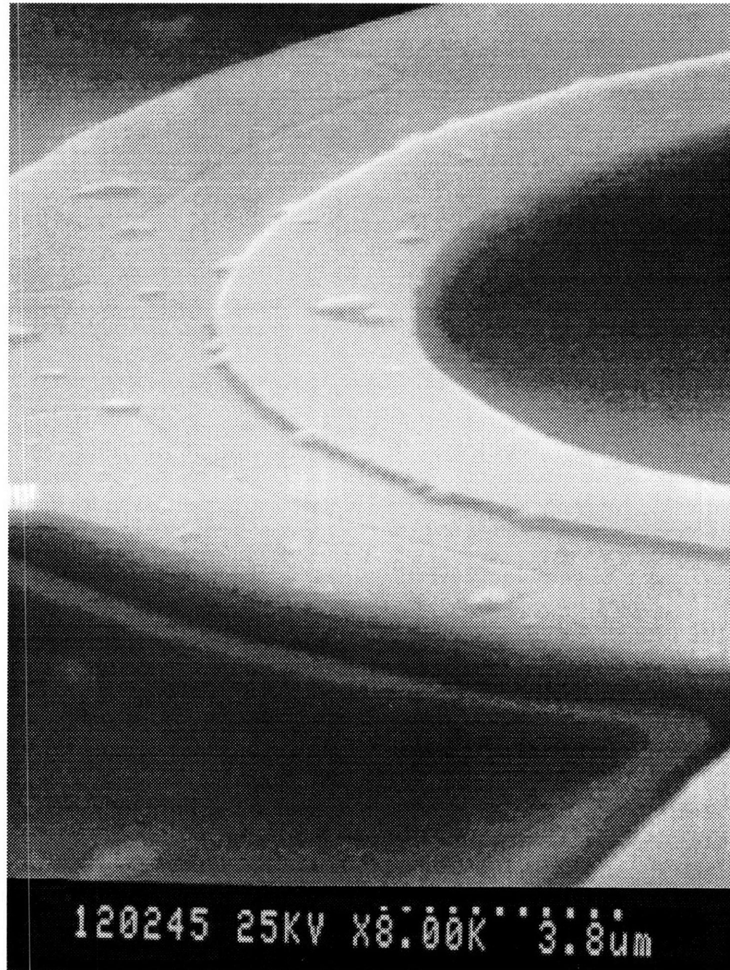

Figure 3.11: Rotor underside with flange-collar pin bearing exhibiting dimple protrusions.

3.3.6 Post-Processing Release

Post-processing release involves an isotropic wet etch which removes the sacrificial oxide supporting the rotor during fabrication, and allowing it to move freely. Side-effects from the release process have been found to cause rotor sticking and are a challenge to overcome in many surface micromachining processes. Most of the sacrificial oxide release processes are based on hydrofluoric acid (HF) etches with a variety of post-rinses, drying, or sublimation steps. The effectiveness of the release step depends on the relative etch-resistance of the other materials in the motor compared to that of the sacrificial oxide. Tavrow found that the room temperature etch speed in a test structure designed to measure etch rates in long channels was independent of channel width from 1 μm to 30 μm [87]. All micromotor geometries are undercut before slow-down in etch rate from diffusion limited etching dominates the etch. In a typical micromotor the sacrificial oxide is etched away in thicknesses as little as 2000 Å over lateral distances greater than 5 μm. When this isotropic etch is performed in concentrated HF, the undercut speed is typically 1 μm per minute for low temperature oxide.

In the first micromotor release processes, buffered hydrofluoric acid (BOE) was used as the oxide etchant. The buffering agent of ammonium fluoride (NH_4F) improves oxide etch rate uniformly and reduces photoresist attack [32]. However, it was found that the solid residue from the buffering agent seemed to attack the high-content of phophosilicate glass found in the phosphorus-doped polysilicon grain boundaries, decreasing its etch resistance [55]. Micromotor release processes were changed to use concentrated HF-only etches that did not attack the polysilicon and etched oxide at a faster rate than BOE. Concentrated-HF etches also improved the relative nitride etch rate which was useful during long etches [87].

After the release etch, the micromotor was typically placed in a de-ionized water (DI) rinse to remove and remaining HF. The DI rinse was shown to enhance native oxide formation on any exposed silicon surfaces which worsened motor performance [59]. Incomplete rinsing was thought to leave fluorine resides that could also aid

in rotor sticking [36]. Surface tension effects as the rinse water leaves the rotor was postulated to cause sticking leading others to rinse in fluids with lower surface tension such as liquid CO2, freeze dry, or sublime the rinse fluid.

The micromotor release process used in this thesis has been refined to the recipe described in Appendix A.3.5, which incorporates a room temperature liquid 2,2-propanol (IPA) dilution and rinse. A release test lot with singly and doubly clamped polysilicon beams was processed in parallel with the micromotor sensor process. Beam arrays approximately 2.5 μm thick and 10 μm wide, varied in length from 10 μm to 200 μm in increments of 10 μm. The sacrificial oxide was a 1 μm low temperature oxide. Three sub-lots were run to investigate the effect of different underlying beam contact materials. The first sub-lot was a single crystal silicon underlying contact (the wafer substrate), a second sub-lot had a 4000 Å layer of silicon-rich silicon nitride as the underlying contact, and the third sub-lot had a 1500 Å of LPCVD polysilicon underlying contact. Each type of array was subject to the same release etch, with and without the IPA dilution/rinse steps. Observation of fringes in released beams under a microscope with 10x regular interferometer objective, showed qualitatively that the released beams exhibited two modes of sticking (I and II) as illustrated in Figures 3.12a and 3.12b. A sample size of 35 arrays were examined for each substrate and recipe. In both modes the affected beam came into contact with the underlying contact material. Mode I sticking is a contact just at the tip of the beam, and mode II sticking is a contact over a larger area at the tip end of the beam.

The yield curves shown in Figure 3.13 are for the combination of mode I and mode II sticking in the singly-clamped polysilicon beams, where yield is defined as the percentage of beams exhibiting neither mode I nor mode II sticking. In the combined mode I and mode II case, the limiting beam length for no sticking is 110 μm. All beams above 110 μm exhibited either mode I or mode II sticking. The IPA rinse improved beam release yield in both the polysilicon underlying contact and single crystal silicon nitride contact. The silicon nitride underlying contact is at its length limit even with no IPA post-rinse.

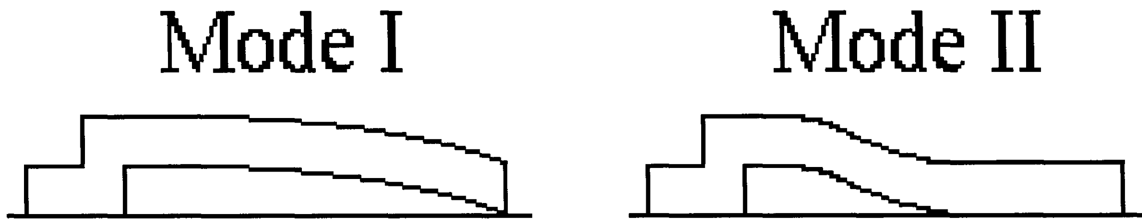

Figure 3.12: Sticking modes I and II.

The yield curves shown in Figure 3.14 are for mode II sticking only in the singly-clamped polysilicon beams, were yield is defined as the percentage of beams not exhibiting mode II sticking. These beams may exhibit mode I sticking and are still considered released. The limiting beam length was not observed and is greater than 200 μm. The IPA rinse greatly improves beam release yield in the case of an underlying single crystal silicon substrate, and improves to 100% the release yields in the cases of polysilicon and silicon nitride underlying contact for beams less than 200 μm long.

The yield curves shown in Figure 3.15 are for mode II sticking only in the doubly clamped polysilicon beams, were yield is defined as the percentage of beams not exhibiting mode II sticking. Mode I sticking was not observed in the doubly clamped beams. A limiting beam length was not observed in beams less than 200 μm long. The IPA rinse greatly improves beam release yield in the case of an underlying single crystal silicon substrate, and improves to 100% the release yields in the cases of polysilicon and silicon nitride underlying contact for beams less than 200 μm long.

The conclusions of this release study are that IPA rinse improves release yield for all three underlying substrates in both singly and doubly-clamped polysilicon beams for both modes I and II sticking. Polysilicon and silicon nitride underlying contact materials offer improved release yield over single crystal underlying contact material.

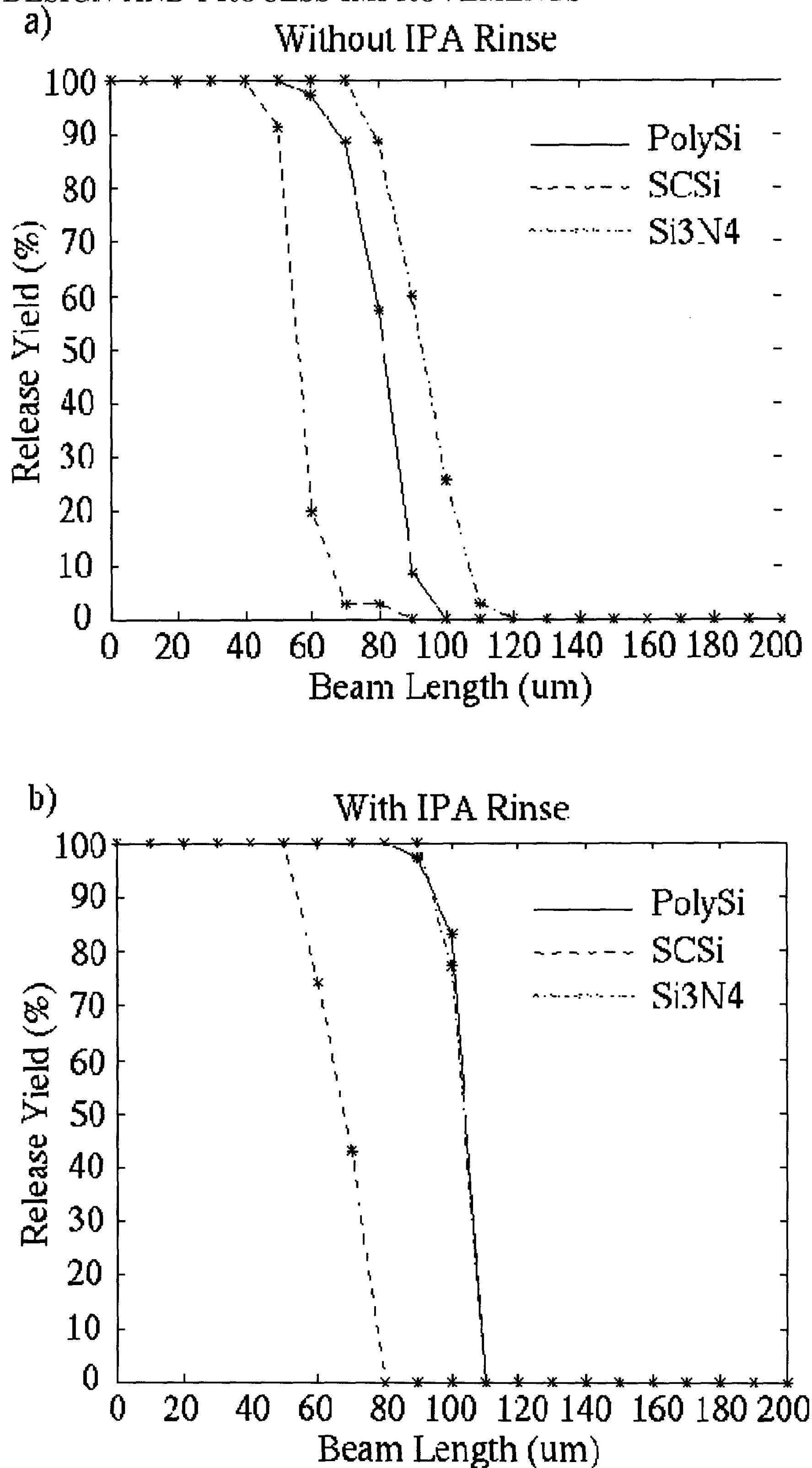

Figure 3.13: Release yield in singly-clamped beams exhibiting modes I and II sticking. a) Without IPA rinse. b) With IPA rinse. The sample size for each substrate and release recipe is 35 arrays.

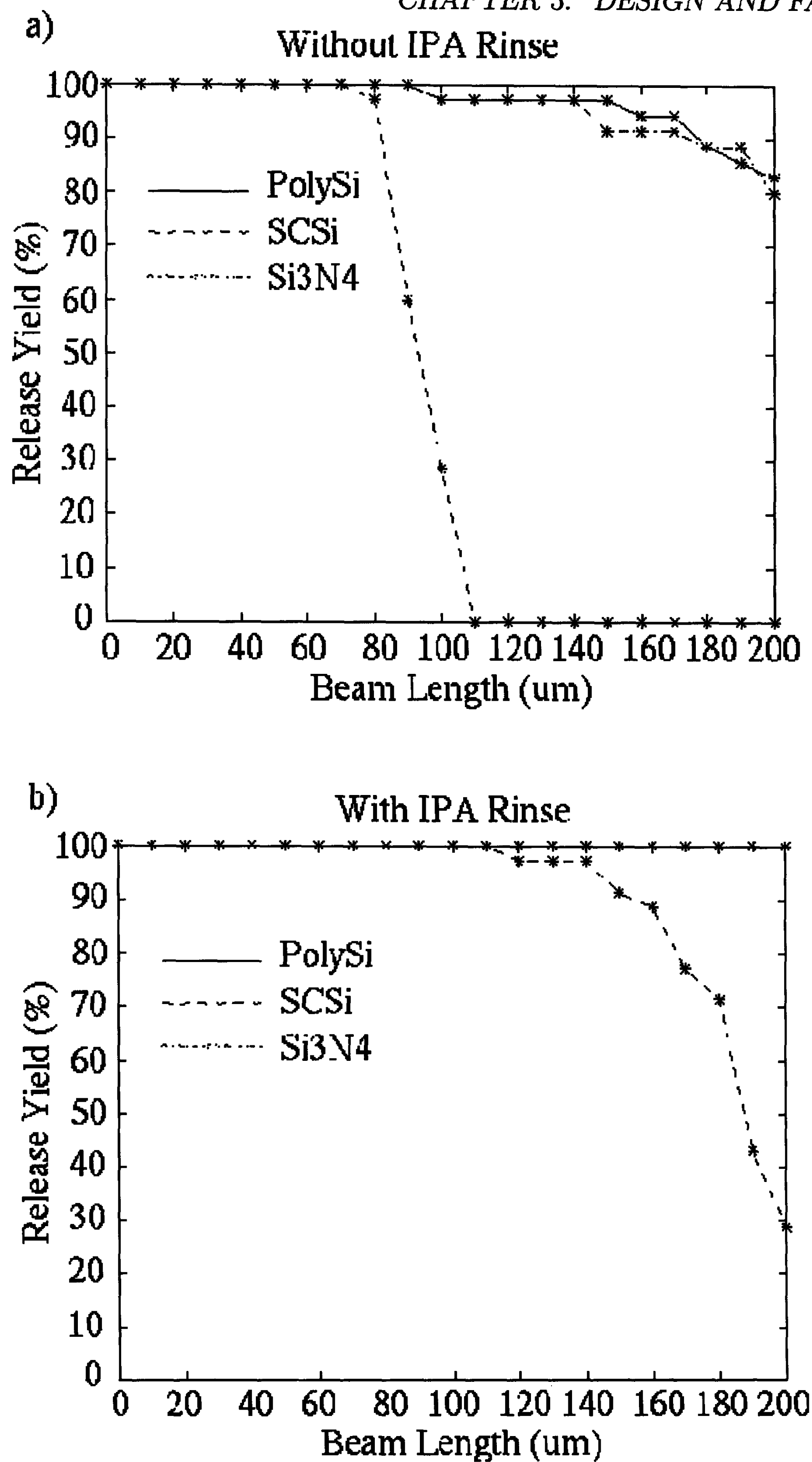

Figure 3.14: Release yield in singly-clamped beams exhibiting only mode II sticking. a) Without IPA rinse. b) With IPA rinse. The sample size for each substrate and release recipe is 35 arrays.

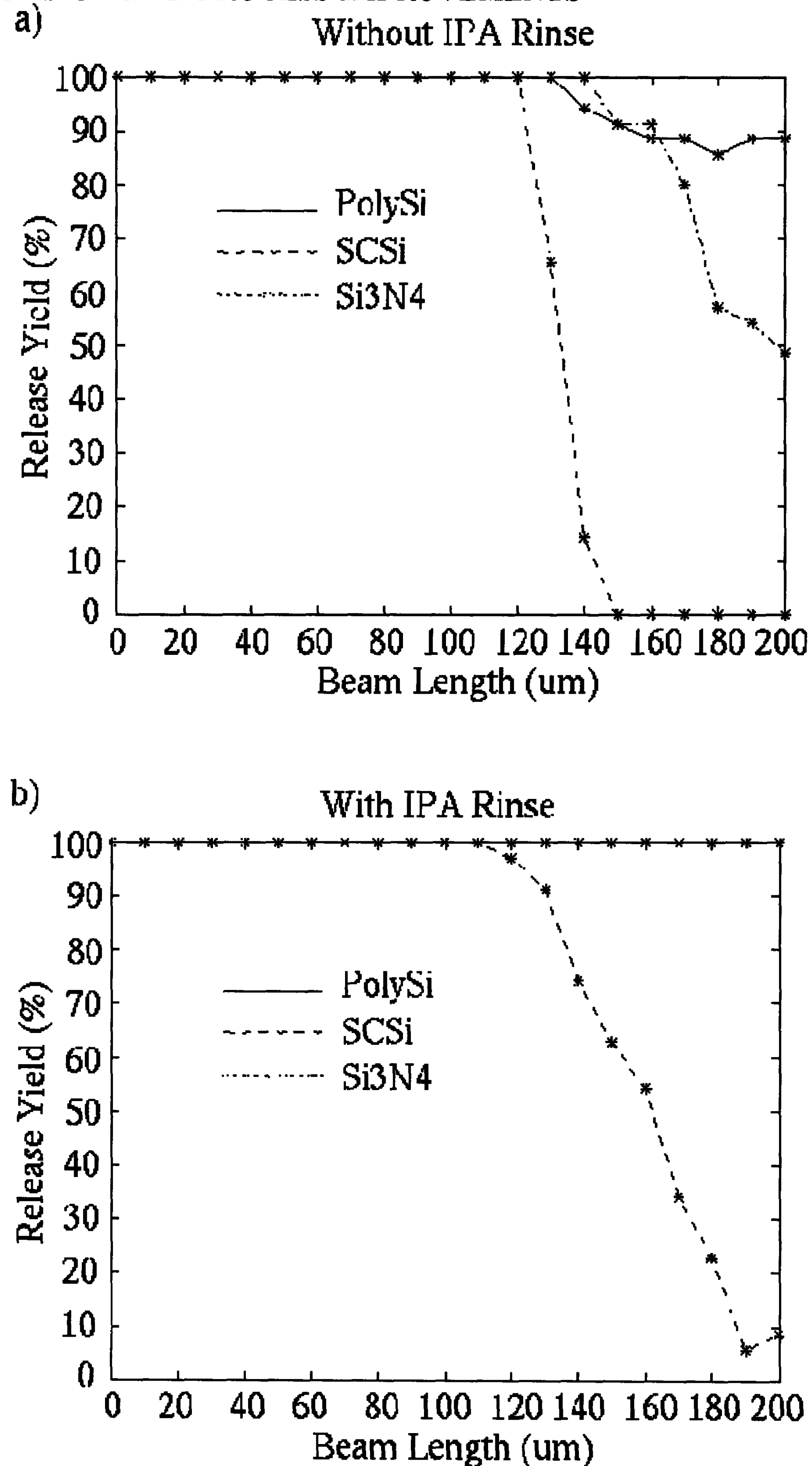

Figure 3.15: Release yield in doubly-clamped beams exhibiting only mode II sticking. a) Without IPA rinse. b) With IPA rinse. The sample size for each substrate and release recipe is 35 arrays.

3.3.7 Bearing Materials

Three materials have been incorporated into the micromotor process as bearing materials: LPCVD silicon-rich silicon nitride, e-beam evaporated gold, and selective CVD tungsten. Silicon nitride is well known to be a high performance bearing material exhibiting fatigue properties exceeding those of high quality bearing steels. The polysilicon-nitride contact has been studied by Fan [23] where solid silicon nitride bearings were fabricated and Tavrow [87] where silicon nitride was used as a solid-lubricant bearing coating. LPCVD stochiometric nitride is a tensile material with residual stress of 1.1 GPa which cracks at a yield strength of 2.0 GPa [14]. Stochiometric LPCVD nitride is useful for mechanical purposes only to a maximum thickness of about 4000 Å before interfaces and materials in contact are affected, or the film cracks itself. In this thesis, silicon-rich nonstochiometric nitride is deposited with a dichlorosilane-to-ammonia flow rate ratio of 10:1 for lower intrinsic stress to thicknesses in excess of 10000 Å. It is found to offer superior bearing performance and is used for the later motion studies. Figure 3.16 shows two solid silicon-rich silicon nitride bearings.

The second type of bearing incorporated into the micromotor process was an e-beam evaporated gold bearing that was deposited and patterned outside of the clean room using a photoresist lift-off technique. Gold is a relatively softer material than the polysilicon rotor. In macro-scale bearings a hard surface is often matched with a softer one where the soft surface self-lubricates the contact pair. Free standing gold bearings were fabricated, but not tested in moving motors because of fabrication complexity. Figures 3.17 show free standing e-beam evaporated gold bearings that were patterned with a negative photoresist mask. Subsequent to gold deposition, the negative photoresist mask is dissolved in acetone and excess gold is lifted off in a bath vibrating at ultrasonic frequencies. Figure 3.17a shows a free standing test gold bearing structure fabricated only with a negative resist mask on a silicon substrate. Figure 3.17b shows a gold bearing in a micromotor. A shadow of e-beam deposition on the inner rim of this bearing causes incomplete step coverage as shown

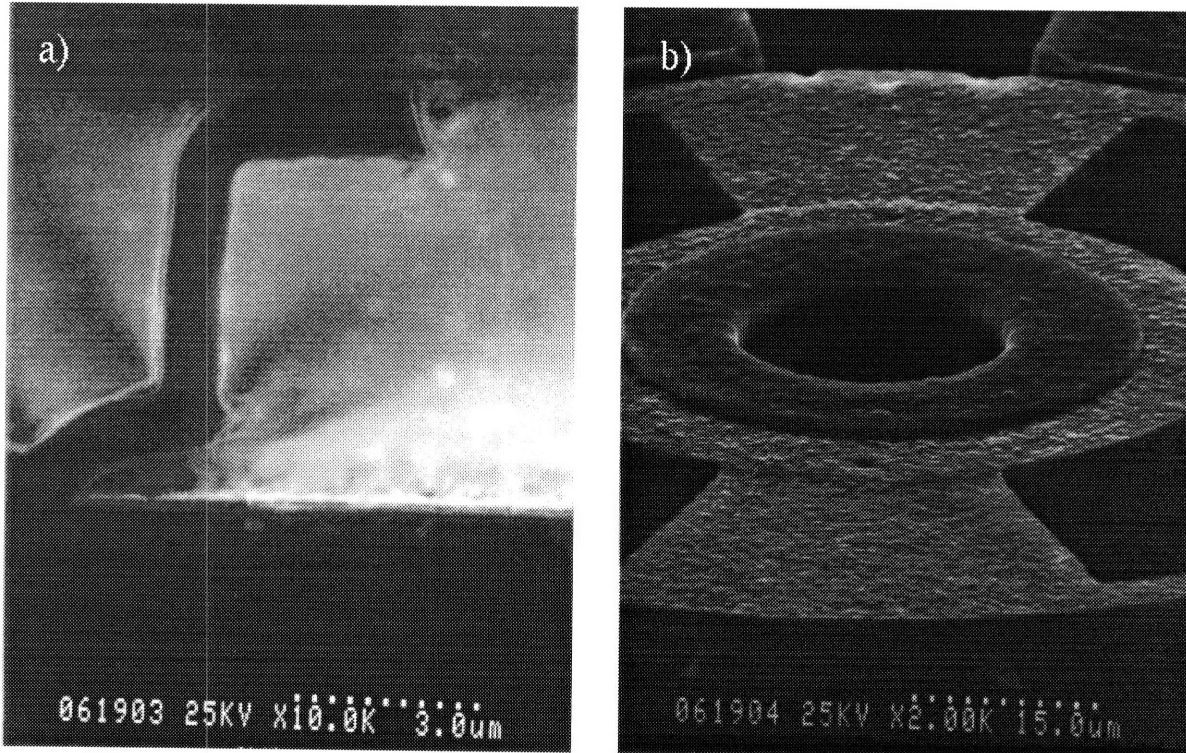

Figure 3.16: Silicon-rich silicon nitride bearings. a) Released cross-section of a silicon nitride bearing without rotor. b) Top-down view of a silicon nitride bearing.

in Figure 3.18, making the bearing structurally unsound and not able to operate. Through these studies it was learned that some bearing materials not available in the fabrication clean room may be deposited outside of the clean room and can be patterned by lift-off. Requirements for these bearing materials are a high HF etch resistance and brittleness suitable for resist lift-off.

The third type of new bearing material was deposited using a selective CVD tungsten process by ULVAC Technologies, Inc. of Andover, MA. Wafers were pre-treated with a 100:1 DI:HF etch to remove native oxide at the bearing anchor, followed by an NF_3 plasma pre-etch for 60 sec. With a deposition chemistry of SiH_4 reducing WF_6, selective tungsten thicknesses of 1.8–2 μm were achieved. CVD tungsten nucleates and grows selectively on the silicon bearing anchor to a greater extent than on silicon oxide. The goal of these bearings was to create mushroom shaped bearing structures which nucleated selectively at the bearing anchor to grow up and over the rotor.

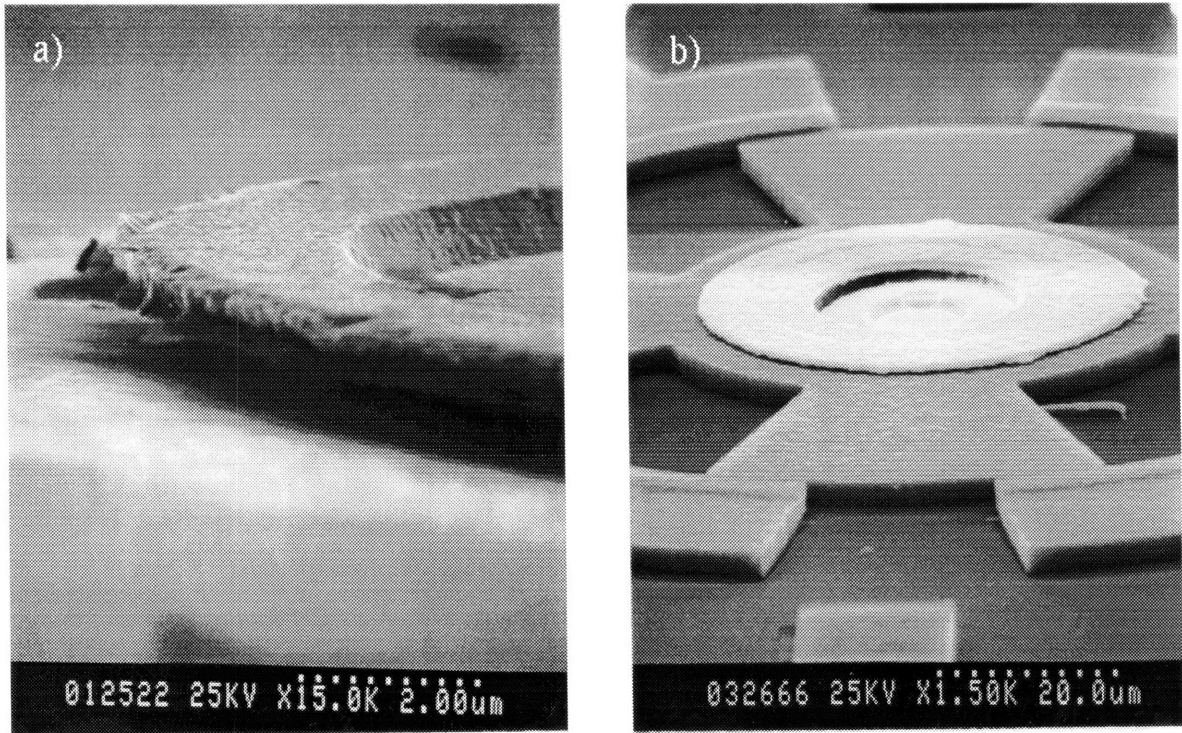

Figure 3.17: E-beam evaporated gold bearings fabricated by ultrasonic lift-off with a negative photoresist mask. a) Free-standing test gold bearing structure fabricated only with negative photoresist mask on the silicon substrate. b) Gold bearing in a micromotor. The shadow of e-beam deposition at the inner rim of the bearing causes incomplete step coverage, making this bearing structurally unsound and inoperable.

There would be no need for the pattern and etch step of the bearing material since bearings would naturally form a bearing cap. Figure 3.19 show the results of the selective CVD tungsten bearing deposition. Figures 3.19a and 3.19b show attempts to selectively grow a bearing at a silicon nucleation site with an oxide field surrounding. The bearing growth in the vertical direction is slower than the additional nucleation of tungsten on the oxide. Figures 3.19c and 3.19d show attempts to grow selective tungsten bearings in actual motors. The growth of tungsten around the stators, and in the gap before significant amounts have mushroomed to form a bearing cap, made these motors inoperable. Through these experiments it was learned that selective bearing growth, if successful, could offer reduced fabrication process complexity by eliminating bearing definition and etch steps. However, higher-selectivity growth

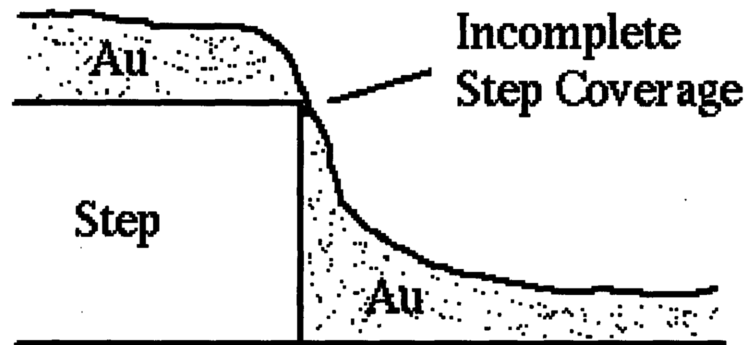

Figure 3.18: Incomplete bearing step coverage by e-beam evaporated gold.

recipes are necessary to obtain useful bearings with sufficient bearing overhang to hold the rotor to the substrate.

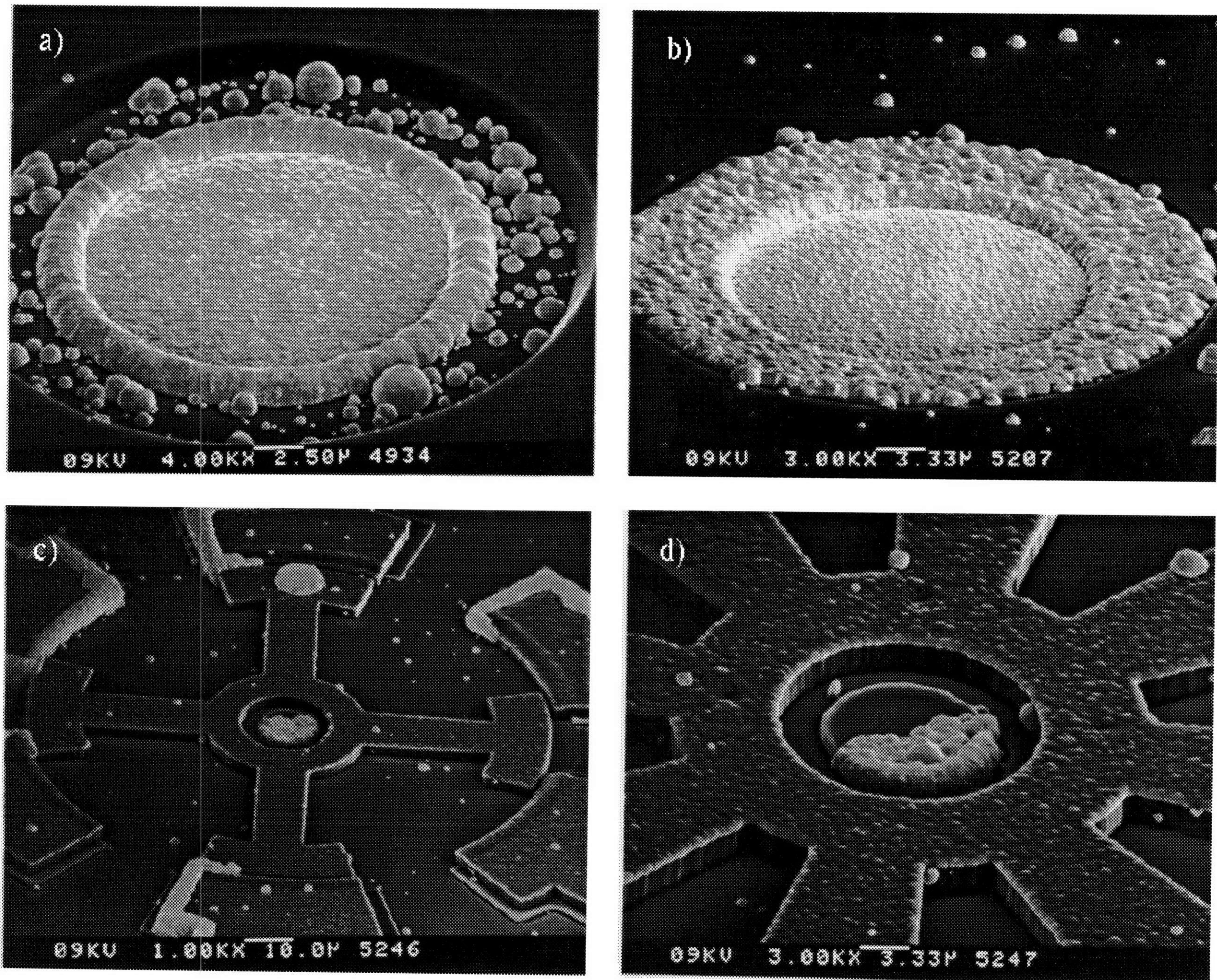

Figure 3.19: Experimental selective CVD tungsten bearings. Photos a) and b) show attempts to selectively grow a tungsten bearing at a silicon nucleation site with an oxide field surrounding it. The bearing growth in the vertical direction is slower than the additional nucleation of tungsten on the oxide. Photos c) and d) show attempts to grow selective tungsten bearings on actual motors. Poor selectivity observed in the growth of tungsten around the stators, and in the gap before significant amounts have mushroomed to form a bearing cap made these bearings inoperable.

Chapter 4

Testing

4.1 Overview

This chapter describes experimental testing of micromotors fabricated with integrated photodiode motion sensors. The experiments are partitioned into five sets. The first set of experiments establish that the photodiode sensors are sensitive to light variations and characterize their operating parameters. The second set of experiments characterize the ability of a sensor to respond to rapid light variations in time. Response to strobed light pulses gives an indication of motion acquisition bandwidth and is determined to be of sufficiently fine time resolution for subsequent motion studies. In the third set of experiments, the functionality of the sensors working as a group to detect the static position of the rotor is examined. This set of experiments verifies that each sensor is individually functioning, that the off-chip amplification and low-pass filtering electronics are functioning, and that the position extraction algorithm is correct.

The fourth set of experiments explores sensor operation in the presence of switching stator drive voltages. Two types of electrical switching interference are observed in the sensor signal. The first interference is a transient above-substrate capacitive coupling between the stator drive probes and sensors. The second interference is a polarity-dependent level-shift coupling to the drive voltage explained by parasitic transistor action in the device. The final set of experiments continuously measure, for the first time, rotor motion as driven by a gas jet and electrical excitation. Rotor position, velocity and acceleration are quantified. Several cases of electrical excitation are presented including electrical rotor clamping/braking, binary shutter excitation, and forward stepping motion of a gas levitated motor.

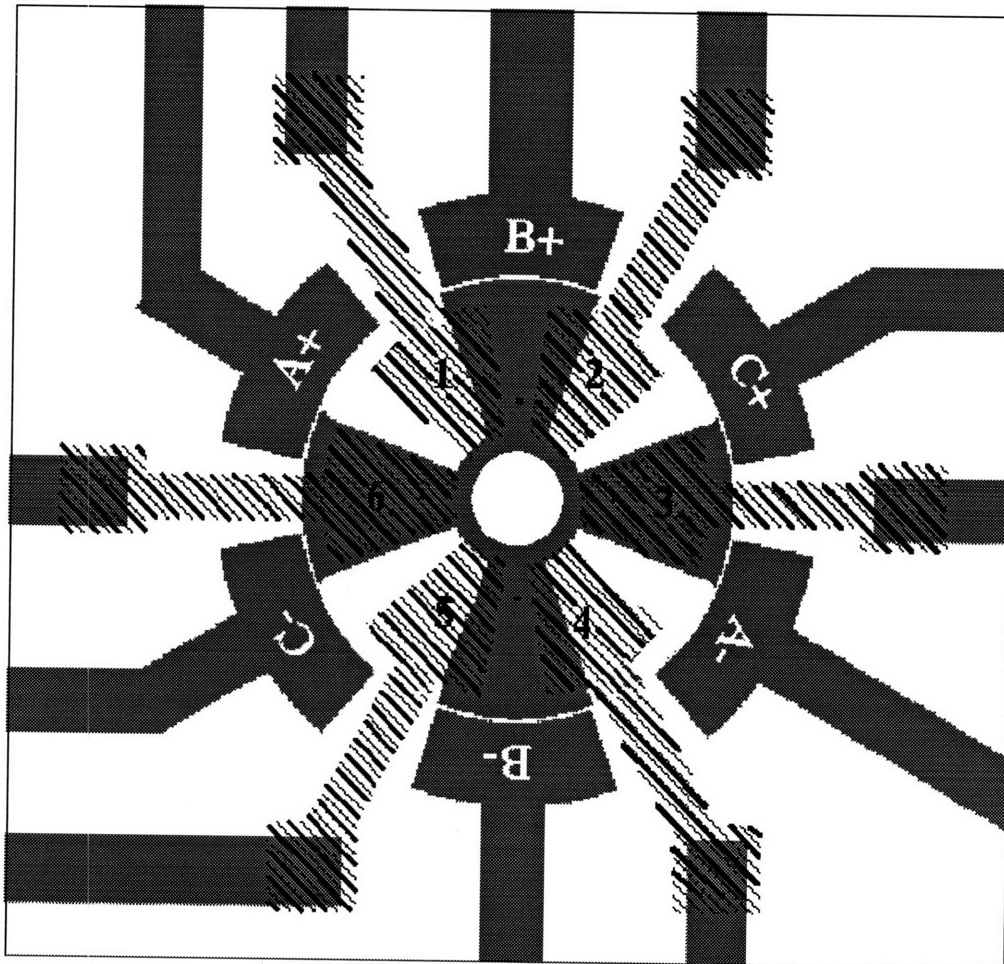

Figure 4.1: Plan view reference for sensor and stator locations when testing a micromotor. The stators are shown in dark gray and phases are referred to by A+, A-, B+, B-, C+, and C-. The sensor regions are shown as hashed lines and are referred to by the numerals 1, 2, 3, 4, 5, and 6. The rotor is shown on top of the sensors in dark gray. The bearing is not shown in this figure.

The motor and sensor plan view in Figure 4.1 will be used as a reference for sensor and stator probe locations in the experiments. Experimental testing was performed on ordinary side drive motors as shown in Figure 1.1 with sensor polysilicon and stator diffusion shielding. These motors have solid silicon-rich silicon nitride bearings. Testing is performed with Wentworth Model MP0920 probe station, Tektronix Model TDS540 oscilloscope, Hewlett Packard Semiconductor Parameter Analyzer Model HP4145, BK Instruments power supply, and a GenRad Strobotac.

4.2 Photodiode Characterization

This section establishes the photosensitivity of the sensors and describes the measurement of the device parameters necessary for use in signal and noise analysis.

4.2.1 Diode IV response to AC modulated light source

In this experiment Sensor 1 in Figure 4.1 is connected to the HP4145 in an $i - v$ sweep mode to generate the $i - v$ diode characteristic shown in Figure 4.2. The die backside is grounded. The incandescent light source of the microscope is used for illumination at two intensity levels. The light source is driven by a 60 Hz sinusoidal voltage, creating a 120 Hz light intensity variation visible as an aliased signal in Figure 4.2. The sweep rate of the HP4145 is slower than the 120 Hz intensity variation of the light source causing aliasing in the reverse biased portion of the $i - v$ traces. Later motion experiments replace the AC light source drive with a DC drive to remove the light source AC intensity fluctuation which would interfere with rotor motion signals at similar frequencies. The diode $i - v$ characteristic between -1.0 V and 1.0 V is observed to give currents in the range of -80 nA to values greater than 100 nA during forward bias. The three cases of no light, low-intensity light, and high-intensity light are shown. Typical $v = 0$ V photocurrent levels are in the range of 0 nA to 80 nA under incandescent bulb illumination. The forward voltage at $i = 0$ nA is typically in the range of 0.3 V to 0.4 V. This experiment has established the sensitivity of the photosensors to an AC modulated light source.

4.2.2 Quantum efficiency

The photodiode quantum efficiency η is defined as the number of carriers generated per incident photon and is measured experimentally by manually sweeping a HeNe laser (Spectra Physics Model 132) with a spot diameter of 2 mm at wavelength $\lambda =$ 632.8 nm. The total power over the spot is measured to be $P_T = 3.8$ mW using a power meter (Newport Optical Model 835) with a 1000x attenuation filter. When

the laser is passed over a zero biased sensor region, a peak photocurrent of $I_p = 450$ nA is measured in time as shown in Figure 4.3. Assuming single-mode lasing, power is distributed as a Guassian shape over the laser spot. In order to simplify the calculation a uniform power distribution over the laser spot is assumed. In this case the optical power incident on the sensor is the laser power P_T scaled by the ratio of the sensor area to the spot area. A typical sensor area of 1.13×10^{-9} m^2 receives approximately $P_S = 1.37$ μW of optical power incident at the top surface of the silicon nitride insulation layer shown in cross section in Figure 3.1.

Only a fraction of the incident optical power is transmitted through the intermediate layers comprising a 4000 Å (0.63λ) silicon nitride insulator, 1000 Å (0.16λ) polysilicon sensor shield, 220 Å (0.04λ) passivation oxide, and 5000 Å (0.79λ) into the implanted substrate to the photodiode junction. Assuming normal incidence of plane waves at the wavelength $\lambda = 632.8$ nm, and neglecting conductivity in the silicon nitride and passivation oxide layers, the power transmission through the four layer dielectric may be modeled as four cascaded TEM transmission lines in series as shown in Figure 4.4. The permeability μ is assumed to be equal to the permeability of free space μ_0 everywhere since none of these materials are magnetic.

In the transmission line analogy, voltage and current at the load (the photojunction) are determined as cascade of four matricies according to [79]

$$\begin{bmatrix} V_S \\ I_S \end{bmatrix} = \overline{\overline{T}}_4 \cdot \overline{\overline{T}}_3 \cdot \overline{\overline{T}}_2 \cdot \overline{\overline{T}}_1 \begin{bmatrix} V_L \\ I_L \end{bmatrix} \tag{4.1}$$

where the ith matrix $\overline{\overline{T}}_i$ is of the form [79]

$$\overline{\overline{T}}_i = \begin{bmatrix} \cos k_i \ell_i & jZ_i \sin k_i \ell_i \\ jY_i \sin k_i \ell_i & \cos k_i \ell_i \end{bmatrix} \tag{4.2}$$

The characteristic impedance of each medium is inversely proportional to the square root of the permittivity in the medium. The permittivities are ϵ_0 for air, $\epsilon_4 = 7.5\epsilon_0$

for amorphous silicon nitride [80], $\epsilon_3 = 11.9\epsilon_0$ for polysilicon [80], $\epsilon_2 = 3.9\epsilon_0$ for oxide [80], and $\epsilon_1 = 11.9\epsilon_0$ for the silicon wafer [80]. These give characteristic impedances in each medium of $Z_0 = 377\ \Omega$ for air, $Z_4 = 0.37Z_0$ for silicon nitride, $Z_3 = 0.29Z_0$ for polysilicon, $Z_2 = 0.51Z_0$ for oxide, and $Z_1 = 0.29Z_0$ for the silicon wafer. To account for conductive losses in the polysilicon and single crystal silicon, the conductivity σ of these layers is introduced as an imaginary part of a complex permittivity $\bar{\epsilon} = \epsilon + \frac{\sigma}{j\omega}$. A nominal conductivity of 0.1 S/cm is used for the polysilicon and single crystal silicon at a frequency of $\omega = 3.0 \times 10^{15}$ sec^{-1}.

Using the wave number definition $k = \frac{2\pi}{\lambda}$ with the thickness of each medium in terms of the laser wavelength, $k_4\ell_4 = 1.26\pi$ for the silicon nitride, $k_3\ell_3 = 0.32\pi$ for the polysilicon, $k_2\ell_2 = 0.08\pi$ for the oxide, and $k_1\ell_1 = 1.58\pi$ for the silicon substrate. Computing the composite matrix product of the cascaded transmission lines yields

$$\begin{bmatrix} V_S \\ I_S \end{bmatrix} = \begin{bmatrix} -0.69 & 0.0002 - 81.31j \\ -0.0064j & -0.69 \end{bmatrix} \begin{bmatrix} V_L \\ I_L \end{bmatrix} \tag{4.3}$$

The optical power P_S of the laser incident of the top surface (the source) is

$$P_S = \frac{1}{2}\Re(V_S I_S^*) \tag{4.4}$$

A similar equation exists for the load power P_L. Applying the composite matrix Equation 4.3 to compute the load power in terms of the source power gives

$$P_L = 0.98 P_S \tag{4.5}$$

The quantum efficiency is the ratio of photogenerated carrier flow rate over incident photon rate, and is given by

$$\eta = \frac{I_p/q}{P_L/h\nu} \tag{4.6}$$

where $h\nu/q = 1.24/\lambda(\mu m)$. Given the data above, the quantum efficiency is ap-

proximately 65%, which appears to be quite low. A possible source for error in the calculations above is the assumption of uniform power distribution over the laser beam spot. If the region of peak power density did not pass over the sensor region, then the illumination power would be lower, leading to an increased quantum efficiency. A second source of error is that the model presented above does not take surface recombination at the layer interfaces into account. Such recombination would prevent photons from reaching the photodiode depletion region. The photon flux incident on the depletion region would be less and hence the quantum efficiency would be higher.

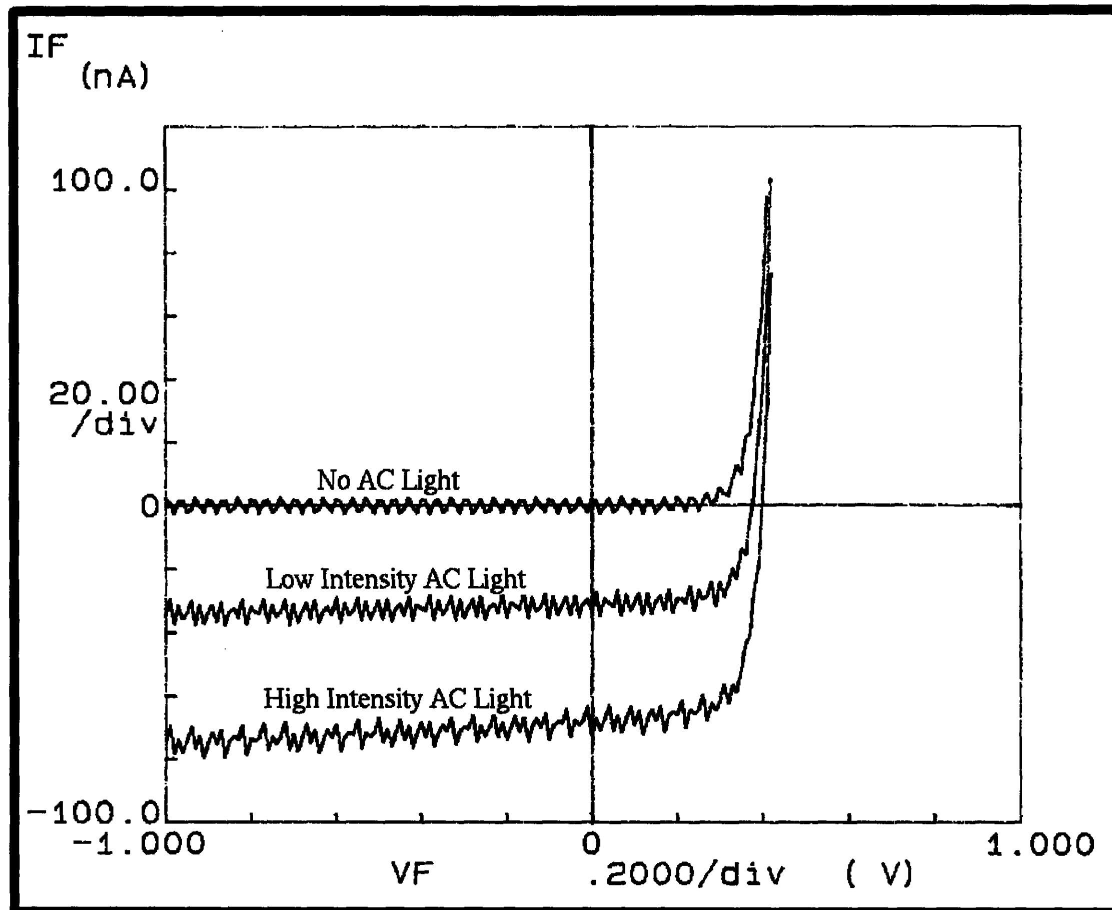

Figure 4.2: Photodiode $i-v$ response under incandescent AC light illumination. Incandescent light from the microscope is used to observe the diode photocurrent under dark, low intensity, and high intensity conditions. The sweep rate of the HP4145 is slower than the 120 Hz intensity variation of the light source causing aliasing in the reverse biased portion of the $i-v$ traces. Some 60 Hz AC line coupling to the probes may also be observed in the dark signal. Typical $v = 0$ V photocurrent levels are in the range of 0 nA to 80 nA under incandescent bulb illumination. Forward voltage at $i = 0$ nA is typically in the range of 0.3 V to 0.4 V.

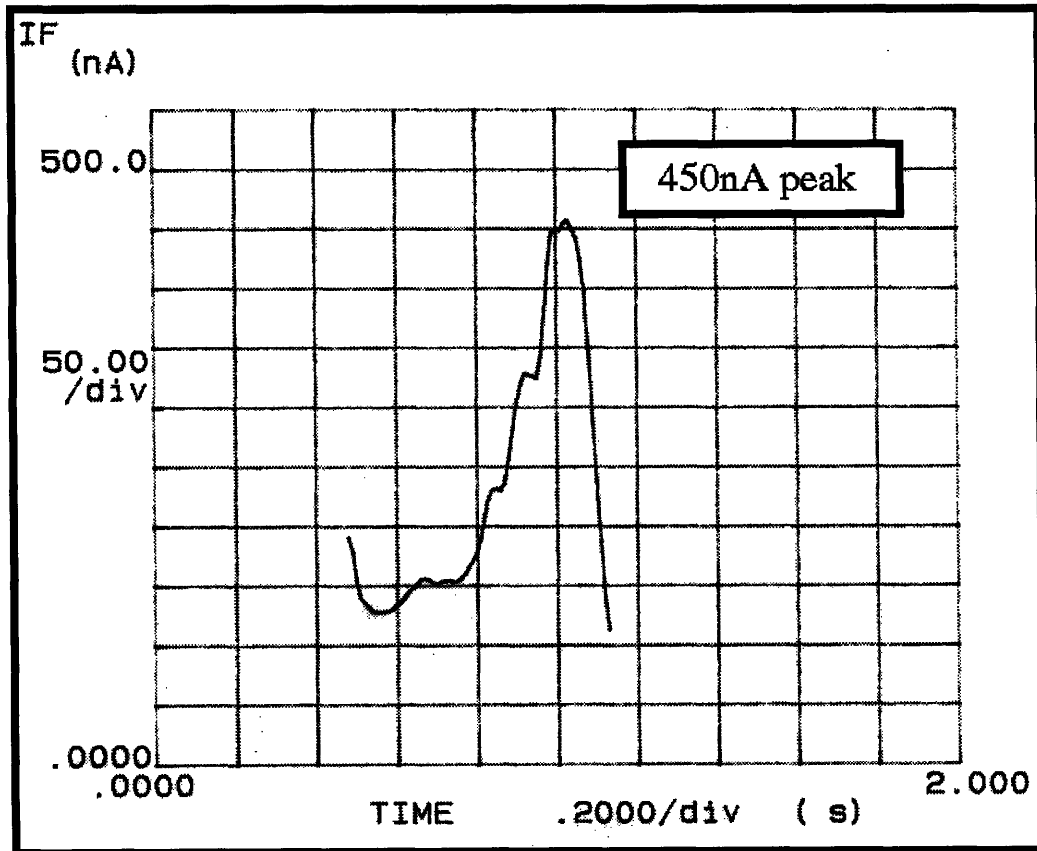

Figure 4.3: Photocurrent at zero bias for sensor illuminated with HeNe laser. The time scale shows the laser sweeping over the photodiode sensor. The photocurrent peak is approximately 450 nA yielding a quantum efficiency of 65%.

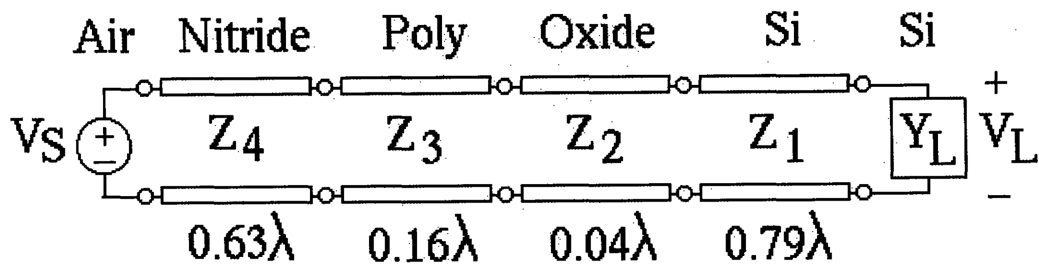

Figure 4.4: Equivalent circuit for the four layer dielectric film to the photosensitive junction.

4.2.3 Ideality Factor

The ideality factor n of the pn-junction is determined experimentally from the forward biased $i - v$ characteristic shown in Figure 4.5. The diode current is given by the diode equation [30]

$$i = I_s \left(e^{qv/nkT} - 1 \right) \tag{4.7}$$

For forward bias voltages greater than the thermal voltage $\frac{kT}{q} = 25$ mV as shown in Figure 4.5, Equation 4.7 approaches the limit

$$i \approx I_s e^{qv/nkT} \tag{4.8}$$

Taking the logarithm of Equation 4.8 an solving for n as a function of the measured slope $\log(i)/v$ yields

$$n = \frac{1}{2.303\,(kT/q)\,(\log(i_D)/v)} \tag{4.9}$$

The ideality factor is measured to be $n = 1.3$ given the slope of $\approx 10^{13}$ A/V and a thermal voltage 25 mV.

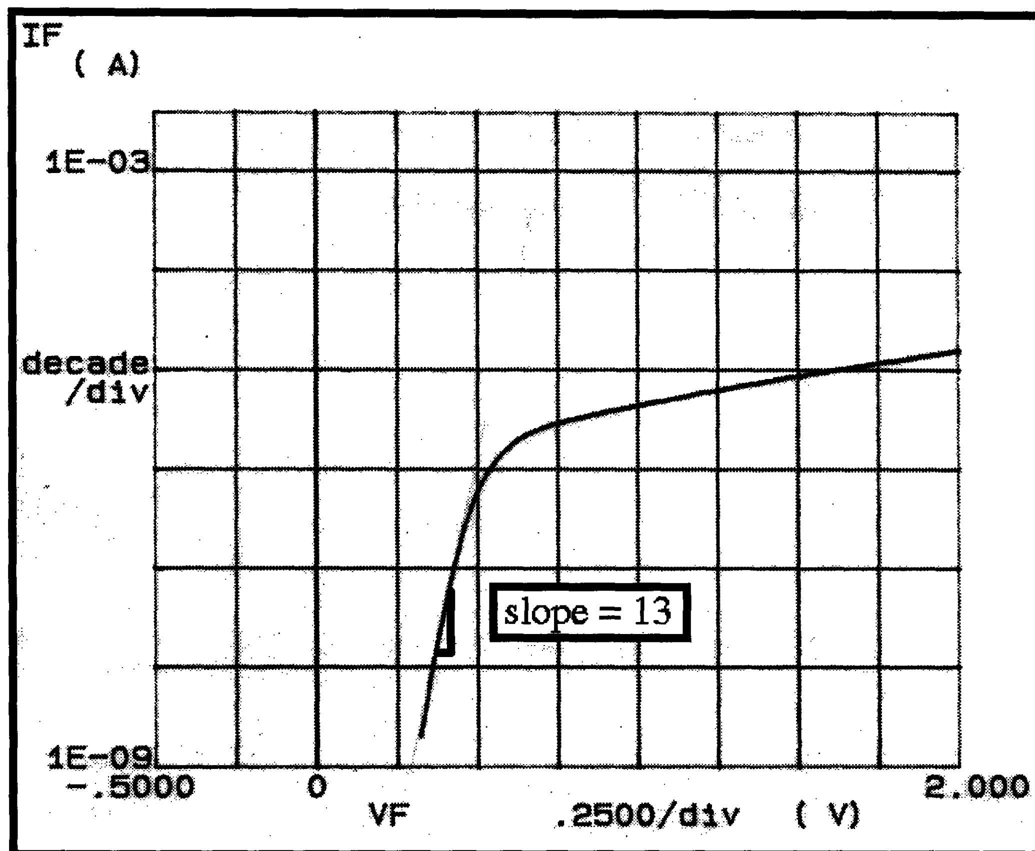

Figure 4.5: Forward biased i-v characteristic of an unilluminated pn-junction for experimental determination of ideality factor. The slope is approximately 10^{13} A/V yielding a junction ideality factor of $n = 1.3$.

4.2.4 Reverse breakdown voltage

The photodiode reverse breakdown voltage may be computed analytically and compared to the measured value. The reverse breakdown voltage is given by [30]

$$V_{br} \approx -\frac{\epsilon_{Si} E_{crit}^2}{2q} \left(\frac{N_{Ap} + N_{Dn}}{N_{Ap} N_{Dn}} \right) \tag{4.10}$$

Taking the critical breakdown field in silicon [80] to be $E_{crit} = 3 \times 10^5$V/cm, the permeability of silicon to be $\epsilon_{Si} = 11.9\ \epsilon_0$, the electronic charge to be $q = 1.6 \times 10^{-19}$ C, and the process charge densities to be $N_{Ap} = 1.7 \times 10^{16}$ cm^{-3}, and $N_{Dn} = 1.0 \times 10^{20}$ cm^{-3}, the reverse breakdown voltage is computed to be $V_{br} = -17.4$ V. This compares favorably to the measured value of -19 V as shown in Figure 4.6. The sharp negative current increase near -38 V occurs as the field region expands the diode area under the bonding pad though inversion. This is verfied by comparing the slope after the current increase which is approximately 20 mA/V to the slope before the current increase which is 0.5 mA/V. This slope change ratio is approximately 40:1, corresponding favorably to a ratio of bonding pad area to sensor area of 35:1.

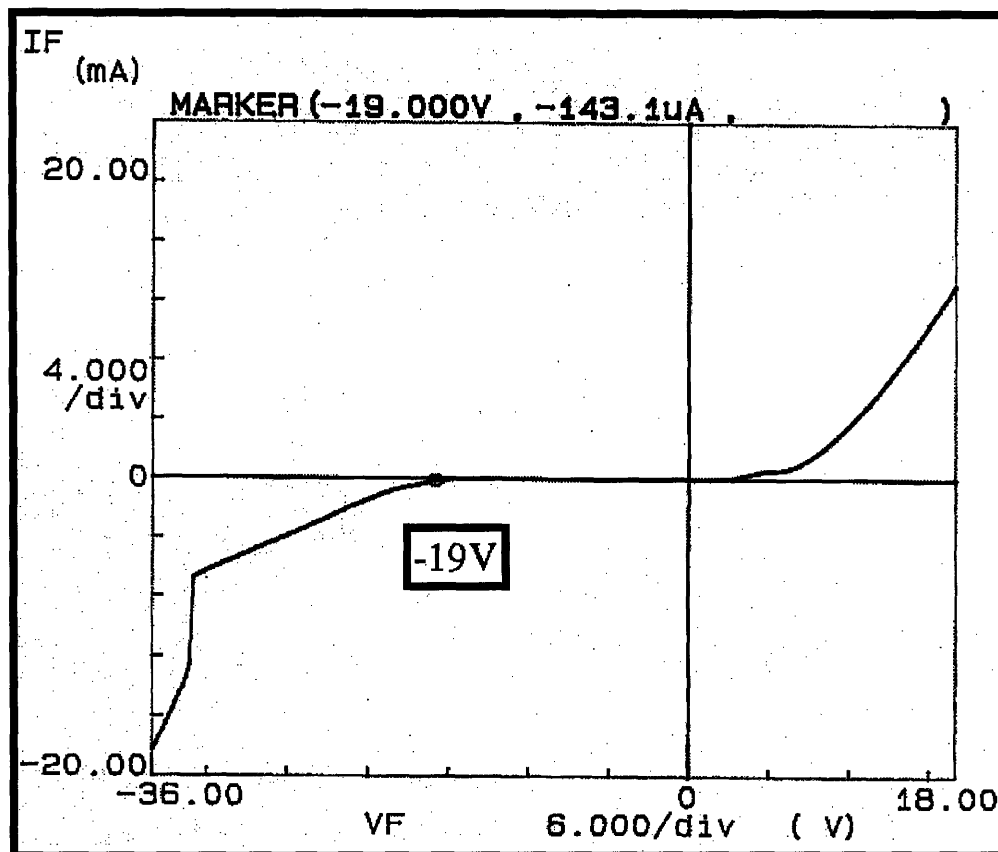

Figure 4.6: Unilluminated photodiode i-v characteristic shows the onset of reverse breakdown at approximately -19V. The sharp negative current increase near -38 V occurs as the field region expands the diode area under the bonding pad though inversion.

4.3 Time Response to a Strobed Light Source

The motion acquisition bandwidth of the photosensors is determined through a series of experiments where a triggered strobe light source is used to excite the sensor and the response is recorded in time. These experiments verify that the sensor and off-chip amplification and filter electronics bandwidth is sufficient to resolve rotor motion. A GenRad Strobotac light source with a bulb persistence of 3 μsec is configured to trigger on the positive-going edge of a 30 V pulse 500 μsec wide. Figure 4.7 shows the sensor output after amplification by the off-chip circuitry. A sensor response with time constant of 250 μsec is observed. This sensor signal is limited by the low-pass filter of the amplification circuitry which has a time constant of 250 μsec. The time constant of the low-pass filter may be modified to vary this time constant, however the low-pass filter prevents passage of higher frequency electrical noise through the amplifier circuitry. The fast initial doublet in the sensor signal is a parasitic capacitive coupling from the trigger signal to the oscilloscope probe that has not passed though the off-chip circuitry. In this set of experiments it was learned that the motion acquisition bandwidth is of sufficiently fine time resolution for the subsequent motion studies.

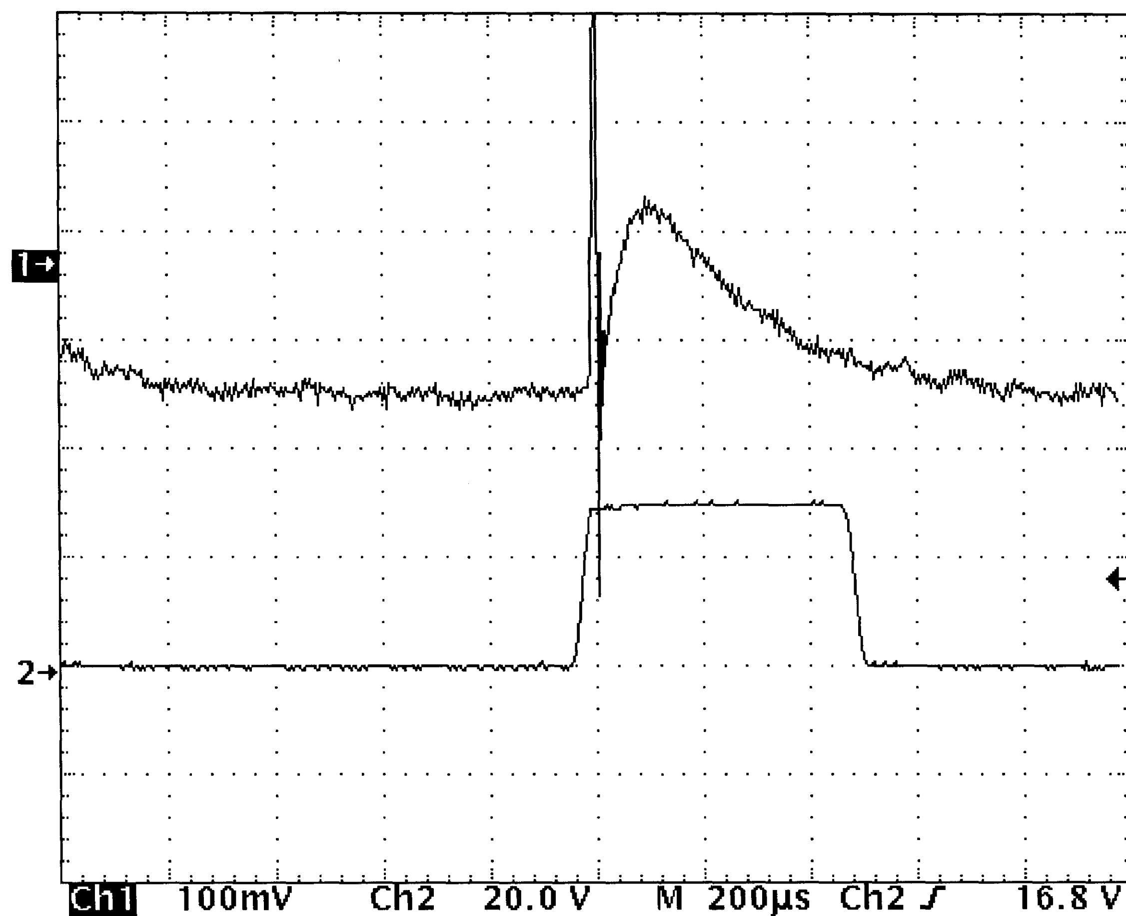

Figure 4.7: Sensor and amplification circuit response to a strobed light signal in Channel 1 at 100 mV/division. Channel 2 shows the trigger pulse used to fire the strobe at 20 V/division. The horizontal time scale is 200 μsec per division.

4.4 Static Rotor Position Measurement

The ability of three photodiode sensors to statically detect angular rotor position is experimentally verified in this section. Sensors 1, 3, and 5 shown in Figure 4.1 are probed with micromanipulators using shielded coaxial cables and run through the off-chip amplification and low-pass filter electronics. No electrical excitation is imposed at the stators. The three sensor signals are manually recorded at positions when the rotor is stationary. The true position of the rotor is measured with a protractor on the magnified (1000X) video image of the rotor. The rotor is repositioned at arbitrary angles by applying a puff from the nitrogen jet and the process is repeated many times. Figure 4.8 shows the angular position as measured by the sensors as a function of angular position measured from the protractor-video setup. The solid line represents an ideal correlation between sensor estimate and protractor-video measurement. The three data points lying far beyond the error bounds are attributed to human measurement error and movement of the rotor between reading the video and sensor signals.

Angular error in the sensor signal is determined by taking the sensor signal noise on the order of 10 mV and passing it through the position extraction algorithm. This yields a 1.1° measurement accuracy. The protractor measurement error when reading angular displacement from the protractor-video setup is estimated to be 5° and is limited by the resolution of the rotor edge, mechanical vibration of the probe station, and the non-sinusoidal shape of sensor response as a function of angle. A small error box is shown in the middle of Figure 4.8 to illustrate these error bounds. Further error is introduced by the misalignment of the protractor center to motor center and may be seen in the data where more data points lie below the line at rotor protractor angles less than 45° and more data points lie above the line at rotor protractor angles greater than 45°. Through this set of experiments it has been shown that each sensor is individually functioning, that off-chip amplification and signal conditioning electronics are functioning, and that the position extraction algorithm is correct.

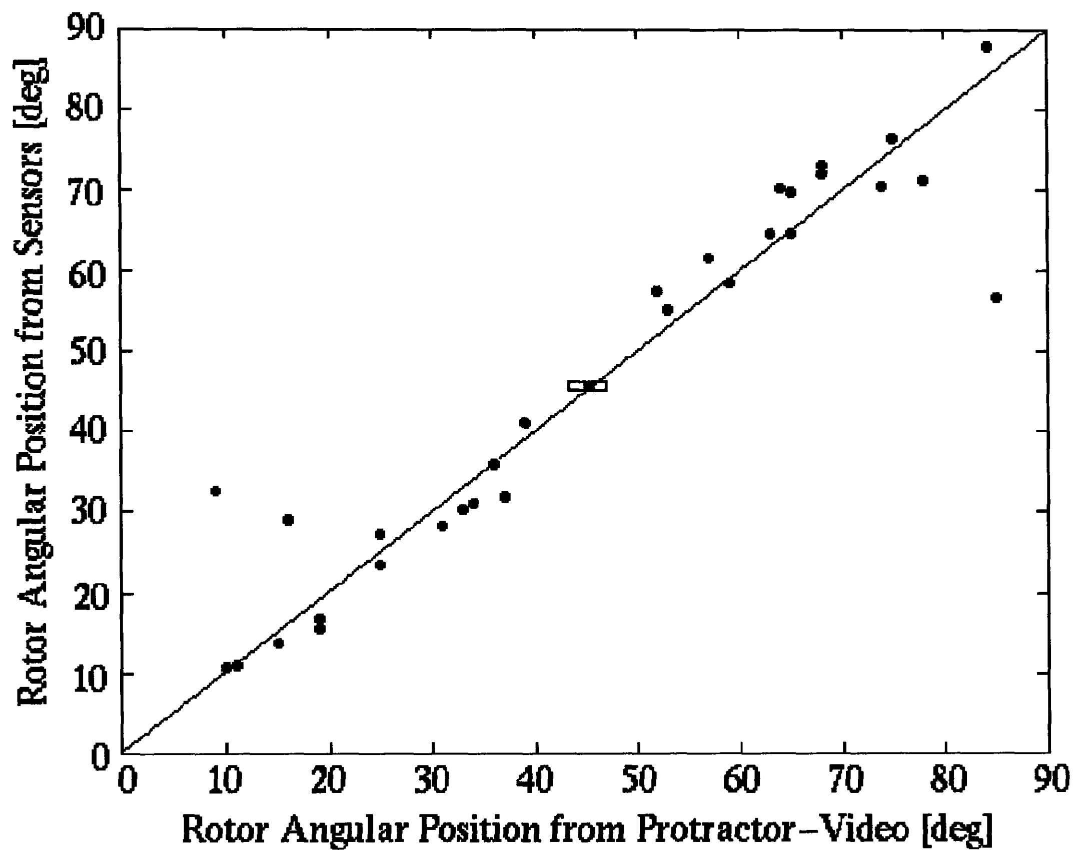

Figure 4.8: Rotor angular position as estimated by the sensors as a function of angular position recorded by the protractor-video setup. The sensor measurement error is 1.1° and the protractor-video measurement error is 5°.

4.5 Sensor Response in Presence of Stator Switching

The sensors are subject to interference from switching electric drive voltage at the stator electrodes. In these experiments positive and negative stator drive voltage is applied to A+ and A- electrodes shown in Figure 4.1, respectively. Sensor 1 as shown in Figure 4.1 is connected to the off-chip amplification and filter circuit. Two types of electrical switching interference are observed in the sensor signal when the rotor is stationary. The first type of interference, shown in Figure 4.9, is a transient above-substrate capacitive coupling between the stator drive probes and sensors. In Figure 4.9 four interference cases are shown. Channel 1 (top trace) is one sensor signal as observed through the off-chip amplification and filter circuitry. Channel 2 and Channel 3 (bottom traces) show the positive and negative 100 V drive voltages imposed at the stator electrodes. The sensor response to a bipolar drive excitation shown in Figure 4.9a is a superposition of the positive and negative excitations shown in Figures 4.9c and 4.9d. If all probes are lifted a few microns above the pads, breaking electrical contact to the pads, the measured sensor response does not change. This demonstrates that the interference is due to above substrate capacitive coupling. It is possible to cancel the positive and negative response by symmetrically balancing the positive and negative excitations in time and space. The time constants of the positive and negative responses are limited by the low-pass filter in the off-chip circuitry to approximately 250μsec as may be seen in Figure 4.9.

The second type of interference in the sensor signal is a polarity-dependent level-shift during the drive excitation. Figure 4.10 shows the level shift to be approximately 10 mV and is present only during the positive drive in Figures 4.10a and 4.10c. The level shift does not occur during the negative drive excitation. The level shift is on the order of the 10mV noise in the sensor signal as may be seen in the AC coupled 60Hz ripple in each figure. Since the level shift is small relative to the sensor signal variation during rotor motion, it affects the sensor accuracy only minimally, by introducing an additional 1.1° measurement error. The level shift persists through the entire drive pulse.

The polarity-dependent level shift is believed to be the result of a parasitic FET transistor working in conjunction with the input offset voltage of the first amplifier stage. In this scenario, two adjacent sensors, for example sensors 1 and 2 in Figure 4.1, form the source and drain of an n-channel FET. The p-type substrate region between them forms the channel. The drain of this n-channel device (sensor 2) is always tied to ground. The high voltage stator acts as the gate causing inversion in an n-channel which connects the active sensor 1 to its neighboring grounded sensor 2. The input offset voltage of the amplifier connected to sensor 1 causes a current to be injected into the sensor through the channel resistance to ground at sensor 2. A typical value of input offset voltage for the OP270 op-amp is 10 μV. Applied across a nominal channel resistance of 1000 Ω gives injected currents on the order of 10 nA. As may be seen in Figure 4.2, 10 nA is approximately 1/8 the magnitude of the full illumination 80 nA photocurrent signal and could give rise to a 10 mV level-shift at the output through the amplifier gain. In the case of a negative stator excitation, the stator is driven below the substrate voltage and the channel becomes more p-type. In this case, no current is injected and no level shift would be observed, explaining the polarity dependence of this type of interference.

These experiments have explored sensor operation in the presence of switching stator drive voltages and shown two types of electrical switching interference the sensor signal. The first interference may be removed by blanking the sensors during the transient. The second interference, a polarity-dependent level-shift coupling to the drive voltage, is ignored in the position extraction algorithm because the observed level shifts are small relative to the sensor signal variation.

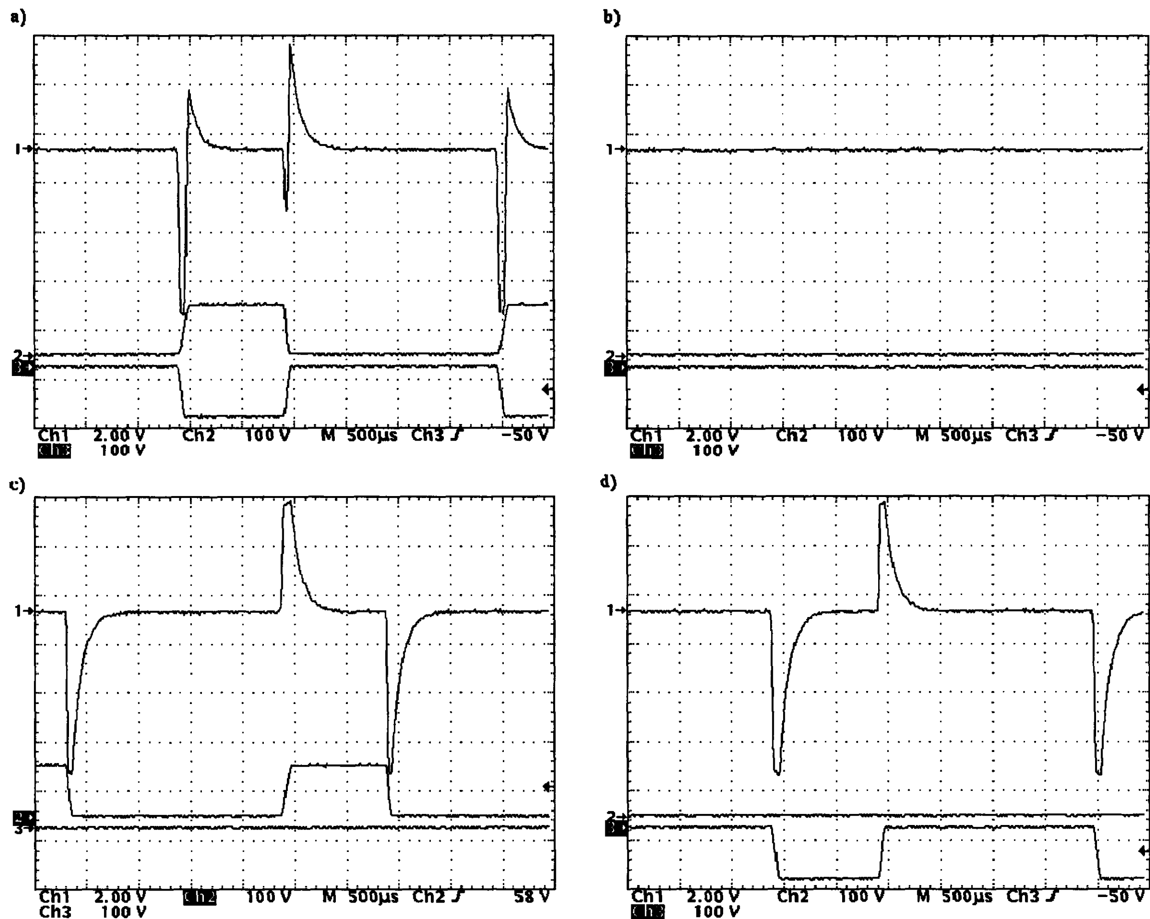

Figure 4.9: Drive interference in sensor signals where Channel 1 (top trace) is one sensor signal as observed through the off-chip amplification and filter circuitry. Channel 2 and Channel 3 (bottom traces) show the positive and negative drive voltages imposed at the stator electrodes. Plot a) is the response to bipolar excitation of 100 V, b) is the sensor response to zero excitation, c) is the response to 100 V positive excitation only, and d) response to -100V excitation only. The time constants are approximately 250 μsec in cases c) and d) and are limited by the off-chip low pass filter circuitry. There is no difference in response if all probes are lifted a few microns above their respective pads, breaking electrical contact with the pads.

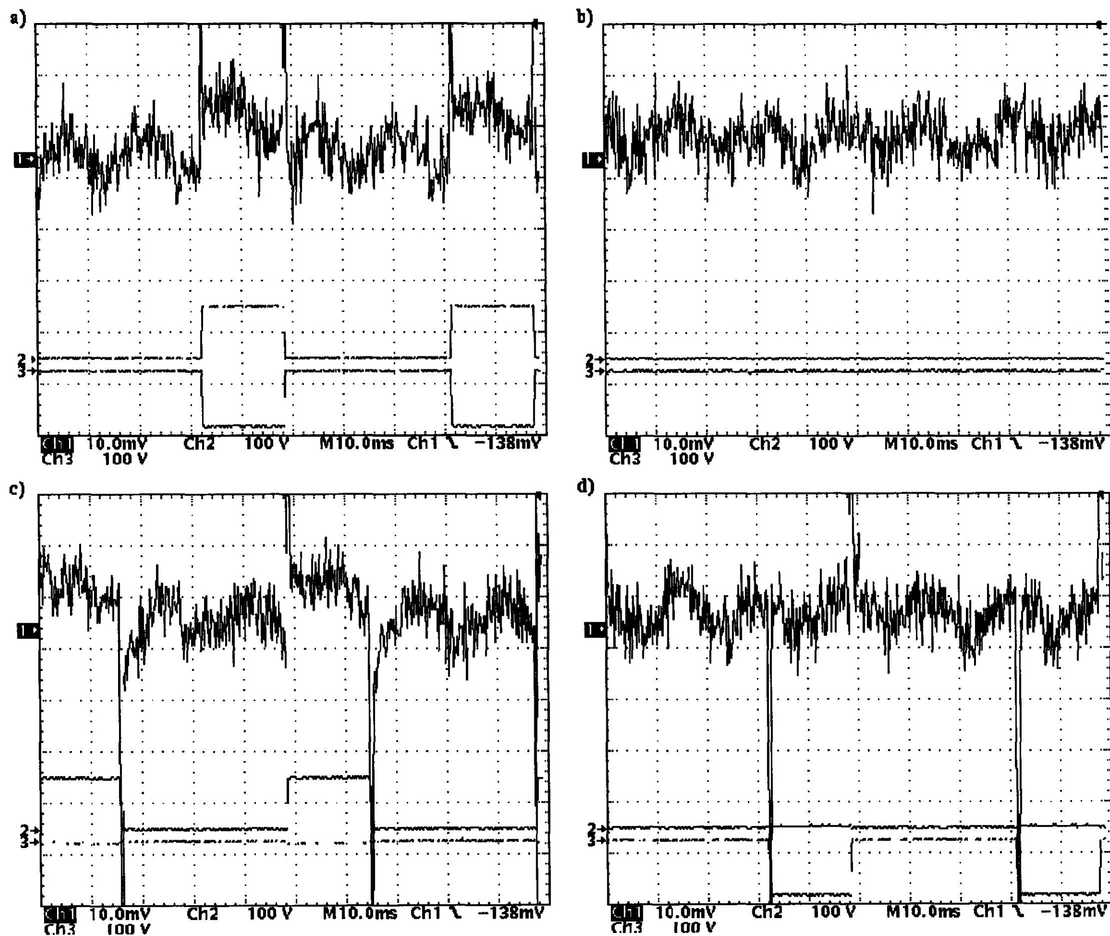

Figure 4.10: A polarity-dependent level-shift interference in the sensor signal due to the positive stator drive excitation. In this case the level shift is on the order of 10 mV and is small relative to the sensor signal variation during rotor motion. Here it introduces a 1.1° error into angle measurement. Plots show: a) sensor response for bipolar stator drive, b) sensor response with no drive excitation, c) sensor response with positive drive excitation only, and d) sensor response with negative drive excitation only.

4.6 Motion of Gas Jet Driven Rotor without Electric Drive

In this section, the sensors are used to detect rotor motion when driven by a nitrogen gas jet. No electrical stator drive excitation is imposed. Sensors 1,3, and 5 shown in Figure 4.1 are probed with micromanipulators and passed through the off-chip amplification and filter circuitry, all stator electrodes are grounded. The incandescent microscope light is powered with a DC source to remove the 120 Hz intensity ripple present under AC illumination, providing a constant illumination over the entire motor. A pipette tip attached to a nitrogen gas source is mounted on a micromanipulator and positioned to inject a stream of gas across the rotor, causing it to spin. Raw data from the three sensors are recorded over a segment of time using the TDS540.

Data from the three sensors under a rotor spinning through a counter clockwise angular sweep of approximately 3π radians (540°) at uniform velocity of 9000 rpm is shown in Figure 4.11. Channels 1-3 represent three sensor signals after off-chip amplification and filtering. Channel 4 is connected to the A+ drive phase showing no electrical excitation. As each rotor blade passes over a given photosensor, the photocurrent magnitude increases in the negative direction in Figure 4.11, and a trough may be observed in the data. As would be expected, over an angular sweep of approximately 3π radians (540°), each sensor signal exhibits approximately six troughs. The noise signal is approximately 10 mV and the peak-to-peak variation from rotor motion is 50 mV. The raw data is passed through the position extraction algorithm to give a single signal from each sensor of rotor position in time as shown in Figure 4.12. These types of transients have never been seen before. It may be observed that the three sensor signals track each other closely, giving confidence in the consistency of the data set. The best indication of rotor position is obtained by averaging the three position signals as shown in Figure 4.13. The 10 mV noise on each sensor signal represents a 1.1° measurement error in the sensor signal.

A second, different motor, is spun under nitrogen jet and the rotor motion of the three averaged sensor signals in shown in Figure 4.14. This rotor accelerates to

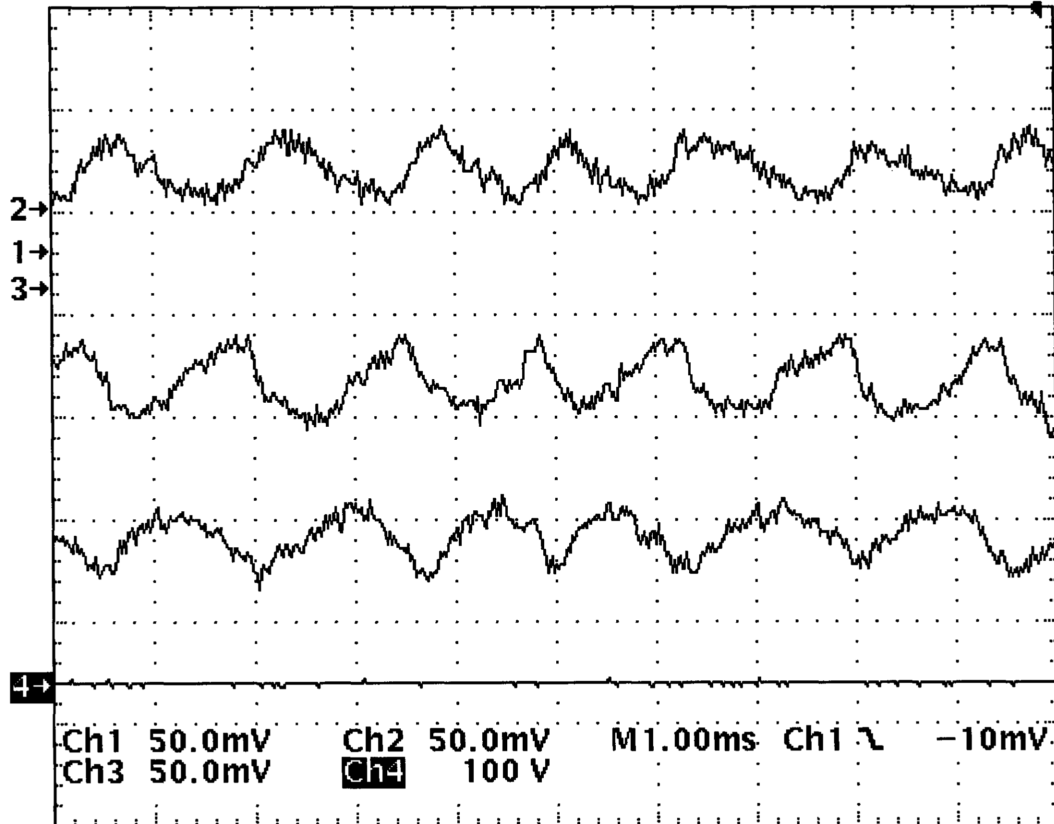

Figure 4.11: Typical raw data set where channels 1-3 represent three sensor signals from the nitrogen jet driven rotor after off-chip amplification and filtering. Channel 4 is connected to the A+ drive phase showing no electrical excitation.

rotational velocities as high as 15000 rpm within 1 ms. A repeating sticking effect occurs every $\pi/2$ rad (90°) corresponding to the passing of each rotor blade. When the motor sticks it decelerates to a velocity of 0 rpm. As the blade passes, the motor accelerates back to 15000 rpm within 1 ms. This type of detailed sticking behavior has never been seen before in a micromotor.

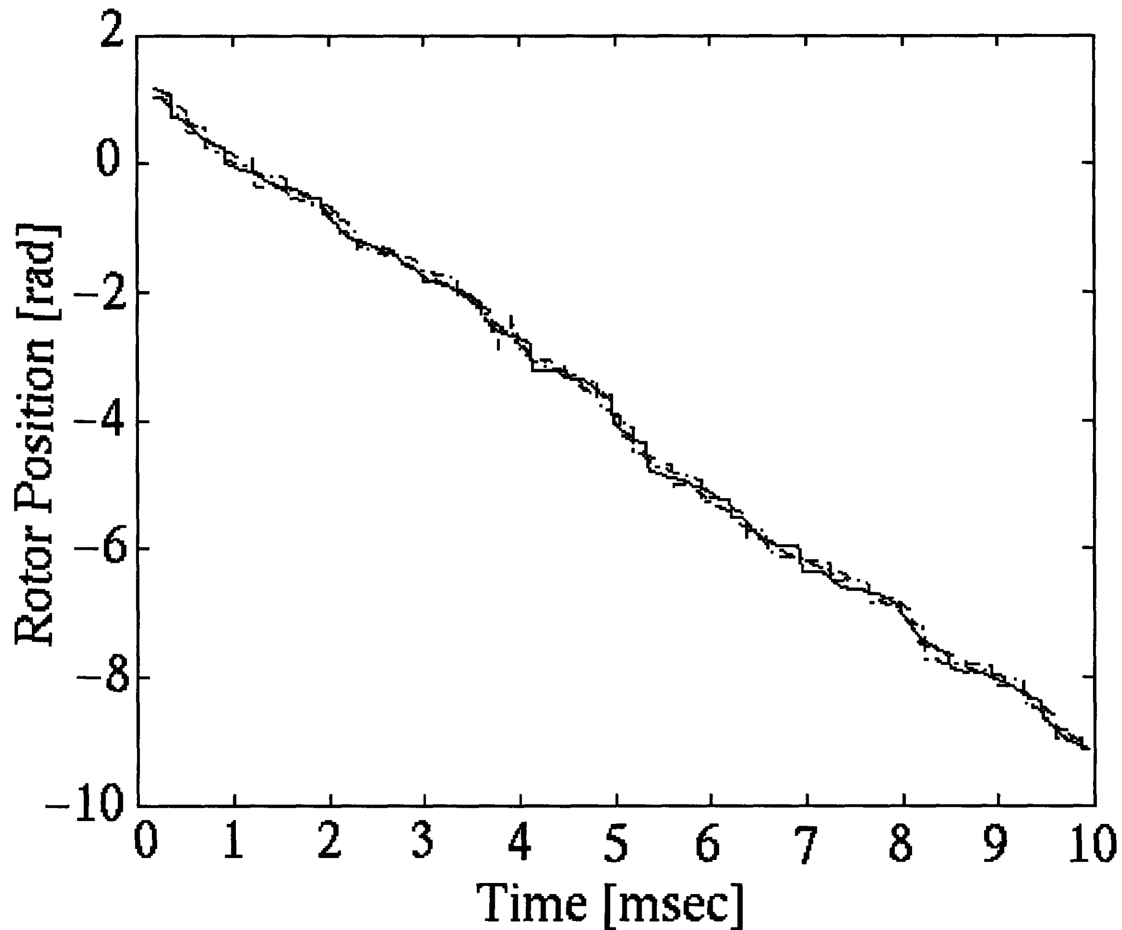

Figure 4.12: Rotor motion in time from a nitrogen gas jet driven rotor given by the position extraction algorithm. The three curves correspond to the position derived from each sensor signal. This motor spins through a counter clockwise angular sweep of approximately 3π radians (540°) at a uniform velocity of 9000 rpm. The angular position error is 1.1°.

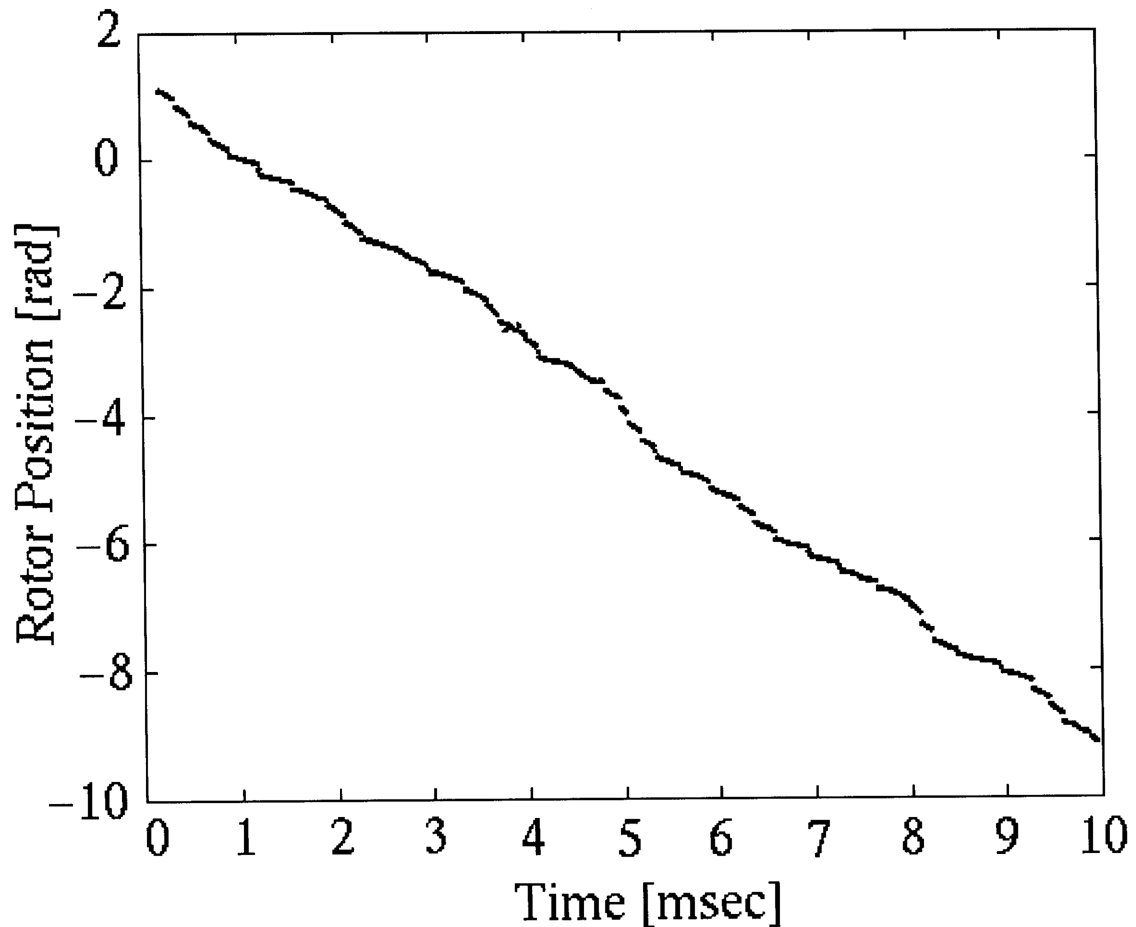

Figure 4.13: Rotor motion in time from a nitrogen gas jet driven rotor given by the position extraction algorithm. This curve is the best estimate of rotor position given by the equally weighted average of three position estimates derived from each sensor signal. This motor spins through a counter clockwise angular sweep of approximately 3π radians (540°) at uniform velocity of 9000 rpm. The angular position error is 1.1°.

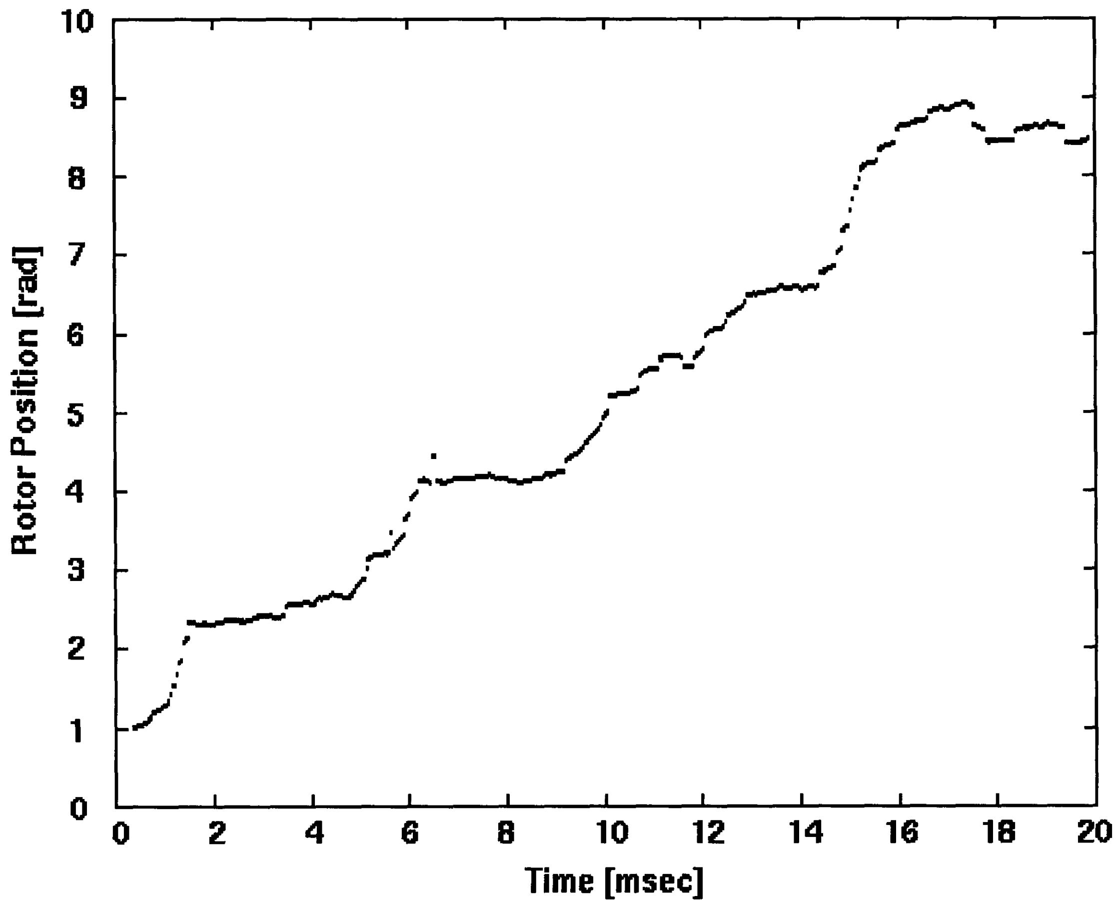

Figure 4.14: Rotor motion in time from a nitrogen gas jet driven rotor given by the position extraction algorithm. This rotor accelerates to rotational velocities as high as 15000 rpm within 1 ms. A repeating sticking effect occurs every $\pi/2$ rad (90°) corresponding to the passing of each rotor blade.

4.7 Motion of Gas Jet Driven Rotor with Electric Drive

In these experiments, micromotors are subject to the same conditions as in the previous section with the addition of a bipolar three-phase 100V stator excitation. In these experiments the nitrogen gas jet is positioned to exert the dominant motive force on the rotor. Sensors 1, 3, and 5 as shown in Figure 4.1 are connected to the off-chip amplification and filtering circuitry. All stators are connected to a three phase (A, B, and C) bipolar excitation where first A+ and A- are on, and B+, B-, C+, and C- are off. Next B+ and B- are on, and A+, A-, C+, and C- are off. Next C+ and C- are on, and A+, A-, B+, and B- are off. The cycle then repeats itself. The sensor and stator shield are grounded. Figure 4.15 shows data recorded from the three sensors after the off-chip amplification and filtering circuitry. The bottom channel, channel 4, shows the C- stator drive phase. Capacitive coupling interference from the stator drive is visible as vertical spikes in the data. This interference is blanked in 300 μsec windows and the data is linearly interpolated over those windows in the position extraction algorithm. In this experiment the level shift due to the positive stator excitation is not apparent. The raw data are transformed into rotor motion in time in Figure 4.16 by the position extraction algorithm. The time intervals in Figure 4.16 show which bipolar phase A, B, or C, is on during that interval. The vertical lines separating the vertical regions indicate phase voltage transitions. In this case, the motor is moving at a velocity of approximately 3600 rpm, where motion is a result of the gas jet drive. The electrical excitation is set to drive the motor at the much lower frequency of 300 rpm.

Figure 4.17 shows electrical braking and clamping in the same motor where the nitrogen jet has been repositioned. During the A and B phase excitations, the rotor is clamped as a result of nitrogen jet drag forces being opposed by the drive torque of electric origin. During the C phase the nitrogen jet drag forces dominate as a result of gas flow direction or the fact that C phase was not making electrical contact to its stator pads. The motor unclamps and moves at a constant velocity of approximately 4000 rpm until the next A and B phase excitations brake and clamp it. In these

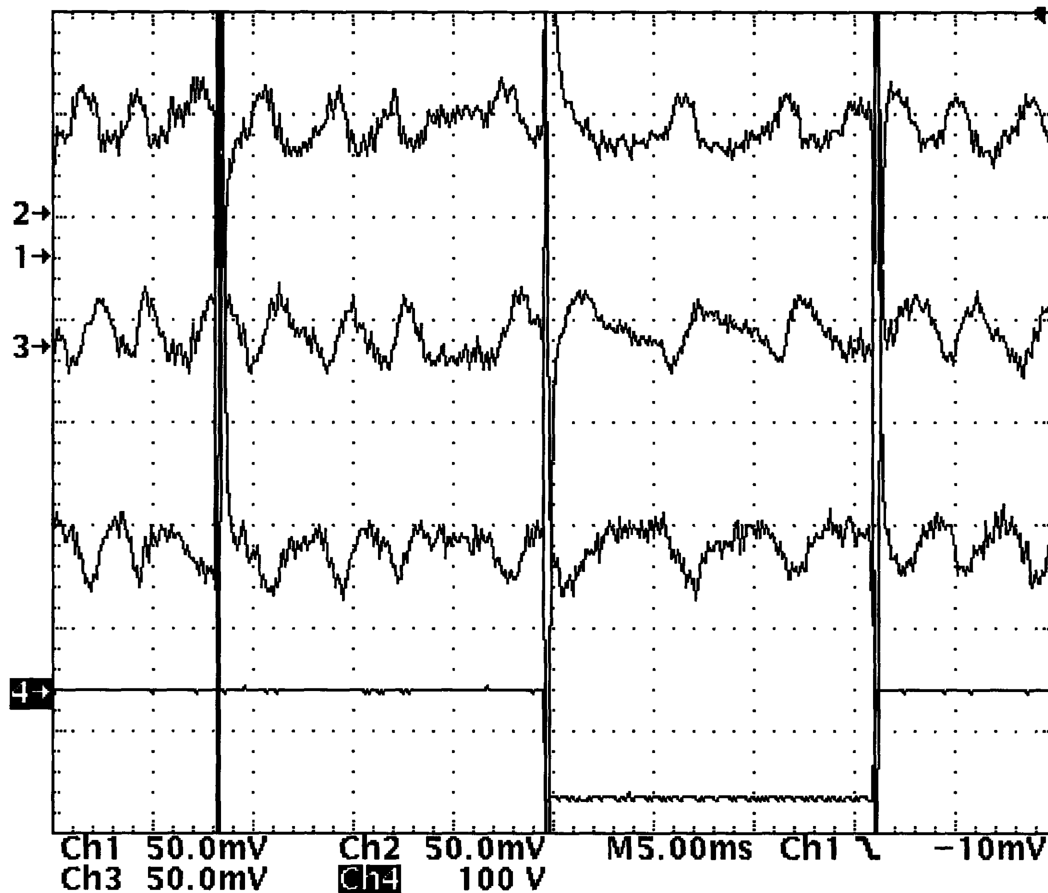

Figure 4.15: Sensor data of a gas jet driven rotor in the presence of 100 V stator electric drive. Channels 1-3 show sensor signals after the off-chip amplification and filtering circuitry. Channel 4 shows one phase of the electrical drive.

experiments it has been learned that rotor motion over each revolution is not identical as was assumed in earlier stroboscopic dynamometry studies. Rotor motion may be affected by frictional effects where motor stall times are not uniform. Electrical excitation at the stator may be used to modify the motion of a rotor spinning by nitrogen gas jet. These results show that the integrated motion sensors are able to function in the presence of electrical drive excitation and observe continuous detailed motion as the rotor spins.

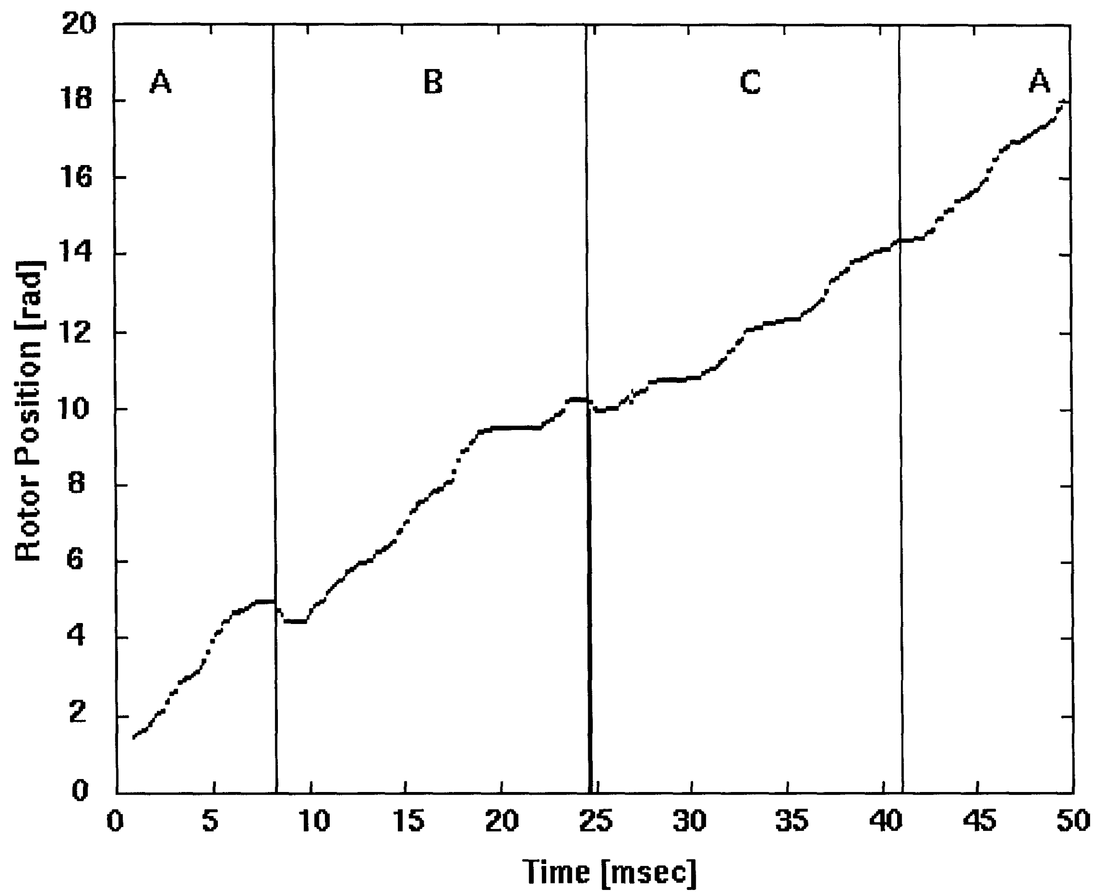

Figure 4.16: Motion of a gas jet driven rotor in the presence of 100 V stator electric drive where gas jet motive forces dominate electric drive forces.

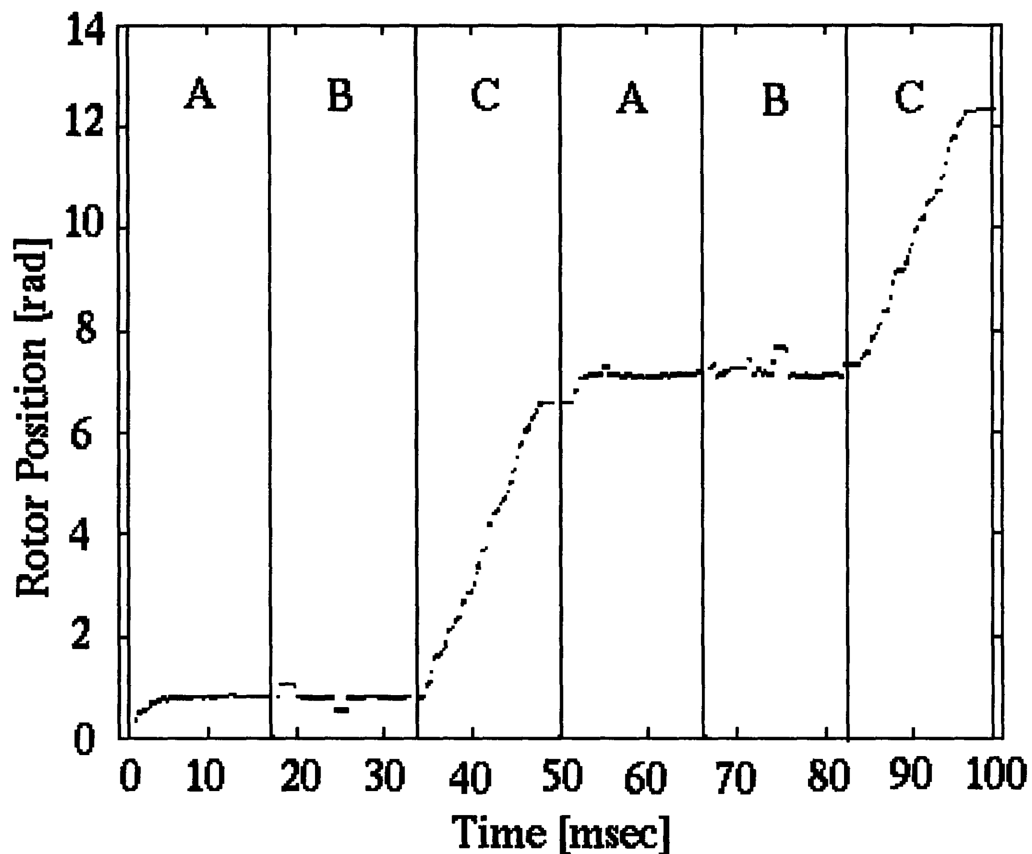

Figure 4.17: Braking and clamping by electric forces in a gas jet driven rotor in the presence of 100 V electric drive. During phase A and B the rotor is clamped and during the C phase it spins freely at a velocity of 4000 rpm.

4.8 Motion of an Electrically Driven Rotor

In this section motion sensors measure the motion of a rotor moving by the dominant torque of electric origin. Nitrogen gas jet levitation is still employed. The experimental set-up is the same as in the previous section, however the nitrogen gas jet is carefully positioned so as to only levitate the rotor and not to rotate it. The three-phase bipolar excitation is applied and sensor probes are connected at sensors 1, 3, and 5 as shown in Figure 4.1. During these experiments, the C+ electrical excitation probe was not making electrical contact to its pad, resulting in a loss of electric motive torque during the C drive phase. Figure 4.18 shows an electrical excitation which moves the rotor in a binary back-and-forth shuttering mode. When the A phase is excited the rotor rotates by $\pi/6$ rad (30°) and returns to its original position when the B phase is excited. The motion repeats over every three phase cycle. The loss of electric motive drive during the C phase is apparent as only a small rotor motion due to the C- voltage (C+ was zero). Rotor motion is a stepping transient that occurs over a time period less than 4 msec accelerating the rotor to a velocities greater than 1200 rpm during the drive motion.

Figures 4.19 and 4.20 show forward and reverse electrical stepping motion in a nitrogen gas jet levitated motor. Excitation was not present at the C+ stator contact and a loss in electric motive drive torque may be observed. During each A and B phase transition the rotor moves $\pi/6$ rad (30°) resulting in mechanical motion averaging 200 rpm. If the C phase had been active, motion would be the same as the electrical drive frequency of 300 rpm. Peak velocities during the step transient reach 1200 rpm.

It has been learned from these experiments that rotor motion in an electrically excited micromotor may be observed by integrated photodiode sensors. In these gas levitated motors, acceleration from 0 rpm to 1200 rpm was observed in time periods as short as 1 ms. At these velocities, rotor motion is a stepping motion where the rotor accelerates to its next position and is fixed at that location until the next phase is excited. An average rotational velocity may be determined and is in agreement with the electrical frequency of excitation. The details of continuous rotor motion

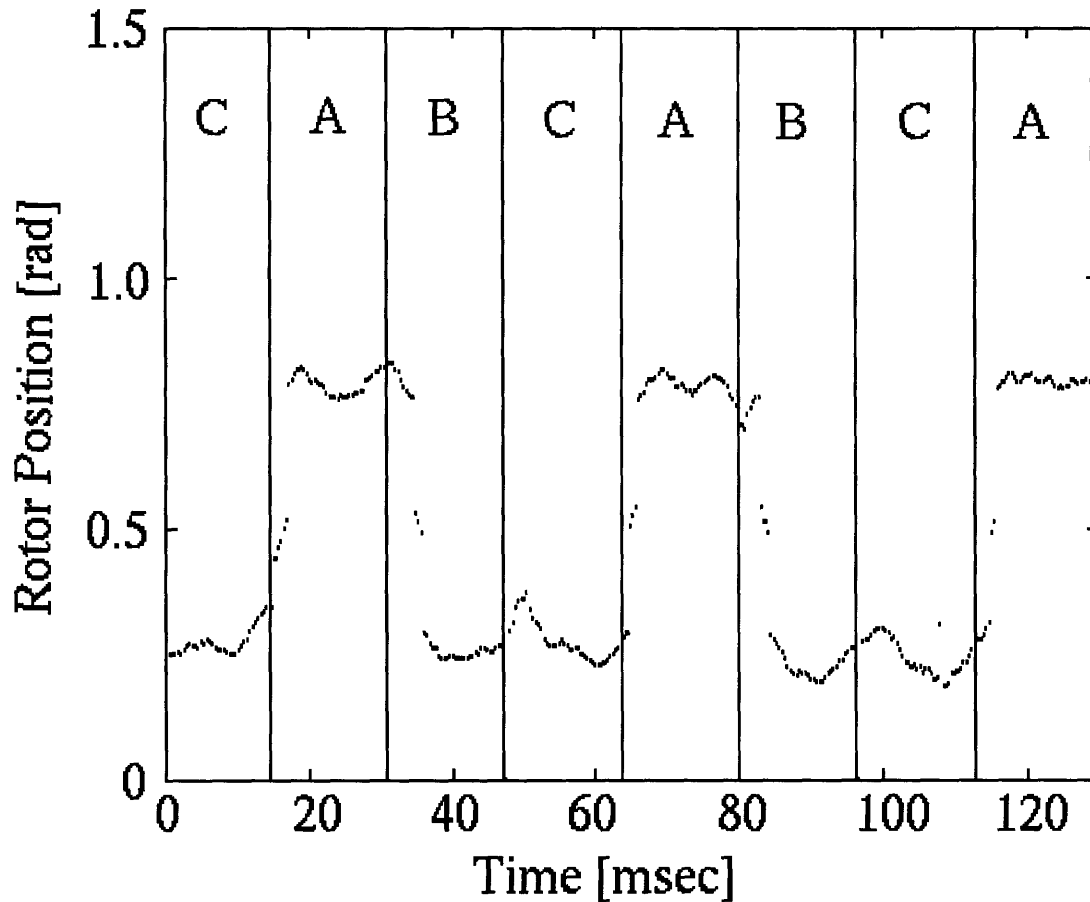

Figure 4.18: Rotor motion due to electrical excitation moving the rotor in a binary back-and-forth shuttering mode. When the A phase is excited the rotor rotates by $\pi/6$ rad (30°) and returns to its original position when the B phase is excited. Lack of drive at the C+ stator is observed as only a small perturbation in rotor position during the C drive phase. The motion repeats over every three phase cycle.

are observed over every revolution of the motor. Here sticking effects and slight rotor perturbation to unipolar phase drives are observed. It has also been learned that other excitation modes beyond simple forward stepping rotor motion are possible, including the rotor breaking/clamping and binary shutter excitation modes.

The electrical excitation of rotating micromotors without the use of gas jet levitation was not achieved in motors with functioning optical photodiodes. In order to explain why, the following analysis estimates the frictional torque present in one

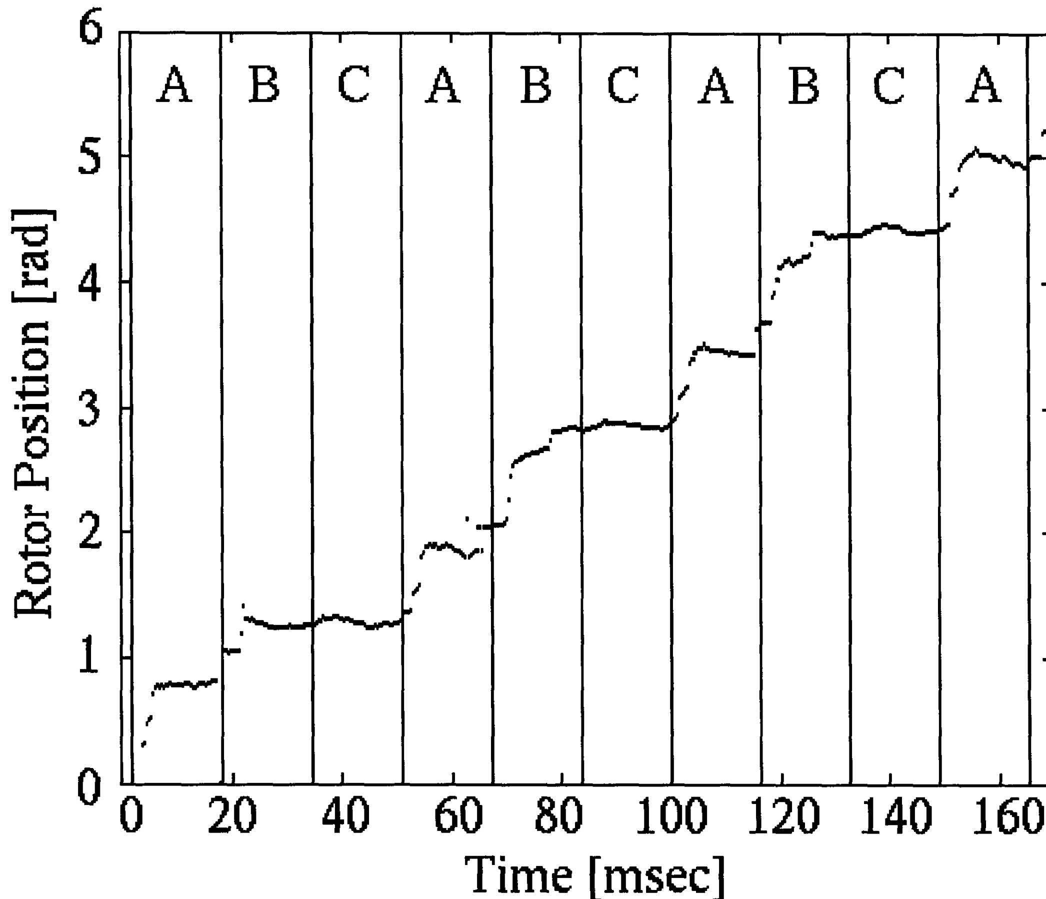

Figure 4.19: Forward electrical stepping motion in a nitrogen gas jet levitated motor. Excitation was not present at the C+ stator. During each A and B phase transition the rotor moves $\pi/6$ rad (30°) resulting in mechanical motion averaging 200 rpm. The peak transient velocity is 1200 rpm.

micromotor based on the data in Figure 4.19. From this analysis, it is concluded that the friction torque is quite large even with gas jet levitation. As a consequence, it is reasonable to expect that without the gas jet levitation, excessive stiction would prevent the micromotor from rotating under the influence of electrical excitation.

To begin the analysis, compute the time average torque of electric origin $< \tau_e >_t$ acting on the rotor. Using the approximate parallel plate model from [4],

$$< \tau_e >_t = \frac{\epsilon_o M R_o d V_{gap}^2}{2G} \left[1 - \frac{N M \lambda}{2\pi R_o} \right] \tag{4.11}$$

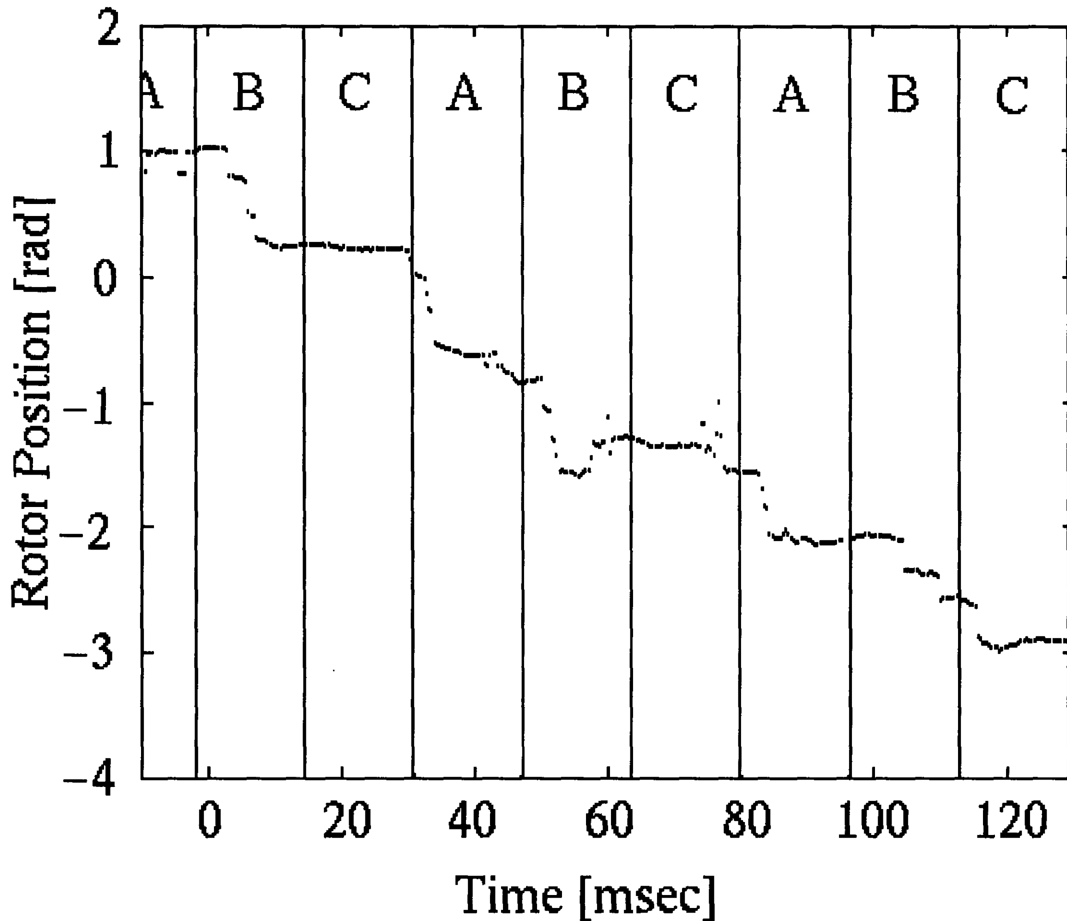

Figure 4.20: Reverse electrical stepping motion in a nitrogen gas jet levitated motor. Excitation was not present at the C+ stator. During each A and B phase transition the rotor moves $\pi/6$ rad (30°) resulting in mechanical motion averaging 200 rpm. The peak transient velocity is 1200 rpm.

where the pole face thickness is $d = 2.5$ μm, the rotor pole outer radius is $R_o = 50$ μm, the gap is $G = 1.5$ μm, the voltage is $V_{gap} = 100$ V, the minumum feature size is $\lambda = 1.0$ μm, the number of stator electrodes is $N = 6$, the number of rotor poles is $M = 4$, and the permittivity of free space is ϵ_o. In this case, the parallel plate approximation of the torque of electric origin is $< \tau_e >_t = 13$ pNm, which is similar to torques of electric origin seen in previous motors [4].

Next consider the mechanical response of the rotor to a step in $< \tau_e >_t$ as taken from Figure 4.19. For example, near the time of 70 ms, the rotor accelerates to a

velocity of 400 rad/sec in approximately 667 μs. The average acceleration is therefore approximately 6×10^5 rad/sec^2. Given that the rotor inertia is approximately 5×10^{-20} kg/m^2, the acceleration torque is approximately 0.03 pNm, which is considerably less than the available torque of electric origin. This indicates that there is excessive friction torque at work within the micromotor, and this friction torque nearly balances the torque of electric origin. By way of comparison, the friction torque in micromotors reported elsewhere is often as little as 10% of $< \tau_e >_t$ [4, 87, 59]. In the preceding analysis, the 250 μs rise time of the sensor amplifier has been ignored. This rise time will make the rotor appear to accelerate more slowly than it actually does. However, given the slow acceleration of the rotor, the effect is small and so it is neglected here.

Given that the running friction is excessively high in the micromotors studied here, it is reasonable to expect that the static friction, or stiction, is similarly high. It is also then reasonable to expect that excessive stiction is the reason why the micromotors fail to turn under the influence of electric torque without gas jet levitation. In [59], micromotors similar to those studied here were reported to rotate without levitation at voltages as low as 71 V, which is a $\sqrt{2}$-fold reduction from the 100 V used here. Since torque varies quadratically with voltage, the stiction observed there was approximately a factor of two below the electric torque applied here. An increase of stiction by a factor of two here, which would in turn prevent rotation without gas jet levitation, is certainly possible given the order of magnitude rise in running torque observed above.

While it is apparent that excess friction is at work within the micromotors studied here, the cause of this friction is still not known. Charging of the rotor [84] and rotor shield is a possible explanation for the sticking behavior observed here. Another possiblity is excessive stiction between the rotor bushing and the shield beneath it. Both would be countered by the gas jet.

Chapter 5

Summary, Conclusions, and Future Work

In this chapter the contents of the thesis are summarized. The major conclusions from the research are presented in the areas of choosing a motion sensing technique, integration of electronic photodiode devices into a micromechanical fabrication process, shielding requirements for operation of sensors in close proximity to high voltage switching actuator electrodes, improved post-processing rotor release techniques, and preliminary fabrication methods and new materials for micromotor bearings. Suggestions for future work are made for the incorporation of sensors into closed-loop micropositioning control systems and the scientific study of detailed motion and friction in micromotors.

5.1 Summary

The thesis has described the integration and operation of optical motion sensors in an electric micromotor allowing continuous real-time measurement of rotor motion for use in precision micromotion control applications and the scientific study of friction. The primary goal of the thesis was the development of an ability to extract real-time rotor motion information in an electrically driven micromotor. This goal involved integration of electronic motion sensing devices operating in close proximity to high voltage switching actuator electrodes fabricated within the confines of a micromechanical process. Secondary goals were the improvement of existing motor bearing designs, bearing fabrication techniques, bearing materials, and release processing.

Chapter 2 presented an analysis of four rotor motion sensing methods for potential use in micromotor systems, including stroboscopic dynamometry, stator $v - i$ sensing, rotor capacitive sensing, and optical sensing methods. Optical photodiode

motion sensors were chosen for implementation in the micromotor fabrication process. The performance and design requirements for the integrated optical sensors were determined and an off-chip sensing/control circuit was developed in conjunction with an algorithm to determine rotor position from the sensor signals. The off-chip sensor amplifier, filter and drive circuit shown in Figure 2.11 may be extended to allow real-time implementation of the entire position extraction algorithm for the purposes of closed-loop control.

Chapter 3 described the design and fabrication of an improved micromotor using a process that was developed to include functional electronic devices with their passivation and shielding structures. The theory of micromotor operation was reviewed and the new fabrication process was described. Improvements to the classic micromotor design were presented including choice of implant species using thermal diffusivity considerations, surface passivation, threshold voltage shift implants, electrical shielding layers, and gap plug oxide. The combination of a threshold voltage shift implant and a passivation oxide was found to be critical in the isolation of neighboring sensor regions. In an earlier process without the implants and passivation oxide the sensors were electrically shorted together and did not operate individually. The polysilicon sensor shield layer and the stator implant shields allowed sensors to function in the presence of the high voltage switching stators. These two shields are important process improvements. A new type of bearing, the flange-collar pin bearing, was designed and fabricated. The flange-collar pin bearing did not offer significant performance improvements over the standard pin bearings. New materials were used in the micromotor bearing. Gold and selective tungsten bearings were built, but require further process development before they can be used in operating motors.

Chapter 4 described experimental testing of micromotors fabricated with integrated photodiode motion sensors. The experiments were partitioned into five sets. The first set of experiments established that the photodiode sensors were sensitive to light variations and characterized their operating parameters. Zero-bias photocurrents from 0 nA to 80 nA were observed under DC incandescent bulb illumination.

A quantum efficiency of 65% was computed from calibrated laser experiments. The photojunction ideality factor of 1.3 was measured and a reverse break-down voltage of -19 V was found to lie close to the predicted value of -17.4 V. The second set of experiments characterized the ability of a sensor to respond to rapid light variations in time. Response to 3 μsec duration strobed light pulses revealed a motion acquisition time constant of 250 μsec that is limited by the low-pass filter of the off-chip electronics. This time constant was of sufficiently fine resolution for the subsequent motion studies.

In the third set of experiments, the functionality of the sensors working as a group to detect the static position of the rotor was determined. Sensor noise on the order of 10 mV allowed a 1.1° angular sensor resolution. This set of experiments verified that each sensor was individually functioning, that off-chip amplification and signal conditioning electronics were functioning, and that the position extraction algorithm was correct. The fourth set of experiments explored sensor operation in the presence of switching stator drive voltages. Two types of electrical switching interference were observed in the sensor signal. The first interference was a 250 μsec transient above-substrate capacitive coupling between the stator drive probes and sensors limited by the off-chip low-pass filter. Sensor signals were blanked during this interference. The second interference was a polarity-dependent level-shift coupling to the drive voltage explained by parasitic FET transistor action in the device coupled with the input-offset voltage of the first amplifier stage. The second type of interference was found to be small therefore was ignored by the position extraction algorithm. The final set of experiments measured, for the first time, rotor motion as driven by a gas jet and electrical excitation. A rotor driven by gas jet was observed to sweep through 3π radians at a uniform velocity of 9000 rpm. Another motor accelerated to velocities as high as 15000 rpm within 1 ms. Repeating rotor sticking effects were observed over a continuous revolution in the motor. Several cases of electrical excitation were presented including electrical rotor clamping/braking, binary shutter excitation, and

forward stepping motion of a gas levitated motor. Forward and reverse rotor stepping velocities of 300 rpm were consistent with the frequency of stator electrical excitation

Appendix A detailed the micromotor fabrication process with integrated photodiode sensors. A formal process traveler was listed with standard baseline and non-baseline operation sets used in the MIT Integrated Circuits Laboratory. The photolithography technique, wet and dry etch processing were described. Diffusion, oxidation, and deposition recipes were given. Appendix B gave a typical SUPREM-III input file for thermal implant diffusion studies and threshold voltage studies. Appendix C derived a useful capacitance matrix formulation for the output of the electrostatic solver FASTCAP. Appendix D listed the source code SENSOR.C for the position data extraction algorithm used to interpret the raw data of three sensor signals to give rotor position in time and the source code POSTCAP.C for the formulation derived in Appendix D.

5.2 Conclusions

The primary conclusion of the thesis is the experimental demonstration of the extraction of continuous real-time rotor motion data in a gas-jet or electrically excited micromotors. Continuous rotor motion in electrically excited micromotors was observed for the first time. The challenging problem of optically sensing the shadow of a moving rotor in close proximity to high voltage actuating stator electrodes was solved through the use of the appropriate implant species, threshold shifts, passivation layers, electrical shielding, off-chip filtering and interference signal blanking. Several secondary conclusions were drawn in the course of the thesis concerning the fabrication of a new bearings design, the use of new bearing materials and deposition techniques, an improved release recipe, and the use of a gap plug oxide to improve motor yield. These are discussed below.

Chapter 1 concluded that a need exists in the rapidly growing area of micromotors for accurate motion sensors with the ability to continuously sense rotor motion and enable closed-loop control. Chapter 2 concluded from an analysis of four rotor

motion sensing techniques that optical photodiode sensors were the best candidates for implementation of motion sensors given the parameters set of the micromotor and operating environment. Fabrication was simpler requiring only electronic diodes, as opposed to transistor buffers. The off-chip signal amplification and conditioning circuitry was simpler than more involved circuitry necessary to measure small capacitance variations in the presence of large parasitic capacitances. It was concluded that the off-chip sensor amplifier, filter and drive circuit may be extended to allow real-time implementation of the entire position extraction algorithm for the purposes of closed-loop control.

Chapter 3 provided several conclusions concerning the design and fabrication of an improved micromotor for a process including functional electronic devices. It was concluded that arsenic is a better implant species than phosphorus because thermal cycling during the construction of the mechanical structure effects the electronics through thermal diffusion. In the micromotor, phosphorus sensor implants would have rendered sensors inoperable as sensor regions diffused into one another and the photosensitive pn-junction diffuses beyond the depth of light penetration at the silicon surface. It was concluded that in micromechanical processes with underlying implant electronics it is desirable to minimize high-temperature cycling and implant species with low thermal diffusivity should be used. It was concluded that to prevent unintended inversion at the silicon surface which could electrically connect neighboring sensor regions, wafers receive a blanket boron ion implant to shift the threshold voltage toward deep depletion. A thermal oxide, protected from HF release etch by the silicon nitride insulator was included to assist in passivating the silicon surface.

Three electric shielding structures were employed to prevent vertical electrical clamping of the rotor and interference between the stator drive signals and the sensor signals. A rotor shield was placed in contact beneath the rotor to share charge with the rotor, reducing vertical clamping of the rotor. A grounded implant, known as the stator shield, was placed beneath the stator electrodes and interconnect to provide a return path for induced currents by the switching stator voltages. A thin transparent

grounded polysilicon layer beneath the insulator was placed everywhere except under stators and at vias to decouple vertical fields induced by the switching stators from the sensors, and to provide a discharge path for any charge accumulating at the passivation oxide - nitride insulator interface. Early sensors lots without the shielding structures resulted in sensors which did not function in the presence of switching stator voltages. It was concluded that room temperature isopropyl alcohol rinses greatly improve HF release process yields in polysilicon beam arrays. Underlying substrates of silicon nitride and polysilicon as opposed to single crystal silicon were found to have improved release yields in polysilicon beam arrays, with and without isopropyl alcohol rinses.

A new type of bearing, known as the flange-collar pin bearing was to combine the advantages of both traditional pin and flange bearings, providing greater tilt stability, and bringing frictional contacts close to the bearing to minimize the retarding torque level arm. It was concluded that the flange-collar pin bearing acted similarly to standard pin bearings because of dimple protrusions which acted as bushings in the standard pin bearings. New types of bearing materials were incorporated. It is qualitatively concluded that the solid silicon-rich silicon nitride bearings have superior yield, and thus were used in all the motion studies. Experimental gold bearings were demonstrated with a lift-off process that can be used to fabricate bearings from different types of materials not available in the clean room. Experimental CVD selective tungsten bearings were fabricated with the goal of removing the bearing pattern and etch process steps. Fabrication difficulty in getting sufficient selective growth only at the bearing prevented their use in working motors.

Chapter 4 concludes through a series of experiments, the primary thesis that rotor motion in an electrically excited micromotor may be observed by integrated photodiode sensors. In gas levitated rotors, acceleration from 0 rpm to 15000 rpm has been observed in time periods as short as 1 ms. At these velocities, rotor motion is a stepping motion where the rotor accelerates to its next position and is fixed at that location until the next phase is excited. An average rotational velocity may be

determined and is in agreement with the electrical frequency of excitation. The details of continuous rotor motion are observed over every revolution of the motor. Here sticking effects and slight rotor perturbation to unipolar phase drive are observed. It has also been learned that other excitation modes beyond simple forward stepping rotor motion are possible, including the rotor breaking/clamping and binary shutter excitation modes.

5.3 Suggestions for Future Work

The results of this thesis open several directions for future research. One major direction is the use of micromotion sensors for stabilization and precision motion control of a micromotor in a closed-loop system. Photodiodes may be optimized for increased sensitivity and hence increased angular rotor measurement resolution. The off-chip read out circuitry could be made more noise-immune with faster time constants to measure the motion dynamics at electrical transitions. Suggestions for new materials to be incorporated into coatings and structural components in the motor are given. The HF release step and underlying material effects on release yield could be further investigated.

Photodiode sensitivity could be improved by placing an undoped layer between the p and n type sides of the junction, forming a p-i-n diode. A wider, uniform electric field forms across the undoped intrinsic region of the diode, absorbing a larger fraction of light and sweeping carriers quickly across the junction by the electric field. Other regimes of diodes operation and biasing could be investigated in future work. Diodes operated at reverse bias just on the verge of avalanche breakdown might improve sensor sensitivity. Here each photon generating hole-electron pairs creates many additional pairs as a result of the avalanche process. With the addition of integrated transistor buffer stages, the integrated sensors could be used as capacitance electrodes in a rotor capacitive sensing method using circuitry developed by Leip [51].

The use of the new sensors to give vertical position information could also be explored for motor stabilization and levitation. Rotor stabilization is critical for op-

eration. To date, rotors are stabilized by mechanical contact restraint at surrounding surfaces horizontally by the bearing side-wall on the rotor, vertically by the bushing on the substrate and the rotor on the bearing cap. The availability of rotor motion sensors would allow development of new stabilization mechanisms including active differential excitation of the stators and aerodynamic control of the rotor to take advantage of compression and lift forces in its viscous fluid environment. Closed-loop position sensing and control can allow differential stator excitation to re-stabilize electromechanical instabilities that arise under open-loop control.

One major difficulty with open-loop drive is that the frictional torque has been observed to result in erratic and unpredictable rotor motion including rotor sticking and stalling. Sensors could be used in conjunction with prediction and estimation algorithms to reduce these effects. Sensors could also be used to study mid-range instabilities that might be present in open-loop drive control. As in the magnetic motor driven with open-loop voltage control at a nominally constant speed, a mid-range instability may exist to disrupt the desired motion [93]. A similar instability has been predicted for electric micromotors, for example if an air bearing were to eliminate the frictional torque and allow a slight interaction in the electric sub-dynamics to destabilize the mechanical sub-dynamics [47].

The design of a closed-loop control for an electric micromotor follows directly from the closed-loop control of a conventional magnetic motor because the electromechanical dynamics of the two types of motors are identical in form. Much information on the control of conventional magnetic motors [52] exists for direct and often simpler application to electric micromotors. Since the electrical sub-dynamics of the electrical micromotor are much faster than the magnetic sub-dynamics and all voltages are externally excited, the closed-loop control may be based only on the mechanical sub-dynamics [47]. This greatly simplifies the closed-loop control design method. In a conventional magnetic motor, torque of electric origin is controlled through the use of fast inner-loop current controls, while slower outer-loop motion controls are used to control the mechanical dynamics. In the electric micromotor, the equivalent

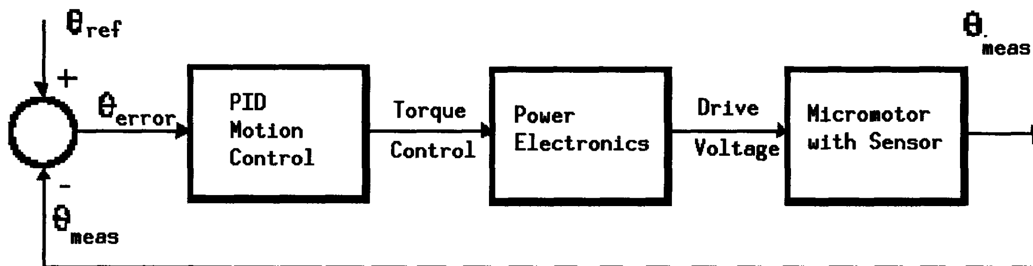

Figure 5.1: System level configuration of electric micromotor closed-loop position control.

inner-loop control charge control is not necessary because the electrical sub-dynamics are very fast. Figure 5.1 shows a possible system level configuration for closed-loop position control of an electric micromotor. A position error is computed from the difference in the desired reference position and the measured position. This error is taken as input by a PID motion controller which gives a torque command to an external power electronic voltage driver. The voltage drives the stators and causes the rotor to move to a new actual position. The sensors measure the rotor position and feed it back to compute a new error signal.

A secondary goal of the thesis has been the investigation of new bearing materials. This work could be continued in the future. Several new materials have been proposed as coatings and structural components. Coatings could be placed on the bearing, bushing, and/or bottom shield surfaces. The primary structural component to be replaced by new materials is the bearing. The rotor and shield plane may be replaced, but with high conductivity materials. Possible new materials include aluminum oxide, silicon carbide, CVD diamond, titanium, and aluminum rich silicon. The isopropyl alcohol rinse release step and release yield for different underlying substrates could

be further investigated by determining the physical mechanisms for the experimental observations.

Appendix A

Fabrication Process

This appendix details the micromotor fabrication process with integrated photodiode sensors. Further explanation of the process is given in Chapter 3. A formal process traveler is listed with standard baseline and non-baseline operation sets used in the MIT Integrated Circuits Laboratory (ICL). Additional information on the traveler format, operation sets and the baseline process may be found in Tedrow [89]. The photolithography technique is described including the resist coat and develop recipes used. Wet etch processing including buffered oxide etch, RCA clean, piranha clean, silicon-rich nitride etch, and HF release etch is described. Dry etch recipes for anisotropic and isotropic polysilicon etching and anisotropic oxide etching are given. Diffusion, oxidation, and deposition recipes are given.

A.1 Process Traveler

PROCESS TRAVELER

MICROMOTOR WITH INTEGRATED ROTOR MOTION SENSORS

LOT: ________

LOT OWNER: Eckart Jansen

Starting Material: p-type (100) wafers, 10-20 Ωcm

STEP #	STEP DESCRIPTION	STATUS	
1	Define Alignment Marks photo.set Coat recipe #11, Develop recipe #20 Mask: ALN, GCA job: ECK CWR1	Wafer numbers Opset start Opset finish	________ ________ ________
2	Plasma Etch Silicon plsilicon.set Modified recipe (isotropic polysilicon)	Wafer numbers Opset start Opset finish	________ ________ ________
3	Resist Ash ash.set	Wafer numbers Opset start Opset finish	________ ________ ________
4	Dummy Thermal Oxide dgate220.set Tube A2, Recipe #230	Wafer numbers Opset start Opset finish	________ ________ ________
5	Threshold Adjust Implant implant.set Boron, Energy = 30 keV Dose = 5×10^{12} ions/cm^2	Wafer numbers Opset start Opset finish	________ ________ ________
6	Backside Contact Implant implant.set BF_2, Energy = 30 keV Dose = 7×10^{15} ions/cm^2	Wafer numbers Opset start Opset finish	________ ________ ________
7	Define Sensors photo.set	Wafer numbers Opset start	________ ________

	Coat recipe #11, Develop recipe #20 Mask: IMP2, GCA job: ECK CWR1	Opset finish	________
8	Sensor Implant implant.set Arsenic, Energy = 90 keV Dose = 5×10^{15} ions/cm^2	Wafer numbers Opset start Opset finish	________ ________ ________
9	Resist Ash ash.set	Wafer numbers Opset start Opset finish	________ ________ ________
10	2nd Resist Clean wpiranha.set Piranha Clean	Wafer numbers Opset start Opset finish	________ ________ ________
11	Strip Dummy Oxide wet.set 7:1 BOE (doped) for 60 sec	Wafer numbers Opset start Opset finish	________ ________ ________
12	Thermal Passivation Oxide dgate220.set Tube A2, Recipe #230 70 min oxidation interval	Wafer numbers Opset start Opset finish	________ ________ ________
13	LPCVD Polysilicon Shield dpoly1.5k.set Tube A6, Recipe #423	Wafer numbers Opset start Opset finish	________ ________ ________
14	POCl Deposition dphos8.set Tube A4, Recipe #315 (90 min dope)	Wafer numbers Opset start Opset finish	________ ________ ________
15	Phosphorous Glass Wet Etch wphos2k.set 7:1 BOE (doped) for 180 sec	Wafer numbers Opset start Opset finish	________ ________ ________
16	Define 1st Polysilicon Shield photo.set Coat recipe #11, Develop recipe #20 Mask: PSHD, GCA job: ECK CWR1	Wafer numbers Opset start Opset finish	________ ________ ________
17	Plasma Etch 1st Polysilicon Shield	Wafer numbers	________

Step	Process	Record	
	plsilicon.set Modified recipe (isotropic polysilicon)	Opset start Opset finish	________ ________
18	Protective Frontside Coat phcoat.set Coat Recipe #11	Wafer numbers Opset start Opset finish	________ ________ ________
19	Backside Polysilicon Etch plsilicon.set Modified recipe (isotropic polysilicon)	Wafer numbers Opset start Opset finish	________ ________ ________
20	Resist Ash ash.set	Wafer numbers Opset start Opset finish	________ ________ ________
21	Define Passivation Oxide photo.set Coat recipe #11, Develop recipe #20 Mask: PSV, GCA job: ECK CWR1	Wafer numbers Opset start Opset finish	________ ________ ________
22	Wet Etch Passivation Oxide wet.set 7:1 BOE (doped) for 120 sec	Wafer numbers Opset start Opset finish	________ ________ ________
23	Resist Ash ash.set	Wafer numbers Opset start Opset finish	________ ________ ________
24	LPCVD Silicon-Rich Nitride Insulation dnit4k.set Tube VTR, 10:1 flow ratio	Wafer numbers Opset start Opset finish	________ ________ ________
25	LPCVD 2nd Polysilicon Shield dpoly1.5k.set Tube A6, Recipe #423	Wafer numbers Opset start Opset finish	________ ________ ________
26	POCl Deposition dphos8.set Tube A4, Recipe #315 (90 min dope)	Wafer numbers Opset start Opset finish	________ ________ ________
27	Phosphorous Glass Wet Etch wphos2k.set 7:1 BOE (doped) for 180 sec	Wafer numbers Opset start Opset finish	________ ________ ________

28	Define 2nd Polysilicon Shield photo.set Coat recipe #11, Develop recipe #20 Mask: PSHD, GCA job: ECK CWR1	Wafer numbers Opset start Opset finish	________ ________ ________
29	Plasma Etch 2nd Polysilicon Shield plsilicon.set Modified recipe (isotropic polysilicon)	Wafer numbers Opset start Opset finish	________ ________ ________
30	Protective Frontside Coat phcoat.set Coat Recipe #11	Wafer numbers Opset start Opset finish	________ ________ ________
31	Backside Polysilicon Etch plsilicon.set Modified recipe (isotropic polysilicon)	Wafer numbers Opset start Opset finish	________ ________ ________
32	Resist Ash ash.set	Wafer numbers Opset start Opset finish	________ ________ ________
33	LPCVD LTO Hard Mask dlto5k.set Tube A7, Recipe #430	Wafer numbers Opset start Opset finish	________ ________ ________
34	Define Oxide Mask for Nitride Etch photo.set Coat recipe #11, Develop recipe #20 Mask: SIN2, GCA job: ECK CWR1	Wafer numbers Opset start Opset finish	________ ________ ________
35	Wet Etch Oxide Mask wet.set 7:1 BOE (undoped) for 140 sec	Wafer numbers Opset start Opset finish	________ ________ ________
36	Resist Ash ash.set	Wafer numbers Opset start Opset finish	________ ________ ________
37	Wet Etch Silicon-Rich Nitride wnit1.5k.set Phosphoric 175 C for 130 min	Wafer numbers Opset start Opset finish	________ ________ ________

38	LPCVD Sacrificial Oxide	Wafer numbers	________
	dlto10k.set	Opset start	________
	Tube A7, Recipe #432	Opset finish	________
39	Define Bushings	Wafer numbers	________
	photo.set	Opset start	________
	Coat recipe #11, Develop recipe #20	Opset finish	________
	Mask: BUSH, GCA job: ECK CWR1		
40	Timed Wet Etch Oxide Bushing Molds	Wafer numbers	________
	wet.set	Opset start	________
	7:1 BOE (undoped) for 120 sec	Opset finish	________
41	Resist Ash	Wafer numbers	________
	ash.set	Opset start	________
		Opset finish	________
42	LPCVD Structural Polysilicon	Wafer numbers	________
	dpoly25k.set	Opset start	________
	Tube A6, Recipe #427	Opset finish	________
43	POCl Deposition	Wafer numbers	________
	dphos8.set	Opset start	________
	Tube A4, Recipe #316 (5 hr dope)	Opset finish	________
44	Phosphorous Glass Wet Etch	Wafer numbers	________
	wphos2k.set	Opset start	________
	7:1 BOE (doped) 6 min	Opset finish	________
45	Oxide Polysilicon for Hard Mask	Wafer numbers	________
	dox3k.set	Opset start	________
	Tube B5, Recipe 114 with 1:15 wet ox	Opset finish	________
46	Define Structural Polysilicon	Wafer numbers	________
	photo.set	Opset start	________
	Coat recipe #11, Develop recipe #20	Opset finish	________
	Mask: POLY, GCA job: ECK CWR1		
47	Plasma Etch Oxide Hard Mask	Wafer numbers	________
	pllto.set	Opset start	________
	Modified recipe (anisotropic oxide)	Opset finish	________
48	Resist Ash	Wafer numbers	________

Step	Description	Record	
	ash.set	Opset start	________
		Opset finish	________
49	Plasma Etch Structural Polysilicon	Wafer numbers	________
	plpoly25k.set	Opset start	________
	Modified recipe (anisotropic polysilicon)	Opset finish	________
50	Protective Frontside Coat	Wafer numbers	________
	phcoat.set	Opset start	________
	Coat Recipe #11	Opset finish	________
51	Backside Polysilicon Etch	Wafer numbers	________
	plsilicon.set	Opset start	________
	Modified recipe (isotropic polysilicon)	Opset finish	________
52	Resist Ash	Wafer numbers	________
	ash.set	Opset start	________
		Opset finish	________
53	LPCVD Gap Plug Oxide	Wafer numbers	________
	dlto10k.set	Opset start	________
	Tube A7, Recipe #432	Opset finish	________
54	Define Gap Plug	Wafer numbers	________
	photo.set	Opset start	________
	Coat recipe #11, Develop recipe #20	Opset finish	________
	Mask: PLUG, GCA job: ECK CWR1		
55	Wet Etch Gap Plug	Wafer numbers	________
	wet.set	Opset start	________
	7:1 BOE (undoped) for 330 sec	Opset finish	________
56	Resist Ash	Wafer numbers	________
	ash.set	Opset start	________
		Opset finish	________
57	LPCVD Bearing Spacer Oxide	Wafer numbers	________
	dlto5k.set	Opset start	________
	Tube A7, Recipe #430	Opset finish	________
58	Define Bearing Contact	Wafer numbers	________
	photo.set	Opset start	________
	Coat recipe #11, Develop recipe #20	Opset finish	________

	Mask: O3, GCA job: ECK CWR1		
59	Wet Etch Bearing Contact wet.set 7:1 BOE for 6 min	Wafer numbers Opset start Opset finish	________ ________ ________
60	Plasma 2nd Etch Bearing Contact pllto.set Modified recipe (anisotropic oxide)	Wafer numbers Opset start Opset finish	________ ________ ________
61	Resist Ash ash.set	Wafer numbers Opset start Opset finish	________ ________ ________
62	LPCVD Silicon-Rich Nitride Bearing dnit10k.set Tube VTR, 10:1 flow ratio	Wafer numbers Opset start Opset finish	________ ________ ________
63	LPCVD LTO Hard Mask dlto5k.set Tube A7, Recipe #430	Wafer numbers Opset start Opset finish	________ ________ ________
64	Define Oxide Mask for Nitride Etch photo.set Coat recipe #11, Develop recipe #20 Mask: P2, GCA job: ECK CWR1	Wafer numbers Opset start Opset finish	________ ________ ________
65	Wet Etch Oxide Mask wet.set 7:1 BOE (undoped) for 120 sec	Wafer numbers Opset start Opset finish	________ ________ ________
66	Resist Ash ash.set	Wafer numbers Opset start Opset finish	________ ________ ________
67	Wet Etch Silicon-Rich Nitride Bearings wnit10k.set Phosphoric acid at 175°C for 6 hr	Wafer numbers Opset start Opset finish	________ ________ ________
68	Dice Wafers diesaw.set	Wafer numbers Opset start Opset finish	________ ________ ________

69	Release Etch	Wafer numbers	________
	HF Release Etch	Opset start	________
		Opset finish	________

A.2 Photolithography

Photolithography is used to define patterns on the wafer surface using a set of 11 masks designed with the KIC CAD layout tool [10]. Completed layouts are transferred to chrome or emulsion patterns on 5 inch glass or quartz substrate using computer controlled optical shutter exposure, scanned electron beam, or direct laser writing. The optical shutter system available for use at MIT has difficulty resolving clear gaps of less than 10 μm so an external mask vendor was used [1]. These masks were produced on lime-soda glass plates using direct laser writing with precision greater than 1 μm and satisfy the micromotor tolerances.

The typical photolithography operational set involves a vapor prime in a Yield Engineering Model 3/10 automatic hexamethyldisilazane (HMDS) oven at 150°C to promote resist adhesion to the wafer surface. A GCA Model 1006 Wafertrac cassette-to-cassette with air-track transport and hot plates for resist bakes is used to coat and develop wafers. Resist is exposed in a GCA Model 4800 DSW g-line (432 nm) stepper wherein a mask pattern is optically reduced by a factor of ten and stepped in an 8 $\times$ 8 matrix of 1 cm dies on the wafer surface. Kodak 820 positive resist with OCG PBR1 Edge Bead Remover (EBR) was used on the coater and developed with KTI 934 alkali-ion-free developer that is 1:1 premixed with DI H_20. The resist coat recipe #11 shown in Table A.1 and developer recipe #20 shown in Table A.2 result in developed resist thicknesses of approximately 1.1 μm.

A.3 Wet Etches

A.3.1 7:1 Buffered Oxide Etch

Buffered Oxide Etch (BOE) is composed of HF with an NH_4F buffer to control etchant pH. The 7:1 dilution of DI H_2O with BOE was observed to etch at rates of

approximately 65 Å/sec in undensified low temperature oxide (LTO) and 20 Å/sec in thermal oxide.

A.3.2 Silicon-Rich Silicon Nitride Etch

Wafers are immersed in 175°C phosphoric acid to etch low stress silicon-rich nitride with a low temperature oxide (LTO) hard mask. Etch rates of 2500 Å/hr silicon-rich nitride and less than 100 Å/hr LTO are typical.

A.3.3 RCA Clean

The RCA clean is a standard wet chemical clean used to remove organic and ionic contaminants from wafer surfaces before high temperature processing. The ICL RCA clean consists of an organic clean, HF dip to remove native oxide, and an ionic clean. The organic clean is a 10 minute immersion in a 75°C mixture of 5:1:1 DI H_20:NH_4OH:H_2O_2. Wafers are dump rinsed in DI H_2O to a resistivity of $\rho > 12$ Ωcm. Next wafers are dipped at room temperature into 50:1 DI H_2O:HF for 15 seconds. Following the HF dip, wafers are dump rinsed to a resistivity of $\rho > 12$ Ωcm. The ionic clean is a 15 minute immersion in a 75°C mixture of 6:1:1 DI H_2O:HCl:H_2O_2. Wafers are dump rinsed to a resistivity of $\rho > 12$ Ωcm and spin dried.

A.3.4 Piranha Clean

The piranha clean is a mixture of 3:1 H_2SO_4:H_2O_2 used to clean residual resist and other organic matter from the wafer surface. This clean was used to insure removal of residual resist after high energy resist-masked ion implantations.

A.3.5 HF Release Etch

All new polypropylene and Pyrex beakers are used for each release etch to avoid contamination from residues left on the beaker walls during previous releases. In a chemical hood, motor dies are placed in a 100 ml polypropylene beaker with 20 ml of concentrated liquid HF (49 % by weight). The dies are etched for 15 minutes to insure undercut of the sacrificial oxide and full release of the rotor at the bearings. The beaker is then placed in the hood sink to rinse under flowing DI water for 5

minutes. In a Pyrex beaker, 50% (by volume) 2,2-propanol (IPA) is mixed to 20 ml. Each die is transferred to the diluted IPA without allowing the die surface to de-wet. This may be accomplished by either "pouring" the dies suspended in a small amount of water into the Pyrex beaker or by lifting the die with a drop of liquid adhering to its front-side surface. After 5 minutes of 50/50 IPA rinse, most of the IPA is poured off into a hydrocarbon waste container, again ensuring die front-surfaces do not de-wet. Another 20 ml of full concentration IPA is poured into the Pyrex beaker. After 5 minutes, the dies are removed from the Pyrex beaker and gently dried under a nitrogen jet for 1 minute.

A.4 Dry Etches

Dry plasma etches are performed in Lam Research etchers, Model 480 for polysilicon and Model 594 for oxide. These are load-locked cassette-to-cassette single-wafer etchers with parallel-plate 20 cm diameter Al electrodes. Three plasma etches for isotropic polysilicon, anisotropic polysilicon, and anisotropic oxide have been modified and are described below.

A.4.1 Isotropic Polysilicon Etch

The isotropic polysilicon plasma recipe uses SF_6-based chemistry to achieve an isotropic etch rate of approximately 6900 Å/min in LPCVD polysilicon and 2700 Å/min in photoresist. The recipe is shown in Table A.3 and is used as timed etch for creating alignment wafer marks, patterning polysilicon shield layers, and backside polysilicon removal.

A.4.2 Anisotropic Polysilicon Etch

The anisotropic polysilicon recipe uses SF_6-based chemistry and has been optimized to etch 1.5 μm wide gaps 2.5 μm wide with straight side walls. Patterned thermal oxide is used as a hard mask since a single coat of photoresist is not sufficient to mask the polysilicon during the 4 minute gap etch. Resolving the gaps in multiple resist coats would be difficult because of limited depth-of-focus during exposure. Etch

rates in LPCVD polysilicon are typically 6250 Å/min for the recipe shown in Table A.4.

A.4.3 Anisotropic Oxide Etch

The anisotropic oxide etch is CHF_3/CF_4-based shown in Table A.5 is used to pattern the thermal and LPCVD oxide hard masks and to create bearing anchors. It etches thermal oxide at a rate of approximately 24 Å/sec with photoresist mask.

A.5 Diffusion, Oxidation, and Deposition

Diffusion, oxidation, and deposition were carried out using Bruce Engineering BTU Model BDF-4 cantilever-load furnaces and a Thermco vertical thermal reactor (VTR) for silicon-rich nitride deposition. Gas flow rates are given as percentage of the maximum flow rate for each tube and are indicated in the corresponding caption in each recipe table. Two thermal oxide oxidation recipes are used, an oxidation recipe 230 (Table A.6) for 220 Å of dry oxide for passivating the silicon surface after sensor implants and a thicker oxide with recipe 114 (Table A.7) dry-wet-dry for the 3000 Å oxide hard-mask used in the anisotropic polysilicon etch.

Low temperature sacrificial oxide (LTO) is deposited using low pressure chemical vapor deposition (LPCVD) in thicknesses of 5000 Å in recipe 430 (Table A.8) and 1.0 μm in recipe 432 (Table A.9). LPCVD Polysilicon is deposited at thicknesses of 1500 Å for polysilicon shields in recipe 423 (Table A.10) and 2.5 μm for structural polysilicon in recipe 427 (Table A.11). After deposition, polysilicon is liquid-source $POCl_3$ doped at atmospheric pressure for 90 minutes in recipe 315 (Table A.12) and 5 hours in recipe 316 (Table A.13) to relieve intrinsic stress and reduce sheet resistivity into the range of 2-10 Ω/square. Low-stress silicon nitride is deposited in the VTR at a flow ratio of 10:1 of SiH_2Cl_2 to NH_3 to thicknesses of 4000 Å for the electrical insulation layer and 1.0 μm for the bearing material using the recipe in Table A.14.

Step	Description	Conditions	Time
1	Dehydration bake	200°C	1 sec
2	Resist dispense	3 ml, 0 RPM	4 sec
3	Resist spread	200 RPM/sec, 250 RPM	3 sec
4	Resist spin coat	10000 RPM/sec, 5000 RPM	20 sec
5	Decelerate	-40000 RPM/sec, 900 RPM	2 sec
6	EBR dispense	900 RPM	15 sec
7	EBR spin off	900 RPM	5 sec
8	Spin dry	40000 RPM/sec, 2000 RPM	15 sec
9	Stop	-40000 RPM/sec, 0 RPM	1 sec
10	Softbake	115°C	60 sec

Table A.1: Standard resist coat recipe #11.

Step	Description	Conditions	Time
1	Bake (no heat)	25°C	5 sec
2	DI H_2O wet	10000 RPM/sec, 500 RPM	5 sec
3	Developer spray	500 RPM	2 sec
4	Spin	-200 RPM/sec, 50 RPM	3 sec
5	Develop	0 RPM	10 sec
6	Developer spin off	10000 RPM/sec, 250 RPM	2 sec
7	Developer spray	-200 RPM/sec, 50 RPM	3 sec
8	Develop	0 RPM	30 sec
9	Developer spin off	10000 RPM/sec, 500 RPM	2 sec
10	DI H_2O rinse	800 RPM	15 sec
11	Spin dry	5000 RPM	20 sec
12	Hardbake	130°C	60 sec

Table A.2: Standard resist develop recipe #20.

Parameter	Step 1	Step 2	Step 3
Pressure (mTorr)	50	450	450
RF Power (Watts)	0	0	100
Gap Spacing (cm)	1.2	1.2	1.2
SF_6 (sccm)	0	135	135
O_2 (sccm)	0	45	45
CCl_4 (sccm)	0	0	0
He (sccm)	0	0	0
Cl_2 (sccm)	0	0	0
Time	1 min	stable	30 sec

Table A.3: Isotropic SF_6 polysilicon plasma etch recipe.

Parameter	Step 1	Step 2	Step 3
Pressure (mTorr)	50	350	350
RF Power (Watts)	0	0	100
Gap Spacing (cm)	1.0	1.0	1.0
SF_6 (sccm)	0	135	135
O_2 (sccm)	0	50	50
CCl_4 (sccm)	0	0	0
He (sccm)	0	0	0
Cl_2 (sccm)	0	0	0
Time	2 min	stable	4 min

Table A.4: Anisotropic SF_6 polysilicon plasma etch recipe.

Parameter	Step 1	Step 2	Step 3
Pressure (Torr)	2.6	2.6	2.6
RF Power (Watts)	0	0	700
Gap Spacing (cm)	0.38	0.38	0.38
CHF_3 (sccm)	0	45	45
CF_4 (sccm)	0	50	50
He (sccm)	0	120	120
N_2 (sccm)	0	0	0
O_2 (sccm)	0	0	0
Time	1 min	stable	2:45 min

Table A.5: Anisotropic CHF_3/CF_4 oxide plasma etch recipe.

Interval	Description	N_2 (%)	O_2 (%)	H_2 (%)	HCl (%)	Temp (°C)	Time (min)
0	Idle	30	0	0	0	800	0
1	Boat in	90	0	0	0	800	20
2	Stabilize	90	0	0	0	800	10
3	Ramp up	60	0	0	0	10°/min	15
4	Stabilize	60	0	0	0	950	10
5	Dry oxidize	0	60	0	0	950	41.6
6	Ramp down	60	0	0	0	-5°/min	30
7	Boat out	90	0	0	0	800	60

Table A.6: 220 Å dry thermal gate oxide recipe 230 in tube A2. Maximum flow rates for N_2 and O_2 are 10 SLM, for H_2 is 20 SLM, and for HCl is 100 sccm.

Interval	Description	N_2 (%)	O_2 (%)	H_2 (%)	HCl (%)	Temp (°C)	Time (min)
0	Idle	30	0	0	0	800	0
1	Boat in	90	0	0	0	800	20
2	Stabilize	90	0	0	0	800	10
3	Ramp up	60	0	0	0	10°/min	15
4	Stabilize	60	0	0	0	950	10
5	Dry oxidize	0	60	0	0	950	30
6	Wet oxidize	0	30	30	0	950	75
7	Dry oxidize	0	60	0	0	950	30
8	Ramp down	60	0	0	0	-5°/min	30
9	Boat out	90	0	0	0	800	50

Table A.7: 3000 Å dry-wet-dry thermal oxide recipe 114 in tube B5. Maximum flow rates for N_2 and O_2 are 10 SLM, for H_2 is 20 SLM, and for HCl is 500 sccm.

Interval	Description	N_2 (%)	O_2 (%)	SiH_4 (low) (%)	SiH_4 (coarse) (%)	Temp (°C)	Time (min)
0	Idle	30	0	0	0	430	0
1	Boat in	30	0	0	0	430	30
2	Stabilize	30	0	0	0	430	2
3	Pump and purge	30	0	0	0	430	50
4-7	Pump and purge	30	0	0	0	430	9
8	Deposit LTO	30	31	38.5	80.5	430	100
9-16	Pump and purge	30	0	0	0	430	16
17	Purge to atm	30	0	0	0	430	20
18	Boat out	30	0	0	0	430	30

Table A.8: 3000 Å LPCVD low temperature oxide (LTO) deposition recipe 430. Tube A7 is at a pressure of approximately 300 mTorr during deposition. Maximum flow rates for N_2 and O_2 are 500 sccm, for SiH_4 (low) is 100 sccm, for SiH_4 (coarse) is 1000 sccm.

Interval	Description	N_2 (%)	O_2 (%)	SiH_4 (low) (%)	SiH_4 (coarse) (%)	Temp (°C)	Time (min)
0	Idle	30	0	0	0	430	0
1	Boat in	30	0	0	0	430	30
2	Stabilize	30	0	0	0	430	2
3	Pump and purge	30	0	0	0	430	50
4-7	Pump and purge	30	0	0	0	430	9
8	Deposit LTO	30	31	38.5	80.5	430	200
9-16	Pump and purge	30	0	0	0	430	16
17	Purge to atm	30	0	0	0	430	20
18	Boat out	30	0	0	0	430	30

Table A.9: 1.0 μm LPCVD low temperature oxide (LTO) deposition recipe 432. Tube A7 is at a pressure of approximately 300 mTorr during deposition. Maximum flow rates for N_2 and O_2 are 500 sccm, for SiH_4 (low) is 100 sccm, for SiH_4 (coarse) is 1000 sccm.

Interval	Description	N_2 (%)	HCl (%)	SiH_4 #1 (%)	SiH_4 #2 (%)	Temp (°C)	Time (min)
0	Idle	30	0	0	0	625	0
1	Boat in	30	0	0	0	625	30
2	Stabilize	30	0	0	0	625	10
3	Pump and purge	30	0	0	0	625	45
4-6	Pump and purge	30	0	0	0	625	6
7	Deposit poly	0	0	90	32	625	16.2
8-14	Pump and purge	30	0	0	0	625	14
15	Purge to atm	30	0	0	0	625	11
16	Boat out	30	0	0	0	625	30

Table A.10: 1500 Å LPCVD polysilicon deposition recipe 423. Tube A6 is at a pressure of approximately 220 mTorr during deposition. Maximum flow rates for N_2 is 20 SLM, for SiH_4 #1 is 100 sccm, for SiH_4 #2 is 50 sccm.

Interval	Description	N_2 (%)	HCl (%)	SiH_4 #1 (%)	SiH_4 #2 (%)	Temp (°C)	Time (min)
0	Idle	30	0	0	0	625	0
1	Boat in	30	0	0	0	625	30
2	Stabilize	30	0	0	0	625	10
3	Pump and purge	30	0	0	0	625	45
4-6	Pump and purge	30	0	0	0	625	6
7	Deposit poly	0	0	90	32	625	300
8-14	Pump and purge	30	0	0	0	625	14
15	Purge to atm	30	0	0	0	625	11
16	Boat out	30	0	0	0	625	30

Table A.11: 2.5 μm LPCVD polysilicon deposition recipe 427. Tube A6 is at a pressure of approximately 220 mTorr during deposition. Maximum flow rates for N_2 is 20 SLM, for SiH_4 #1 is 100 sccm, for SiH_4 #2 is 50 sccm.

Interval	Description	N_2 (%)	O_2 (%)	$POCl_3$ (%)	O_2 (low) (%)	Temp (°C)	Time (min)
0	Idle	30	0	0	0	800	0
1	Boat in	90	0	0	0	800	20
2	Stabilize	90	0	0	0	800	10
3	Ramp up	60	0	0	0	10°C/min	12.5
4	Stabilize	60	0	0	0	925	10
5	Dope $POCl_3$	55	0	60	46	925	90
6	Oxidize cap	0	60	0	0	925	15
7	Stabilize	60	0	0	0	925	10
8	Ramp down	60	0	0	0	-2.5°C/min	50
9	Boat out	90	0	0	0	800	20

Table A.12: $POCl_3$ doping recipe 315 for 90 minutes. $POCl_3$ is liquid-source and tube A4 is at atmospheric pressure. Maximum flow rates for N_2 and O_2 are 10 SLM; and for $POCl_3$ and O_2 (low) are 500 sccm.

Interval	Description	N_2 (%)	O_2 (%)	$POCl_3$ (%)	O_2 (low) (%)	Temp (°C)	Time (min)
0	Idle	30	0	0	0	800	0
1	Boat in	90	0	0	0	800	20
2	Stabilize	90	0	0	0	800	10
3	Ramp up	60	0	0	0	10°C/min	12.5
4	Stabilize	60	0	0	0	925	10
5	Dope $POCl_3$	55	0	60	46	925	300
6	Oxidize cap	0	60	0	0	925	15
7	Stabilize	60	0	0	0	925	10
8	Ramp down	60	0	0	0	-2.5°C/min	50
9	Boat out	90	0	0	0	800	20

Table A.13: $POCl_3$ doping recipe 316 for 5 hours. $POCl_3$ is liquid-source and tube A4 is at atmospheric pressure. Maximum flow rates for N_2 and O_2 are 10 SLM; and for $POCl_3$ and O_2 (low) are 500 sccm.

Interval	Description	N_2 (sccm)	NH_3 (sccm)	SiH_2Cl_2 (sccm)	Temp (°C)	Time (min)
0	Idle	200	0	0	650	0
1	Boat in	10 SLM	0	0	650	30
2	Pump and Ramp-up	200	0	0	12°C/min	10
3	Leakcheck	200	0	0	775	10
4	Stabilize	200	0	0	775	20
5	NH_3 ramp	0	25	0	775	1
6	DCS ramp	0	25	250	775	1
7	Deposit nitride	0	25	250	775	see caption
8	Pump and purge	200	0	0	775	10
9	Backfill	200	0	0	775	10
10	Ramp down	200	0	0	-5°C/min	25
11	Boat out	10 SLM	0	0	650	30

Table A.14: Silicon-rich silicon nitride recipe for the vertical thermal reactor (VTR). Deposition occurs at a pressure of approximately 280 mTorr and a flow ratio of 10:1 (SiH_2Cl_2:NH_3). Deposition time during interval 7 for 4000 Å is 120 minutes and for 10000 Å is 280 minutes.

Appendix B

SUPREM-III Model

SUPREM-III [39] is used to determine one-dimensional diffusion profiles of the sensor and shield implant regions throughout the micromotor process sequence in Chapter 3. As a result of the study, an implant species with lower thermal diffusivity was chosen for the sensor implant electrodes. The following is a typical SUPREM-III input deck used to model the micromotor sensor process before addition of the sensor/stator shielding and surface passivation oxide steps.

```
title Micromotor SENSOR2 inversion channel

initialize silicon <100> concentration=1e15 Boron
+          thickness=3.0 dx=0.005 xdx=0.02 spaces=150

comment * dummy gate oxide
diffusion temp=800, time=10, nitrogen
diffusion temp=925, time=15, nitrogen
diffusion temp=925, time=25, dryo2
diffusion temp=925, time=30, nitrogen
diffusion temp=800, time=60, nitrogen

comment * field (B) and channel (As) threshold adjust impants
implant boron dose=5e12 energy=30
implant arsenic dose=5e12 energy=90

comment * strip dummy oxide
etch oxide all

comment * gate oxide
diffusion temp=800, time=10, nitrogen
diffusion temp=925, time=15, nitrogen
diffusion temp=925, time=25, dryo2
```

```
diffusion temp=925, time=30, nitrogen
diffusion temp=800, time=60, nitrogen

comment * LPCVD Polysilicon 3000 A
deposit polysilicon, thickness=0.3, temp=625
diffusion temp=625, time=100, nitrogen

comment * POCl Deposition (90 minutes)
diffusion temp=800, time=10, nitrogen
diffusion temp=925, time=22, nitrogen
diffusion temp=925, time=72, dryo2 solidsol phos
diffusion temp=925, time=15, dryo2
diffusion temp=925, time=10, nitrogen
diffusion temp=800, time=60, nitrogen

comment * strip PSG
etch oxide all

comment * S/D implants
implant arsenic dose=5e15 energy=90

comment * LPCVD Silicon Nitride 3000A
deposit nitride, thickness=0.3000, spaces=30
diffusion temp=800, time=160
diffusion temp=700, time=30

comment * LPCVD Polysilicon 2000 A
deposit polysilicon, thickness=0.3, temp=625
diffusion temp=625, time=100, nitrogen

comment * POCl Deposition (90 minutes)
diffusion temp=800, time=10, nitrogen
diffusion temp=925, time=22, nitrogen
diffusion temp=925, time=72, dryo2 solidsol phos
diffusion temp=925, time=15, dryo2
diffusion temp=925, time=10, nitrogen
diffusion temp=800, time=60, nitrogen

comment * strip PSG
etch oxide all

comment * etch poly
etch polysilicon all
```

```
comment * etch nitride contacts
etch nitride all

comment * LPCVD LTO 5000A
deposit oxide, thickness=0.5000
diffusion temp=350, time=35
diffusion temp=400, time=9

comment * etch oxide
etch oxide all

comment * LPCVD Polysilicon 1.5 A
deposit polysilicon, thickness=1.5, temp=625
diffusion temp=625, time=250, nitrogen

comment * POCl Deposition (5 hr minutes)
diffusion temp=800, time=10, nitrogen
diffusion temp=925, time=22, nitrogen
diffusion temp=925, time=300, dryo2 solidsol phos
diffusion temp=925, time=15, dryo2
diffusion temp=925, time=10, nitrogen
diffusion temp=800, time=60, nitrogen

comment * strip PSG
etch oxide all

comment * LPCVD LTO 1um
deposit oxide, thickness=1.0
diffusion temp=350, time=35
diffusion temp=400, time=9

comment * LPCVD LTO 5000A
deposit oxide, thickness=0.5
diffusion temp=350, time=35
diffusion temp=400, time=9

comment * LPCVD Silicon Nitride 10000A
comment *deposit nitride, thickness=1.000, spaces=30
diffusion temp=800, time=280
diffusion temp=700, time=30

comment * etch nitride
```

```
comment * etch nitride all

comment * etch oxide
etch oxide all

stop
```

Appendix C

Capacitance Matrix Extraction from FASTCAP

FASTCAP [68] produces a capacitance matrix which describes the charges on a system of electrodes in terms of the electrode voltages given with respect to a reference electrode at infinity. This capacitance matrix, while of fundamental importance, is inconvenient to use in many practical situations for two reasons. First, in many practical situations, the reference electrode from which voltages are specified is one of the electrodes in the system as opposed to the electrode at infinity. Second, in many practical situations, some of the conductors are charge constrained, not voltage constrained. The most common example is a 'floating' electrode on which the net charge is zero. As a consequence of these two reasons, an alternative capacitance matrix is desirable for the purpose of electromechanical analysis in such situations. The purpose of this appendix is to describe how to extract the alternative capacitance matrix from the output of FASTCAP.

As an example, consider a five electrode system shown in Figure C.1 where electrodes numbered 1, 2, 3 and 4 have finite separations between one another. Electrode number ∞ is at infinity. The charges on electrodes 1, 2, 3, 4 and ∞ are represented by q_1, q_2, q_3, q_4 and q_∞. The absolute voltages on electrodes 1, 2, 3 and 4 with respect to electrode ∞ are represented by $v_{1\infty}$, $v_{2\infty}$, $v_{3\infty}$ and $v_{4\infty}$. Electrode ∞ is defined to have a voltage of zero. FASTCAP analyzes the five electrode system described above to determine charges, normalized by the dielectric constant of free space so as to become 'capacitances', which result from experiments in which a given electrode is held at 1 Volt with respect to infinity while the other electrodes are all held at 0 Volts. The results are returned in the form of a capacitance matrix. The relationship

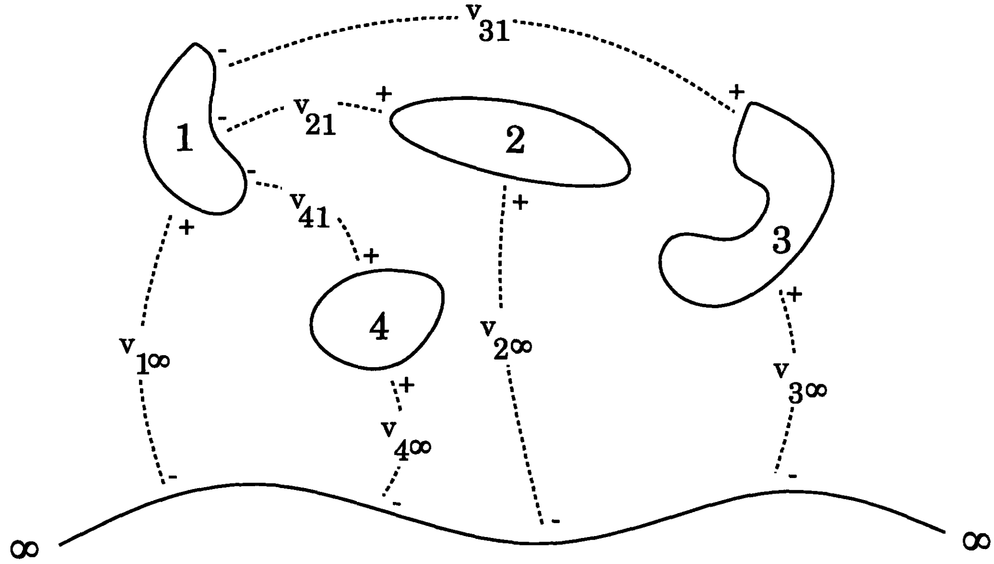

Figure C.1: Five electrode system.

between charges and voltages of the electrodes is given by

$$\begin{bmatrix} q_1 \\ q_2 \\ q_3 \\ q_4 \\ q_\infty \end{bmatrix} = \begin{bmatrix} C_{11} & C_{12} & C_{13} & C_{14} \\ C_{21} & C_{22} & C_{23} & C_{24} \\ C_{31} & C_{32} & C_{33} & C_{34} \\ C_{41} & C_{42} & C_{43} & C_{44} \\ -\sum C_{i1} & -\sum C_{i2} & -\sum C_{i3} & -\sum C_{i4} \end{bmatrix} \begin{bmatrix} v_{1\infty} \\ v_{2\infty} \\ v_{3\infty} \\ v_{4\infty} \end{bmatrix} \tag{C.1}$$

where the capacitance values are taken from the FASTCAP matrix. Note that the last row is redundant and is not provided by FASTCAP.

The first step in modifying Equation C.1 is to shift the reference electrode from infinity to one of the other four electrodes in the system. In this case choose electrode number 1 as the non-infinity reference and define the relative voltages between the reference electrode 1 and the other electrodes such that $v_{2\infty} = v_{21} + v_{1\infty}$, $v_{3\infty} = v_{31} + v_{1\infty}$, and $v_{4\infty} = v_{41} + v_{1\infty}$ as shown in Figure C.1. Next, the electrode at infinity

is made to float by constraining its net charge to be zero. This is consistent with most practical situations. Thus,

$$q_{\infty} = 0 \tag{C.2}$$

Assuming the system of five electrodes is charge neutral, and because infinity now has no net charge, the charge on reference electrode 1 forms an image of the charges on electrodes 2, 3 and 4, namely

$$q_1 = -q_2 - q_3 - q_4 \tag{C.3}$$

Substituting Equation (C.2) and Equation (C.3) into Equation (C.1), and using the definitions for $v_{2\infty}$, $v_{3\infty}$ and $v_{4\infty}$, the relationship in terms of voltages relative to the non-infinity reference is

$$\begin{bmatrix} -q_2 - q_3 - q_4 \\ q_2 \\ q_3 \\ q_4 \\ 0 \end{bmatrix} = \begin{bmatrix} C_{11} & C_{12} & C_{13} & C_{14} \\ C_{21} & C_{22} & C_{23} & C_{24} \\ C_{31} & C_{32} & C_{33} & C_{34} \\ C_{41} & C_{42} & C_{43} & C_{44} \\ -\sum C_{i1} & -\sum C_{i2} & -\sum C_{i3} & -\sum C_{i4} \end{bmatrix} \begin{bmatrix} v_{1\infty} \\ v_{21} + v_{1\infty} \\ v_{31} + v_{1\infty} \\ v_{41} + v_{1\infty} \end{bmatrix} \tag{C.4}$$

Solving for the reference voltage $v_{1\infty}$ in terms of the other voltages using the bottom row of Equation (C.4) yields

$$v_{1\infty} = -\frac{\sum C_{i2} v_{21}}{\sum C_{ij}} - \frac{\sum C_{i3} v_{31}}{\sum C_{ij}} - \frac{\sum C_{i4} C_{41}}{\sum C_{ij}} \tag{C.5}$$

Substituting Equation (C.5) into Equation (C.4) rows 2, 3, and 4 yields

$$\begin{bmatrix} q_2 \\ q_3 \\ q_4 \end{bmatrix} = \begin{bmatrix} C_{22} - \frac{\sum C_{2j} \sum C_{i2}}{\sum C_{ij}} & C_{23} - \frac{\sum C_{2j} \sum C_{i3}}{\sum C_{ij}} & C_{24} - \frac{\sum C_{2j} \sum C_{i4}}{\sum C_{ij}} \\ C_{32} - \frac{\sum C_{3j} \sum C_{i2}}{\sum C_{ij}} & C_{33} - \frac{\sum C_{3j} \sum C_{i3}}{\sum C_{ij}} & C_{34} - \frac{\sum C_{3j} \sum C_{i4}}{\sum C_{ij}} \\ C_{42} - \frac{\sum C_{4j} \sum C_{i2}}{\sum C_{ij}} & C_{43} - \frac{\sum C_{4j} \sum C_{i3}}{\sum C_{ij}} & C_{44} - \frac{\sum C_{4j} \sum C_{i4}}{\sum C_{ij}} \end{bmatrix} \begin{bmatrix} v_{21} \\ v_{31} \\ v_{41} \end{bmatrix} \tag{C.6}$$

The matrix in Equation (C.6) is a capacitance matrix between electrodes 1, 2, 3 and 4, where infinity is detached from the problem and allowed to 'float'. Electrodes 2, 3 and 4 are 'fixed' in voltage with respect to electrode 1. Namely, their voltage is constrained to remain at some level determined by an external source which provides the necessary charge allowing the voltage to remain constant. This is the form of capacitance matrix which is generally most useful for electromechanical analysis of lumped parameter systems.

The formulation may be extended to permit additional floating electrodes. A hybrid matrix equation results and may be reduced by removing the floating electrode rows and columns. For example, assume electrode 3 in the example above were a floating electrode having zero net charge ($q_3 = 0$). Equation (C.6) would be rewritten as follows

$$\begin{bmatrix} q_2 \\ 0 \\ q_4 \end{bmatrix} = \begin{bmatrix} C_{22} - \frac{\sum C_{2j} \sum C_{i2}}{\sum C_{ij}} & C_{23} - \frac{\sum C_{2j} \sum C_{i3}}{\sum C_{ij}} & C_{24} - \frac{\sum C_{2j} \sum C_{i4}}{\sum C_{ij}} \\ C_{32} - \frac{\sum C_{3j} \sum C_{i2}}{\sum C_{ij}} & C_{33} - \frac{\sum C_{3j} \sum C_{i3}}{\sum C_{ij}} & C_{34} - \frac{\sum C_{3j} \sum C_{i4}}{\sum C_{ij}} \\ C_{42} - \frac{\sum C_{4j} \sum C_{i2}}{\sum C_{ij}} & C_{43} - \frac{\sum C_{4j} \sum C_{i3}}{\sum C_{ij}} & C_{44} - \frac{\sum C_{4j} \sum C_{i4}}{\sum C_{ij}} \end{bmatrix} \begin{bmatrix} v_{21} \\ v_{31} \\ v_{41} \end{bmatrix} \tag{C.7}$$

Equation (C.7) should now be reduced to terms of constrained voltages and their associated charges. This is done by first eliminating row 3 in Equation (C.7) to determine voltage v_{31} in terms of the other voltages, and then using the resulting expression for v_{31} to eliminate v_{31} and the third column from Equation (C.7). This

results in

$$\begin{bmatrix} q_2 \\ \\ q_4 \end{bmatrix} = \begin{bmatrix} C'_{22} & C'_{24} \\ \\ C'_{42} & C'_{44} \end{bmatrix} \begin{bmatrix} v_{21} \\ \\ v_{41} \end{bmatrix} \tag{C.8}$$

where the primed capacitances are functions of the unprimed capacitances determined in the reduction of Equation (C.7). A capacitance matrix results for only the voltage constrained electrodes. Here the 'self-capacitance' of a given electrode represents the capacitance of that electrode to the reference electrode.

As an example of the above, consider five concentric spherical conducting shells in free space as shown in Figure C.2 with radii at 1, 2, 3, 4 and 5 meters. Using Gauss' Law and Faraday's Law the capacitance between any two neighboring shells n and $n+1$ is given by the equation

$$C_{n,n+1} = \frac{4\pi\epsilon_o}{\frac{1}{r_n} - \frac{1}{r_{n+1}}} \tag{C.9}$$

where ϵ_o is the dielectric constant of free space, r_n is the inner shell radius, and r_{n+1} is the outer shell radius. The capacitance between the outer most shell and infinity may be determined in the limit as $r_{n+1} \to \infty$ yielding

$$C_{n,\infty} = 4\pi\epsilon_o r_n \tag{C.10}$$

Using Equations (C.9) and (C.10) the exact analytical solution to the capacitance matrix can be computed in the FASTCAP form. In this form, each matrix row is constructed by constraining one shell (of that row number) to 1 Volt while constraining all other shells (including infinity) to 0 Volts. The resulting charge on each shell normalized by the dielectric constant of free space ϵ_o is entered in the corresponding column number. Applying Equations (C.9) and (C.10) to obtain the exact analytical

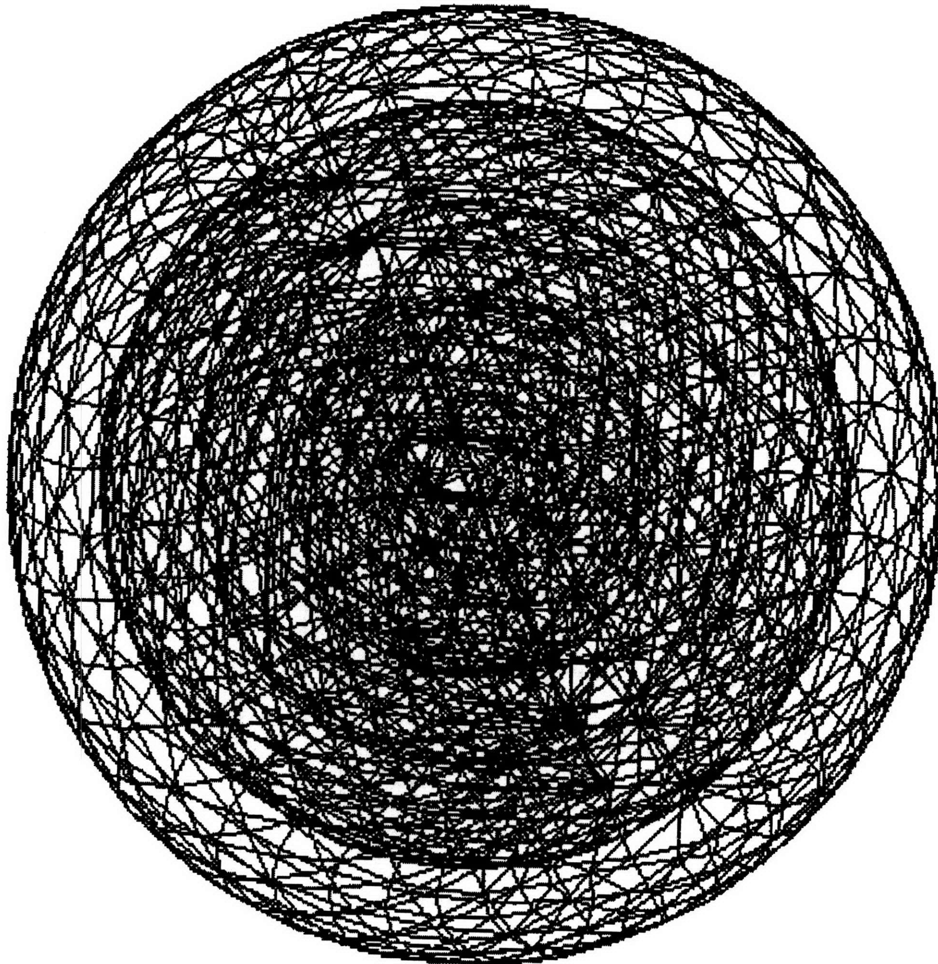

Figure C.2: Five concentric spherical conducting shells in free space.

solution to the capacitance matrix in FASTCAP form results in

$$\begin{bmatrix} 222.5 & -222.5 & 0 & 0 & 0 \\ -222.5 & 890.0 & -667.5 & 0 & 0 \\ 0 & -667.5 & 2003 & -1335 & 0 \\ 0 & 0 & -1335 & 3560 & -2225 \\ 0 & 0 & 0 & -2225 & 2781 \end{bmatrix} \tag{C.11}$$

where entries are in units of pico-Farads, the medium is free space with a dielectric constant ϵ_o, and the first row (column) corresponds to the shell at a 1 meter radius, the second row (column) corresponds to the shell at a 2 meter radius, and so on to the fifth row (column) which corresponds to the shell at a 5 meter radius.

A computer program POSTCAP acts as a post-processor to any FASTCAP output file and implements the matrix transformation described above. The POSTCAP source code listing is shown in Appendix D. One may select various electrodes in a FASTCAP problem as 'floating' (charge constrained to zero) or 'constrained' (voltage constrained) and obtain capacitances between the 'constrained' electrodes via POSTCAP. Continuing with the example having five concentric spherical shells, suppose we desire to compute the capacitance between the shell at 1 meter and the shell at 3 meters where the shell in between at 2 meters and the outer shells at 4 and 5 meters are allowed to 'float'. In this case, the entry in the FASTCAP matrix at location (1, 3) gives a value of 0 pF, which is clearly an incorrect result because FASTCAP has solved a different problem. Letting the reference electrode be electrode 1, POSTCAP returns a value of 167 pF as shown in Figure C.3 which is the correct answer, the capacitance between the shells at 1 meter and 2 meters in series with the capacitance of the shells at 2 meters and 3 meters.

```
POSTCAP capacitance matrix for FASTCAP file:  5_spheres.analytical.soln

   Number of conductors = 5
   Reference conductor: 1
   Floating conductor(s): 2 4 5
   Constrained conductor(s): 3


   POSTCAP input capacitance matrix from FASTCAP (pico-Farads):

                #1          #2          #3          #4          #5
     #1     2.225e+02  -2.225e+02   0.000e+00   0.000e+00   0.000e+00
     #2    -2.225e+02   8.900e+02  -6.675e+02   0.000e+00   0.000e+00
     #3     0.000e+00  -6.675e+02   2.003e+03  -1.335e+03   0.000e+00
     #4     0.000e+00   0.000e+00  -1.335e+03   3.560e+03  -2.225e+03
     #5     0.000e+00   0.000e+00   0.000e+00  -2.225e+03   2.781e+03


   Capacitance matrix of constrained conductors with respect to reference:

                #3
     #3     1.669e+02
```

Figure C.3: POSTCAP run of five concentric shells example from exact analytical solution (in FASTCAP form).

Appendix D

Computer Software

This appendix lists the source code SENSOR.C for the position data extraction algorithm used to interpret the raw data of three sensor signals to give rotor position in time, and the source code POSTCAP.C used to extract finite electrode referenced capacitance matricies with voltage or charge fixed electrodes from the electrostatic solver FASTCAP []. POSTCAP.C incorporates matrix inversion routines from *Numerical Recipes in C* [].

D.1 SENSOR.C

```
/*  SENSOR.C position data extraction code
 *                     Eckart Jansen
 */

#include <math.h>
#include <stdio.h>
#include <string.h>

#define maxData 20000
#define PI 3.14159265358979323846264 33

int numData,numdrives;
double time[maxData],A[maxData],drvtime,driveTime[maxData],winwidth;
double s1[maxData],s2[maxData],s3[maxData];
double angle1[maxData],angle2[maxData],angle3[maxData],angleAvg[maxData];
double angle1A[maxData],angle2A[maxData],angle3A[maxData];
double angle1B[maxData],angle2B[maxData],angle3B[maxData];
double vel1[maxData],vel2[maxData],vel3[maxData],velAvg[maxData];
double accel1[maxData],accel2[maxData],accel3[maxData],accelAvg[maxData];
FILE *inptr1,*inptr2,*inptr3,*outptr1,*outptr2,*outptr3,*outptr4;
```

```
FILE *outptr5,*outptr6;
char infile1[35],infile2[35],infile3[35];
char outfile1[35],outfile2[35],outfile3[35],outfile4[35];
char outfile5[35],outfile6[35];

/* Get user input and output file names */

void interactUser()
{
  printf("\n");
  printf("\n");
  printf("Sensor #1 .dat file? ");
  gets(infile1);
  printf("Sensor #2 .dat file? ");
  gets(infile2);
  printf("Sensor #3 .dat file? ");
  gets(infile3);
  printf("Theta #1 output file?");
  gets(outfile1);
  printf("Theta #2 output file?");
  gets(outfile2);
  printf("Theta #3 output file?");
  gets(outfile3);

  printf("Drive spikes removed sensor #1 output file? ");
  gets(outfile4);
  printf("Drive spikes removed sensor #2 output file? ");
  gets(outfile5);
  printf("Drive spikes removed sensor #3 output file? ");
  gets(outfile6);

  printf("Number of drive transitions?");
  scanf("%d",&numdrives);
  printf("Interpolation window width (sec)?");
  scanf("%lf",&winwidth);
  for (i=1;i<=numdrives;i++) {
    printf("Transition time %d (sec)?",i);
    scanf("%lf",&drvtime);
    driveTime[i]=drvtime;
  printf("\n");
}

/* Import sensor data from user input files */

void importData()
{
```

```
  int i;
  double t,val;

  i=0;
  inptr1 = fopen(infile1,"r");
  while ( fscanf(inptr1,"%lf,%lf",(&t),(&val)) != EOF ) {
    i++;
    s1[i]=val;
  }
  fclose(inptr1);

  i=0;
  inptr2 = fopen(infile2,"r");
  while ( fscanf(inptr2,"%lf,%lf",(&t),(&val)) != EOF ) {
    i++;
    s2[i]=val;
  }
  fclose(inptr2);

  i=0;
  inptr3 = fopen(infile3,"r");
  while ( fscanf(inptr3,"%lf,%lf",(&t),(&val)) != EOF ) {
    i++;
    time[i]=t;
    s3[i]=val;
  }
  fclose(inptr3);
  numData=i;
}

/* Replace drive spikes in sensor signal by linear interpolation */
between sensor data at edges of drive transition window */

void remove_drive_spikes()
{
  int i,j,startN[100], middleN[100], endN[100], halfwidthN;
  double timeslice,slope1,slope2,slope3;


  timeslice = (time[numData] - time[1])/numData;
  halfwidthN = (int)(winwidth / (2.0*timeslice));

  for (i=1;i<=numdrives;i++) {
    middleN[i] = (int)((driveTime[i] - time[1]) / timeslice);
    startN[i] = middleN[i] - halfwidthN;
    endN[i] = middleN[i] + halfwidthN;
```

```
    if (endN[i] > numData) endN[i] = numData;
    if (startN[i] < 1) startN[i] = 1;
  }
  for (i=1;i<=numdrives;i++) {
    slope1 = (s1[endN[i]] - s1[startN[i]])/winwidth;
    slope2 = (s2[endN[i]] - s2[startN[i]])/winwidth;
    slope3 = (s3[endN[i]] - s3[startN[i]])/winwidth;
    for(j=startN[i];j<=endN[i];j++){
      s1[j] = s1[startN[i]] + slope1*timeslice*(j - startN[i]);
      s2[j] = s2[startN[i]] + slope2*timeslice*(j - startN[i]);
      s3[j] = s3[startN[i]] + slope3*timeslice*(j - startN[i]);
    }
  }
}

/* Run an averaging window filter through data to remove noise */

void window_filter()
{
  int i,j,winsize;
  double sum,sw1[maxData],sw2[maxData],sw3[maxData];

  winsize = 10;

/* Sensor #1 data */

  for (i=winsize;i<=numData;i++) {
      sum = 0.0;
      for (j=1;j<=winsize;j++) sum += s1[i-j+1];
      sw1[i] = sum/winsize;
    }
  for (i=1;i<winsize;i++) sw1[i]=sw1[winsize];  /* pad with first data point */
  for (i=1;i<=numData;i++) s1[i] = sw1[i];  /* transfer back to data array */

/* Sensor #2 data */

  for (i=winsize;i<=numData;i++) {
      sum = 0.0;
      for (j=1;j<=winsize;j++) sum += s2[i-j+1];
      sw2[i] = sum/winsize;
    }
  for (i=1;i<winsize;i++) sw2[i]=sw2[winsize];  /* pad with first data point */
  for (i=1;i<=numData;i++) s2[i] = sw2[i];  /* transfer back to data array */

/* Sensor #3 data */
```

```
  for (i=winsize;i<=numData;i++) {
      sum = 0.0;
      for (j=1;j<=winsize;j++) sum += s3[i-j+1];
      sw3[i] = sum/winsize;
    }
  for (i=1;i<winsize;i++) sw3[i]=sw3[winsize];  /* pad with first data point*/
  for (i=1;i<=numData;i++) s3[i] = sw3[i];  /* transfer back to data array */

}

/* Normalize all data to lie centered about 0 with unity amplitude */

void normalize_peak()
{
  int i;
  double hipeak,lopeak;

  hipeak=s1[1];
  lopeak=s1[1];
  for (i=1;i<=numData;i++) if (hipeak < s1[i]) hipeak = s1[i];
  for (i=1;i<=numData;i++) if (lopeak > s1[i]) lopeak = s1[i];
  for (i=1;i<=numData;i++) s1[i] = (s1[i] - (lopeak + (hipeak-lopeak)/2)) /
((hipeak-lopeak)/2);

  hipeak=s2[1];
  lopeak=s2[1];
  for (i=1;i<=numData;i++) if (hipeak < s2[i]) hipeak = s2[i];
  for (i=1;i<=numData;i++) if (lopeak > s2[i]) lopeak = s2[i];
  for (i=1;i<=numData;i++) s2[i] = (s2[i] - (lopeak + (hipeak-lopeak)/2)) /
((hipeak-lopeak)/2);

  hipeak=s3[1];
  lopeak=s3[1];
  for (i=1;i<=numData;i++) if (hipeak < s3[i]) hipeak = s3[i];
  for (i=1;i<=numData;i++) if (lopeak > s3[i]) lopeak = s3[i];
  for (i=1;i<=numData;i++) s3[i] = (s3[i] - (lopeak + (hipeak-lopeak)/2)) /
((hipeak-lopeak)/2);
}

/* Neighbor function for clustering algorithm returns the nearest
   distance on a circle of the angB from reference angA
*/

double neighbor(angA,angB)
double angA, angB;
{
```

```
  if (fabs(angB - angA) <= PI) return angB;
  if (angB >  angA) return (angB - 2.0*PI);
  if (angB <= angA) return (angB + 2.0*PI);
}

/* Compute two possible angles during inverse sine operation and
   pick the correct angle.
*/

void compute_angle()
{
  int i;
  double sum1A2A3A,sum1A2A3B,sum1A2B3A,sum1A2B3B;
  double sum1B2A3A,sum1B2A3B,sum1B2B3A,sum1B2B3B;
  double avg1A2A3A,avg1A2A3B,avg1A2B3A,avg1A2B3B;
  double avg1B2A3A,avg1B2A3B,avg1B2B3A,avg1B2B3B;
  double sum,ang1,ang2,ang3,avg;
  double x,y,z,a;
  double ang1uncycle, ang2uncycle, ang3uncycle;

/* compute both possible angles (A and B) when taking inverse sine */

  for (i=1;i<=numData;i++) {

    angle1A[i] =      asin(s1[i]);
    angle1B[i] = PI - asin(s1[i]);
    angle2A[i] =      asin(s2[i]) + 2.0*PI/3.0;
    angle2B[i] = PI - asin(s2[i]) + 2.0*PI/3.0;
    angle3A[i] =      asin(s3[i]) - 2.0*PI/3.0;
    angle3B[i] = PI - asin(s3[i]) - 2.0*PI/3.0;

/* shift all angles between 0 and 2PI degrees */

    if (angle1A[i] < -2.0*PI) angle1A[i] +=  2.0*PI;
    if (angle1A[i] < 0.0)     angle1A[i] +=  2.0*PI;
    if (angle1A[i] >= 2.0*PI)  angle1A[i] += -2.0*PI;

    if (angle1B[i] < -2.0*PI) angle1B[i] +=  2.0*PI;
    if (angle1B[i] < 0.0)     angle1B[i] +=  2.0*PI;
    if (angle1B[i] >= 2.0*PI)  angle1B[i] += -2.0*PI;

    if (angle2A[i] < -2.0*PI) angle2A[i] +=  2.0*PI;
    if (angle2A[i] < 0.0)     angle2A[i] +=  2.0*PI;
    if (angle2A[i] >= 2.0*PI)  angle2A[i] += -2.0*PI;

    if (angle2B[i] < -2.0*PI) angle2B[i] +=  2.0*PI;
```

```
    if (angle2B[i] < 0.0)     angle2B[i] +=  2.0*PI;
    if (angle2B[i] >= 2.0*PI)  angle2B[i] += -2.0*PI;

    if (angle3A[i] < -2.0*PI) angle3A[i] +=  2.0*PI;
    if (angle3A[i] < 0.0)     angle3A[i] +=  2.0*PI;
    if (angle3A[i] >= 2.0*PI)  angle3A[i] += -2.0*PI;

    if (angle3B[i] < -2.0*PI) angle3B[i] +=  2.0*PI;
    if (angle3B[i] < 0.0)     angle3B[i] +=  2.0*PI;
    if (angle3B[i] >= 2.0*PI)  angle3B[i] += -2.0*PI;
}

/* Compute clustering sum (RMS error) and find the minimum error to
   determine which of angle A or B is the correct angle
*/

  for (i=1;i<=numData;i++) {
    /* 1A2A3A */
    x = angle1A[i];
    y = neighbor(angle1A[i],angle2A[i]);
    z = neighbor(angle1A[i],angle3A[i]);
    a = (x + y + z)/3.0;
    sum1A2A3A = ((x-a)*(x-a)) + ((y-a)*(y-a)) + ((z-a)*(z-a));
    /* 1A2A3B */
    x = angle1A[i];
    y = neighbor(angle1A[i],angle2A[i]);
    z = neighbor(angle1A[i],angle3B[i]);
    a = (x + y + z)/3.0;
    sum1A2A3B = ((x-a)*(x-a)) + ((y-a)*(y-a)) + ((z-a)*(z-a));
    /* 1A2B3A */
    x = angle1A[i];
    y = neighbor(angle1A[i],angle2B[i]);
    z = neighbor(angle1A[i],angle3A[i]);
    a = (x + y + z)/3.0;
    sum1A2B3A = ((x-a)*(x-a)) + ((y-a)*(y-a)) + ((z-a)*(z-a));
    /* 1A2B3B */
    x = angle1A[i];
    y = neighbor(angle1A[i],angle2B[i]);
    z = neighbor(angle1A[i],angle3B[i]);
    a = (x + y + z)/3.0;
    sum1A2B3B = ((x-a)*(x-a)) + ((y-a)*(y-a)) + ((z-a)*(z-a));
    /* 1B2A3A */
    x = angle1B[i];
    y = neighbor(angle1B[i],angle2A[i]);
    z = neighbor(angle1B[i],angle3A[i]);
    a = (x + y + z)/3.0;
```

```
    sum1B2A3A = ((x-a)*(x-a)) + ((y-a)*(y-a)) + ((z-a)*(z-a));
    /* 1B2A3B */
    x = angle1B[i];
    y = neighbor(angle1B[i],angle2A[i]);
    z = neighbor(angle1B[i],angle3B[i]);
    a = (x + y + z)/3.0;
    sum1B2A3B = ((x-a)*(x-a)) + ((y-a)*(y-a)) + ((z-a)*(z-a));
    /* 1B2B3A */
    x = angle1B[i];
    y = neighbor(angle1B[i],angle2B[i]);
    z = neighbor(angle1B[i],angle3A[i]);
    a = (x + y + z)/3.0;
    sum1B2B3A = ((x-a)*(x-a)) + ((y-a)*(y-a)) + ((z-a)*(z-a));
    /* 1B2B3B */
    x = angle1B[i];
    y = neighbor(angle1B[i],angle2B[i]);
    z = neighbor(angle1B[i],angle3B[i]);
    a = (x + y + z)/3.0;
    sum1B2B3B = ((x-a)*(x-a)) + ((y-a)*(y-a)) + ((z-a)*(z-a));

/* trickle down to find minimum sum (RMS error) */

      sum=sum1A2A3A;
      ang1=angle1A[i];
      ang2=angle2A[i];
      ang3=angle3A[i];

    if (sum > sum1A2A3B) {
      sum=sum1A2A3B;
      ang1=angle1A[i];
      ang2=angle2A[i];
      ang3=angle3B[i];
    }
    if (sum > sum1A2B3A) {
      sum=sum1A2B3A;
      ang1=angle1A[i];
      ang2=angle2B[i];
      ang3=angle3A[i];
    }
    if (sum > sum1A2B3B) {
      sum=sum1A2B3B;
      ang1=angle1A[i];
      ang2=angle2B[i];
      ang3=angle3B[i];
    }
    if (sum > sum1B2A3A) {
```

```
      sum=sum1B2A3A;
      ang1=angle1B[i];
      ang2=angle2A[i];
      ang3=angle3A[i];
    }
    if (sum > sum1B2A3B) {
      sum=sum1B2A3B;
      ang1=angle1B[i];
      ang2=angle2A[i];
      ang3=angle3B[i];
    }
    if (sum > sum1B2B3A) {
      sum=sum1B2B3A;
      ang1=angle1B[i];
      ang2=angle2B[i];
      ang3=angle3A[i];
    }
    if (sum > sum1B2B3B) {
      sum=sum1B2B3B;
      ang1=angle1B[i];
      ang2=angle2B[i];
      ang3=angle3B[i];
    }
    angle1[i]=ang1;
    angle2[i]=ang2;
    angle3[i]=ang3;
  }

/* Uncycle data - so all data moves monotonically upward */

  ang1uncycle = 0.0;
  ang2uncycle = 0.0;
  ang3uncycle = 0.0;
  for (i=1;i<=numData-1;i++) {
    if ((angle1[i] - angle1[i+1]) > PI) ang1uncycle += 2*PI;
    if ((angle1[i+1] - angle1[i]) > PI) ang1uncycle -= 2*PI;
    if ((angle2[i] - angle2[i+1]) > PI) ang2uncycle += 2*PI;
    if ((angle2[i+1] - angle2[i]) > PI) ang2uncycle -= 2*PI;
    if ((angle3[i] - angle3[i+1]) > PI) ang3uncycle += 2*PI;
    if ((angle3[i+1] - angle3[i]) > PI) ang3uncycle -= 2*PI;
    angle1[i] += ang1uncycle;
    angle2[i] += ang2uncycle;
    angle3[i] += ang3uncycle;
  }

/* Remove spikes 1 */
```

```
    for (i=1;i<=numData-2;i++) {
      if (((angle1[i] - angle1[i+1]) > PI) && ((angle1[i+2] - angle1[i+1])
> PI))
angle1[i+1] = (angle1[i] + angle1[i+2])/2.0;
      if (((angle1[i+1] - angle1[i]) > PI) && ((angle1[i+1] - angle1[i+2])
> PI))
angle1[i+1] = (angle1[i] + angle1[i+2])/2.0;
      if (((angle2[i] - angle2[i+1]) > PI) && ((angle2[i+2] - angle2[i+1])
> PI))
angle2[i+1] = (angle2[i] + angle2[i+2])/2.0;
      if (((angle2[i+1] - angle2[i]) > PI) && ((angle2[i+1] - angle2[i+2])
> PI))
angle2[i+1] = (angle2[i] + angle2[i+2])/2.0;
      if (((angle3[i] - angle3[i+1]) > PI) && ((angle3[i+2] - angle3[i+1])
> PI))
angle3[i+1] = (angle3[i] + angle3[i+2])/2.0;
      if (((angle3[i+1] - angle3[i]) > PI) && ((angle3[i+1] - angle3[i+2])
> PI))
angle3[i+1] = (angle3[i] + angle3[i+2])/2.0;
  }

/* Remove spikes 2 */

    for (i=1;i<=numData-3;i++) {
      if (((angle1[i] - angle1[i+1]) > PI) && ((angle1[i+3] - angle1[i+1]) > PI))
angle1[i+1] = (angle1[i] + angle1[i+3])/2.0;
      if (((angle1[i+1] - angle1[i]) > PI) && ((angle1[i+1] - angle1[i+3]) > PI))
angle1[i+1] = (angle1[i] + angle1[i+3])/2.0;
      if (((angle2[i] - angle2[i+1]) > PI) && ((angle2[i+3] - angle2[i+1]) > PI))
angle2[i+1] = (angle2[i] + angle2[i+3])/2.0;
      if (((angle2[i+1] - angle2[i]) > PI) && ((angle2[i+1] - angle2[i+3]) > PI))
angle2[i+1] = (angle2[i] + angle2[i+3])/2.0;
      if (((angle3[i] - angle3[i+1]) > PI) && ((angle3[i+3] - angle3[i+1]) > PI))
angle3[i+1] = (angle3[i] + angle3[i+3])/2.0;
      if (((angle3[i+1] - angle3[i]) > PI) && ((angle3[i+1] - angle3[i+3]) > PI))
angle3[i+1] = (angle3[i] + angle3[i+3])/2.0;
  }

/* Remove spikes 3 */

    for (i=1;i<=numData-3;i++) {
      if (((angle1[i] - angle1[i+2]) > PI) && ((angle1[i+3] - angle1[i+2]) > PI))
angle1[i+2] = (angle1[i] + angle1[i+3])/2.0;
      if (((angle1[i+2] - angle1[i]) > PI) && ((angle1[i+2] - angle1[i+3]) > PI))
angle1[i+2] = (angle1[i] + angle1[i+3])/2.0;
```

```
      if (((angle2[i] - angle2[i+2]) > PI) && ((angle2[i+3] - angle2[i+2]) > PI))
angle2[i+2] = (angle2[i] + angle2[i+3])/2.0;
      if (((angle2[i+2] - angle2[i]) > PI) && ((angle2[i+2] - angle2[i+3]) > PI))
angle2[i+2] = (angle2[i] + angle2[i+3])/2.0;
      if (((angle3[i] - angle3[i+2]) > PI) && ((angle3[i+3] - angle3[i+2]) > PI))
angle3[i+2] = (angle3[i] + angle3[i+3])/2.0;
      if (((angle3[i+2] - angle3[i]) > PI) && ((angle3[i+2] - angle3[i+3]) > PI))
angle3[i+2] = (angle3[i] + angle3[i+3])/2.0;
  }

/* Average data */

  for (i=1;i<=numData;i++) angleAvg[i]=(angle1[i] + angle2[i] + angle3[i])/3.0;

}

/* Export data to user output files */

void exportData()
{
  int i;

  outptr1 = fopen(outfile1,"w");
  for (i=10;i<=numData-2;i++) fprintf(outptr1,"%f,%f\n",time[i],angle1[i]/4.0);
  fclose(outptr1);

  outptr2 = fopen(outfile2,"w");
  for (i=10;i<=numData-2;i++) fprintf(outptr2,"%f,%f\n",time[i],angle2[i]/4.0);
  fclose(outptr2);

  outptr3 = fopen(outfile3,"w");
  for (i=10;i<=numData-2;i++) fprintf(outptr3,"%f,%f\n",time[i],angle3[i]/4.0);
  fclose(outptr3);
}

/* Main program */

main()  {

  interactUser();
  importData();
  remove_drive_spikes();
  window_filter();
  normalize_peak();
  compute_angle();
  exportData();
```

```
  printf("\nDone.\n\n");
}
```

D.2 POSTCAP.C

```
/*
 *                       POSTCAP.C
 *
 *    FASTCAP  Capacitance Matrix Extraction Utility
 *              Eckart Jansen
 */
#include <math.h>
#include <stdio.h>
#include <string.h>
#define MaxCond 100     /* Maximum number of conductors */
#define TINY 1.0e-20

int numcond,numflo,numfix,ref,flo[MaxCond],fix[MaxCond];
double Cin[MaxCond][MaxCond],Cout[MaxCond][MaxCond];
double Cflo[MaxCond][MaxCond], Cfix[MaxCond][MaxCond];
double invCflo[MaxCond][MaxCond], Ctemp1[MaxCond][MaxCond];
double Ctemp2[MaxCond][MaxCond], Cinter[MaxCond][MaxCond];
char numconds[2],flofixs[1],refs[2];
char infile[35],outfile[35];
FILE *inptr,*outptr;

/* Get number of conductors, conductor information, and file name
   from the user. */

void interactUser()
{
  int i;

  printf("\n\n");
  printf("Number of conductors (excluding infinity)? ");
  gets(numconds);
  numcond=atoi(numconds);
  printf("Reference conductor? ");
  gets(refs);
  ref=atoi(refs);
  numflo=0;
  numfix=0;
  for (i=1;i<=numcond;i++)
```

```
    if (i != ref) {
      printf("Is conductor %d's potential floating or controlled (f,c)? ");
      gets(flofixs);
      if (flofixs[0] == 'f') {
numflo++;
flo[numflo]=i;
      }
     /* "controlled" == "fixed" */
      if (flofixs[0] == 'c') {
numfix++;
fix[numfix]=i;
      }
    }
  printf("FASTCAP file? ");
  gets(infile);
  printf("Output file?");
  gets(outfile);
  printf("\n");
}

/* Get capacitance matrix from FASTCAP file */

void importData()
{
  int i,j,numperc;
  char dummy1;
  double val;

  inptr = fopen(infile,"r");
  numperc=0;
  while (numperc < (2+numcond)) {
    dummy1 = fgetc(inptr);
    if (dummy1 == '%') numperc++;     /* look for '%' characters */
  }
  for (i=1;i<=12;i++) dummy1 = fgetc(inptr);
  for (i=1;i<=numcond;i++) {
    fscanf(inptr,"%lf",(&val));
    Cin[i][1]=val;
  }
  for (j=2;j<=numcond;j++) {
    for (i=1;i<=14;i++) dummy1 = fgetc(inptr);
    for (i=1;i<=numcond;i++) {
      fscanf(inptr,"%lf",(&val));
      Cin[i][j]=val;
    }
  }
```

```
  fclose(inptr);
}

/* Matrix inversion of Cflo matrix, adapted from Numerical Recipes in C */

void invertCflo()
{
  int i,ii,ip,imax,j,j2,k,n,i3,j3;
  int indx[MaxCond];
  double big,dum,sum,temp;
  double vv[MaxCond];
  double a[MaxCond][MaxCond],b[MaxCond],d;

  n=numflo;
  for (i=1;i<=n;i++)
    for (j=1;j<=n;j++) a[i][j]=Cflo[i][j];

/* LU decomposition */

  d=1.0;
  for (i=1;i<=n;i++) {
    big=0.0;
    for (j=1;j<=n;j++)
      if ((temp=fabs(a[i][j])) > big) big=temp;
    if (big == 0.0) printf("Singular matrix \n");
    vv[i]=1.0/big;
  }
  for (j=1;j<=n;j++) {
    for (i=1;i<j;i++) {
      sum=a[i][j];
      for (k=1;k<i;k++) sum -= a[i][k]*a[k][j];
      a[i][j]=sum;
    }
    big=0.0;
    for (i=j;i<=n;i++) {
      sum=a[i][j];
      for (k=1;k<j;k++)
 sum -= a[i][k]*a[k][j];
      a[i][j]=sum;
      if ( (dum=vv[i]*fabs(sum)) >= big) {
 big=dum;
 imax=i;
      }
    }
    if (j != imax) {
      for (k=1;k<=n;k++) {
```

```
dum=a[imax][k];
a[imax][k]=a[j][k];
a[j][k]=dum;
      }
      d = -d;
      vv[imax]=vv[j];
    }
    indx[j]=imax;
    if (a[j][j] == 0.0) a[j][j]=TINY;
    if (j != n) {
      dum=1.0/(a[j][j]);
      for (i=j+1;i<=n;i++) a[i][j] *= dum;
    }
  }

/* LU backsolve */

  for(j=1;j<=n;j++) {
    for(i=1;i<=n;i++) b[i]=0.0;
    b[j]=1.0;
    ii=0;
    for (i=1;i<=n;i++) {
      ip=indx[i];
      sum=b[ip];
      b[ip]=b[i];
      if (ii)
for (j2=ii;j2<=i-1;j2++) sum -= a[i][j2]*b[j2];
      else if (sum) ii=i;
      b[i]=sum;
    }
    for (i=n;i>=1;i--) {
      sum=b[i];
      for (j2=i+1;j2<=n;j2++) sum -= a[i][j2]*b[j2];
      b[i]=sum/a[i][i];
    }
    for(i=1;i<=n;i++) invCflo[i][j]=b[i];
  }
}

/* Numerical analysis procedure */

void crunchData()
{
   int i,j,k,l,m;
   double sumCij,sumCi,sumCj,sum;
```

```
/* adjust cap matrix so infinity has net charge 0 */

   sumCij=0.0;
   for (i=1;i<=numcond;i++)
     for (j=1;j<=numcond;j++) sumCij += Cin[i][j];
   for (i=1;i<=numcond;i++)
     for (j=1;j<=numcond;j++) {
       sumCi=0.0;
       sumCj=0.0;
       for (l=1;l<=numcond;l++) sumCi += Cin[l][j];
       for (m=1;m<=numcond;m++) sumCj += Cin[i][m];
       Cinter[i][j] = Cin[i][j] - sumCi*sumCj/sumCij;
     }

/* stuff float and fixed matrices */

   for (i=1;i<=numflo;i++)
     for (j=1;j<=numflo;j++)
       Cflo[i][j] = Cinter[flo[i]][flo[j]];

   for (i=1;i<=numflo;i++)
     for (j=1;j<=numfix;j++)
       Cfix[i][j] = Cinter[flo[i]][fix[j]];

/* Compute floating voltages in terms of fixed voltages */
/* invert float matrix */

   invertCflo();

/* multiply inv(float) by -1 */

  for(i=1;i<=numflo;i++)
    for(j=1;j<=numflo;j++)
      Ctemp1[i][j] = -1.0 * invCflo[i][j];

/* multiply -inv(float) matrix by fixed matrix */

  for(i=1;i<=numflo;i++)
    for(j=1;j<=numfix;j++) {
      sum=0.0;
      for(k=1;k<=numflo;k++) sum += Ctemp1[i][k] * Cfix[k][j];
      Ctemp2[j][i] = sum;
    }

/* Substitute floating voltages (in terms of fixed voltages) */
/* back into cap matrix and reduce matrix dimention to only fixed voltages */
```

```
/* output in Cout */

   for (i=1;i<=numfix;i++)
     for (j=1;j<=numfix;j++) {
       sum=0.0;
       for (k=1;k<=numflo;k++) sum += Cinter[fix[j]][flo[k]]*Ctemp2[j][k];
       Cout[i][j] = Cinter[fix[i]][fix[j]] + sum;
     }
}

/*  Write output file */

void exportData()
 {
   int i,j;

   outptr = fopen(outfile,"w");
   fprintf(outptr,"\n\n");
   fprintf(outptr,"POSTCAP capacitance matrix for FASTCAP file:  %s  \n \n",
infile);
   fprintf(outptr,"Number of conductors = %d  \n",numcond);
   fprintf(outptr,"Reference conductor: %d  \n",ref);
   fprintf(outptr,"Floating conductor(s): ");
   for (i=1;i<=numflo;i++) fprintf(outptr,"%d ",flo[i]);
   fprintf(outptr,"\n");
   fprintf(outptr,"Constrained conductor(s): ");
   for (i=1;i<=numfix;i++) fprintf(outptr,"%d ",fix[i]);
   fprintf(outptr,"\n\n\n");
   fprintf(outptr,"POSTCAP input capacitance matrix from FASTCAP
(same units):\n");
   fprintf(outptr,"\n");
   fprintf(outptr,"        ");
   for (i=1;i<=numcond;i++) fprintf(outptr,"   #%d    ",i);
   fprintf(outptr,"\n");
   for (i=1;i<=numcond;i++) {
     fprintf(outptr,"     #%d   ",i);
     for (j=1;j<=numcond;j++) fprintf(outptr," %0.3e ",Cin[i][j]);
    fprintf(outptr,"\n");
  }
   fprintf(outptr,"\n\n\n");
   fprintf(outptr,"Capacitance matrix of constrained conductors with respect
to reference:\n");
   fprintf(outptr,"\n");
   fprintf(outptr,"        ");
   for (i=1;i<=numfix;i++) fprintf(outptr,"      #%d    ",fix[i]);
   fprintf(outptr,"\n");
```

```
   for (i=1;i<=numfix;i++) {
     fprintf(outptr,"     #%d   ",fix[i]);
     for (j=1;j<=numfix;j++) fprintf(outptr,"   %0.3e   ",Cout[i][j]);
    fprintf(outptr,"\n");
  }
  fclose(outptr);
}

/* Main program */

main()  {
  int i,j;

  interactUser();
  importData();
  crunchData();
  exportData();
  printf("\nDone.\n\n");
}
```

References

[1] Photronics, Inc., Sunnyvale, CA.

[2] C. H. Ahn, Y. J. Kim, and M. G. Allen. A planar variable reluctance magnetic micromotor with fully integrated stator and coils. *IEEE Journal of Microelectromechanical Systems*, 2(4):165–173, Dec. 1993.

[3] S. Akamine, T. R. Albrecht, M. J. Zdeblick, and C. F. Quate. A planar process for microfabrication of a scanning tunneling microscope. *Sensors and Actuators*, A21–A23:964–970, 1990.

[4] S. F. Bart. *Modeling and Design of Electroquasistatic Microactuators.* PhD thesis, Massachusetts Institute of Technology, Cambridge, MA, 1990.

[5] S. F. Bart, T. A. Lober, R. T. Howe, J. H. Lang, and M. F. Schlecht. Design considerations for micromachined electric actuators. *Sensors and Actuators*, 14:269–292, 1988.

[6] S. F. Bart, M. Mehregany, L. S. Tavrow, J. H. Lang, and S. D. Senturia. Measurements of electric micromotor dynamics. In *Microstructures, Sensors, and Actuators*, pages 19–29, Dallas, TX, Nov. 25–30, 1990. ASME DSC–Vol. 19.

[7] S. F. Bart, M. Mehregany, L. S. Tavrow, J. H. Lang, and S. D. Senturia. Electric micromotor dynamics. *IEEE Trans. on Electron Devices*, ED–39(3):566–575, Mar. 1992.

[8] S. F. Bart, L. S. Tavrow, M. Mehregany, and J. H. Lang. Microfabricated electrohydrodynamic pumps. *Sensors and Actuators*, A21:193–197, 1990.

[9] P. Bergveld. Development, operation, and application of the ion–sensitive field effect transistor as a tool for electrophysiology. *IEEE Trans. Biomedical Engineering*, BME–19:342–351, Sept. 1972.

[10] G. C. Billingsley. *Program Reference for KIC.* Electronics Research Lab., E.E.C.S. Dept., U. C. Berkeley, 1983.

[11] B. Bollée. Electrostatic motors. *Philips Technical Review*, 30(6/7):178–194, 1969.

[12] R. B. Brown, M.-L. Ger, and T. Nguyen. Characterization of molybdenum thin films for micromechanical structures. In *Proceedings of the 3rd IEEE Workshop on Micro Electro Mechanical Systems*, pages 77–81, Napa Valley, CA, 1990.

[13] L. Y. Chen, Z. L. Zhang, J. J. Yao, D. C. Thomas, and N. C. MacDonald. Selective chemical vapor deposition of tungsten for microdynamic structures. In *Proceedings of the IEEE Micro Electro Mechanical Systems Workshop*, pages 82–87, Salt Lake City, UT, February 20–22, 1989.

[14] K. E. Crowe. Determination of mechanical properties of LPCVD silicon nitride thin films. Master's thesis, Massachusetts Institute of Technology, Cambridge, MA, 1988.

[15] T. W. Dakin, G. Luxa, G. Oppermann, J. Vigreux, G. Wind, and H. Winkelnkemper. Breakdown of gases in uniform fields: Paschen curves for nitrogen, air and sulfur hexaflouride. *Electra*, 32:61–82, 1974.

[16] K. Deng, V. R. Dhuler, M. Mehregany, and E. W. Jansen. Measurement of micromotor dynamics in lubricating fluids. In *Proceedings of IEEE Micro Electro Mechanical Systems*, pages 260–264, Ft. Lauderdale, FL, Feb. 1993.

[17] K. Deng, W. H. Ko, and G. M. Michal. A preliminary study on friction measurements in MEMS. In *Transducers*, pages 213–216, San Francisco, CA, June 4–7, 1991.

[18] K. Deng, M. Mehregany, and A. S. Dewa. A simple fabrication process for polysilicon side–drive micromotors. *IEEE Journal of Microelectromechanical Systems*, 3(4):126–133, Dec. 1994.

[19] V. Dhuler, M. Mehregany, and S. M. Phillips. Micromotor operation in a liquid environment. In *Technical Digest of the IEEE Solid-State Sensor and Actuator Workshop*, Hilton Head, SC, June 1992.

[20] C. D. Ellis, D. A. Jaworske, R. Ramesham, and T. Roppel. Polycrystalline diamond film flow sensor. In *Proceedings of the IEEE CH2783-9*, 1990.

[21] M. Esashi, S. Shoji, Y. Matsumoto, and K. Furuta. Catheter-tip capacitive pressure transducer. *Electronics and Communication in Japan, Part 2*, 73(10):79–87, 1990.

[22] M. Esashi, S. Shoji, T. Wada, and T. Nagata. Capacitive absolute pressure sensors with hybrid structure. *Electronics and Communication in Japan, Part 2*, 74(4):67–75, 1991.

[23] L. S. Fan. *Integrated Micromachinery — Moving Structures on Silicon Chips*. PhD thesis, University of California, Berkeley, CA, 1990.

[24] L. S. Fan, Y. C. Tai, and R. S. Muller. IC–processed electrostatic micro–motors. In *Technical Digest, IEEE International Electron Devices Meeting*, pages 666–669, San Francisco, CA, December 11–14, 1988.

[25] L. S. Fan, Y. C. Tai, and R. S. Muller. Integrated movable micromechanical structures for sensors and actuators. *IEEE Trans. on Electron Devices*, 35(6):724–730, June 1988.

[26] L. S. Fan, Y. C. Tai, and R. S. Muller. IC–processed electrostatic micromotors. *Sensors and Actuators*, 20(1/2):41–47, 1989.

[27] L. S. Fan and S. Woodman. Batch fabrication of mechanical platforms for high density data storage. In *The 8th International Conference on Solid-State Sensors and Actuators / Eurosensors IX*, pages 434–437, Stockholm, Sweden, June 25–29 1995.

[28] N. J. Felici. Developments in regard to electrostatic generators for direct current. *Direct Current*, pages 122–130, June 1953.

[29] A. M. Flynn, L. S. Tavrow, S. F. Bart, R. A. Brooks, D. Ehrlich, K. R. Udayakumar, and L. E. Cross. Piezoelectric micromotors for microrobots. *IEEE Journal of Microelectromechanical Systems*, 1(1):44–51, Mar. 1992.

[30] C. G. Fonstad. *Microelectronic Devices and Circuits.* McGraw-Hill, New York, 1994.

[31] K. J. Gabriel, F. Behi, R. Mahadevan, and M. Mehregany. *In Situ* friction and wear measurements in integrated polysilicon mechanisms. *Sensors and Actuators*, A21:184–188, 1990.

[32] S. K. Ghandi. *VLSI fabrication principles: Silicon and Gallium Arsenide.* John Wiley and Sons, Inc., New York, 1983.

[33] H. Guckel, D. W. Burns, C. R. Rutigliano, D. K. Showers, and J. Uglow. Fine grained polysilicon and its application to planar pressure transducers. In *Technical Digest of the 4th International Conference on Solid-State Sensors and Actuators*, pages 277–282, Tokyo, Japan, June 2–5 1987.

[34] H. Guckel, T. R. Christenson, K. J. Skrobis, T. S. Jung, J. Klein, K. V. Hartojo, and I. Widjaja. A first functional current excited planar rotational magnetic micromotor. In *Proceedings of the IEEE Micro Electro Mechanical Systems Workshop*, pages 7–11, Fort Lauderdale, FL, 1993.

[35] H. Guckel, T. Randazzo, and D. W. Burns. A simple technique for the determination of mechanical strain in thin films with applications to polysilicon. *J. Appl. Phys.*, 57:1671–1675, 1985.

[36] H. Guckel, J. J. Sniegowski, and T. R. Christenson. Fabrication of micromechanical devices from polysilicon films with smooth surfaces. *Sensors and Actuators*, 20:117–122, 1989.

[37] W. D. Harris and J. H. Lang. A simple motion estimator for variable reluctance motors. *IEEE Transactions on Industry Applications*, 26:237–243, Mar. 1990.

[38] K. Hjort, J.-A. Schweitz, and B. Hök. Bulk and surface micromachining of GaAs structures. In *Proceedings of the 3rd IEEE Workshop on Micro Electro Mechanical Systems*, pages 73–76, Napa Valley, CA, 1990.

[39] C. Ho, J. D. Plummer, S. E. Hansen, and R. W. Dutton. VLSI process modeling — SUPREM-III. *IEEE Trans. Electron Devices*, ED-30(11):1438–1452, Nov. 1983.

[40] R. T. Howe and R. S. Muller. Polycrystalline and amorphous silicon micromechanical beams: annealing and mechanical properties. *Sensors and Actuators*, 4:447–454, 1983.

[41] R. T. Howe and R. S. Muller. Polycrystalline silicon microstructures. *J. Electrochem. Soc.*, 130:1420–1423, 1983.

[42] R. T. Howe and R. S. Muller. Resonant-microbridge vapor sensor. *IEEE Trans. on Electron Devices*, ED-33(4):499–506, 1986.

[43] O. D. Jefimenko. Electrostatic motors. In A. D. Moore, editor, *Electrostatics and its Applications*, chapter 7, pages 131–147. John Wiley and Sons, Inc., New York, 1973.

[44] H. Jiang and W. N. Carr. On-chip integration of high voltage generator circuits for an electrostatic micromotor. In *The 8th International Conference on Solid-State Sensors and Actuators / Eurosensors IX*, pages 150–153, Stockholm, Sweden, June 25–29 1995.

[45] L. A. Jones and J. H. Lang. A state observer for the permanent magnet synchronous motor. *IEEE Transactions on Industrial Electronics*, 36:374–382, Aug. 1989.

[46] J. T. Kung and H.-S. Lee. An integrated air–gap–capacitor pressure sensor and digital readout with sub–100 attofarad resolution. *IEEE Journal of Microelectromechanical Systems*, 1(3):121–129, Sept. 1992.

[47] J. H. Lang. Initial thoughts on the dynamics and control of electric micromotors. In *Proceedings of the 3rd Toyota Conference*, pages 9.1–9.14, Aichi-ken, Japan, Oct. 1989.

[48] M. W. Layland. Generalized electrostatic machine theory. *Proc. IEE*, 116:403–405, 1969.

[49] T. P. Lee and T. Li. Photodetectors. In S. E. Miller and A. G. Chynoweth, editors, *Optical Fiber Telecommunications*, pages 593–626. Academic Press, New York, 1979.

[50] R. Legtenberg, E. Berenschot, J. van Baar, T. Lammerink, and M. Elwenspoek. An electrostatic lower stator axial gap wobble motor: Design and fabrication. In *The 8th International Conference on Solid-State Sensors and Actuators / Eurosensors IX*, pages 104–107, Stockholm, Sweden, June 25–29 1995.

[51] D. G. Leip. Design and implementation of a capacitive measurement circuit with application to integrated micromotor position sensing. Master's thesis, Massachusetts Institute of Technology, Cambridge, MA, 1994.

[52] W. Leonhard. Micromotor control of high dynamic performance ac–drives – a survey. *Automatica*, 22(1):1–19, 1986.

[53] M. G. Lim, J. C. Chang, D. P. Schultz, R. T. Howe, and R. M. White. Polysilicon microstructures to characterize static friction. In *Proceedings of the IEEE Micro Electro Mechanical Systems Workshop*, pages 82–88, Napa Valley, CA, February 11–14, 1990.

[54] T. A. Lober. A microfabricated electrostatic motor design and process. Master's thesis, Massachusetts Institute of Technology, Cambridge, MA, 1988.

[55] T. A. Lober and R. T. Howe. Surface–micromachining processes for electrostatic microactuator fabrication. In *Technical Digest of the IEEE Solid-State Sensor and Actuator Workshop*, pages 59–62, Hilton Head Island, SC, June 6–9, 1988.

[56] T. A. Lober, J. Huang, M. A. Schmidt, and S. D. Senturia. Characterization of the mechanisms producing bending moments in polysilicon micro–cantilever beams by interferometric deflection measurements. In *Technical Digest of the IEEE Solid–State Sensor and Actuator Workshop*, pages 92–95, Hilton Head Island, SC, June 6–9, 1988.

[57] Machine Design: 1990 Systems Design Reference Volume. *Bearings and lubricants*, June 1990.

[58] V. M. McNeil. *A Thin-Film Silicon Microaccelerometer Fabricated Using Electrochemical Etch-Stop and Wafer Bonding Technology.* PhD thesis, Massachusetts Institute of Technology, Cambridge, MA, 1994.

[59] M. Mehregany. *Microfabricated Silicon Electric Mechanisms.* PhD thesis, Massachusetts Institute of Technology, Cambridge, MA, 1990.

[60] M. Mehregany, S. F. Bart, L. S. Tavrow, J. H. Lang, and S. D. Senturia. Principles in design and microfabrication of variable–capacitance side–drive motors. *Journal of Vacuum Science and Technology*, A 8(4):3614–3624, Jul–Aug 1990.

[61] M. Mehregany, S. F. Bart, L. S. Tavrow, J. H. Lang, S. D. Senturia, and M. F. Schlecht. A study of three microfabricated variable–capacitance motors. *Sensors and Actuators*, A21:173–179, 1990.

[62] M. Mehregany and V. R. Dhuler. Operation of electric micromotors in liquid environments. *J. Micromech. Microeng.*, 2:1–3, Feb. 1992.

[63] M. Mehregany, K. J. Gabriel, and W. S. N. Trimmer. Integrated fabrication of polysilicon mechanisms. *IEEE Trans. on Electron Devices*, 35(6):719–723, June 1988.

[64] M. Mehregany, P. Nagarkar, S. D. Senturia, and J. H. Lang. Operation of microfabricated harmonic and ordinary side–drive motors. In *Proceedings of the 3rd IEEE Workshop on Micro Electro Mechanical Systems*, pages 1–8, Napa Valley, CA, 1990.

[65] M. Mehregany, S. D. Senturia, and J. H. Lang. Friction and wear in microfabricated harmonic side–drive motors. In *Technical Digest of the IEEE Solid-State Sensor and Actuator Workshop*, pages 17–22, Hilton Head Island, SC, June 4–7, 1990.

[66] M. Mehregany, S. D. Senturia, and J. H. Lang. Measurement of wear in polysilicon micromotors. *IEEE Trans. on Electron Devices*, ED–39(5):1136–1143, May 1992.

[67] M. Mehregany, S. D. Senturia, J. H. Lang, and P. Nagarkar. Micromotor fabrication. *IEEE Trans. on Electron Devices*, ED–39(9):2060–2069, Sept. 1992.

[68] K. Nabors, S. Kim, J. White, , and S. Senturia. Fast capacitance extraction of general three-dimentional structures. In *Proc. Int. Conf. Comput. Design*, Cambridge, MA, October 1991.

[69] H. C. Nathanson, W. E. Newell, R. A. Wickstrom, and J. John R. Davis. The resonant gate transistor. *IEEE Trans. on Electron Devices*, ED–14(3):117–133, 1967.

[70] A. Padmanabhan, H. D. Goldberg, K. S. Brewer, and M. A. Schmidt. A silicon micromachined floating-element shear-stress sensor with optical position sensing by photodiodes. In *The 8th International Conference on Solid-State Sensors and Actuators / Eurosensors IX*, pages 436–439, Stockholm, Sweden, June 25–29 1995.

[71] L. Paratte, H. Lorenz, R. Luthier, R. Clavel, and N. F. de Rooij. Miniature gear reduction unit driven by a silicon electrostatic wobble motor. In *Micro Electro Mechanical Systems*, Oiso, Japan, Jan 25–28, 1994.

[72] F. Paschen. Ueber die zum Funkenübergang in Luft, Wasserstoff und Kohlensäure bei verschiedenen Drucken erforderliche Potentialdifferenz. *Annalen der Physik*, 37:69–96, 1889.

[73] K. E. Petersen. Silicon as a mechanical material. *Proc. IEEE*, 70(5):420–457, May 1982.

[74] K. E. Petersen, J. Brown, and W. Renken. High–precision, high–performance mass flow sensor with integrated laminar flow microchannels. In *Proc. of Int. Conf. on Solid–State Sensors and Actuators*, page 361, Philadelphia, PA, June 1985.

[75] L. Roylance and J. Angell. A batch-fabricated silicon accelerometer. *IEEE Trans. on Electron Devices*, ED–26(12):1911–1917, Dec. 1979.

[76] C. S. Sander, J. W. Knuth, and J. D. Meindl. A monolithic capacitive pressure sensor with pulsed–period output. *IEEE Trans. on Electron Devices*, ED–27(5):927–930, May 1980.

[77] M. A. Schmidt, R. T. Howe, S. D. Senturia, and J. H. Haritonidis. Surface micromachining of polyimide/metal composites for a shear–stress sensor. In *IEEE Micro Robots and Teleoperators Workshop*, Hyannis, MA, 1987.

[78] M. A. Schmidt, R. T. Howe, S. D. Senturia, and J. H. Haritonidis. Design and calibration of a microfabricated floating–element shear–stress sensor. *IEEE Trans. on Electron Devices*, 35(6):750–757, 1988.

[79] D. H. Staelin, A. W. Morgenthaler, and J. A. Kong. *Electromagnetic Waves*, pages 230–234. Prentice–Hall, Inc., Englewood Cliffs, NJ, 1994.

[80] S. M. Sze. *Physics of Semiconductor Devices.* John Wiley and Sons, Inc., New York, second edition, 1981.

[81] Y. C. Tai. *IC–processed Polysilicon Micromechanics: Technology, Material, and Devices.* PhD thesis, University of California, Berkeley, CA, 1989.

[82] Y. C. Tai, L. S. Fan, and R. S. Muller. IC–processed micro-motors: Design, technology, and testing. In *Proceedings of the IEEE Micro Electro Mechanical Systems Workshop*, pages 1–6, Salt Lake City, UT, February 20–22, 1989.

[83] Y. C. Tai and R. S. Muller. IC–processed electrostatic synchronous micromotors. *Sensors and Actuators*, 20(1/2):49–55, 1989.

[84] Y.-C. Tai and R. S. Muller. Frictional study of IC–processed micromotors. *Sensors and Actuators A*, 21:180–183, 1990.

[85] H. Tanigawa, T. Ishihara, M. Hirata, and K. Suzuki. MOS integrated silicon pressure sensor. *IEEE Trans. on Electron Devices*, ED–32:1191–1195, 1985.

[86] L. S. Tavrow. Microfabricated electric motors. *Electrical Manufacturing*, pages 23–28, May 1990.

[87] L. S. Tavrow. *A LOCOS-Based Microfabricated Radial-Gap Electric Motor.* PhD thesis, Massachusetts Institute of Technology, Cambridge, MA, 1991.

[88] L. S. Tavrow, S. F. Bart, J. H. Lang, and M. F. Schlecht. A LOCOS process for an electrostatic microfabricated motor. *Sensors and Actuators*, A21:893–898, 1990.

[89] P. K. Tedrow and C. G. Sodini. MIT twin well CMOS process. *Microsystems Techology Laboratories, Massachusetts Institute of Technology*, July 1993. Version 1.3.

[90] The Timkin Company: Bearing Selection Handbook. *Bearings life*, 1986.

[91] W. S. N. Trimmer and K. J. Gabriel. Design considerations for a practical electrostatic micro-motor. *Sensors and Actuators*, 11(2):189–206, 1987.

[92] J. G. Trump. *Vacuum Electrostatic Engineering.* PhD thesis, Massachusetts Institute of Technology, 1933.

[93] G. C. Verghese, J. H. Lang, and L. F. Casey. Analysis of instability in electrical machines. *IEEE Transactions on Industry Applications*, 22(5):853–864, 1986.

[94] A. R. von Hippel. *Molecular Science and Molecular Engineering.* John Wiley and Sons, Inc., New York, 1959.

[95] A. A. Yasseen, S. W. Smith, and M. M. F. L. Merat. Diffraction grating scanners using polysilicon micromotors. In *Proceedings of the IEEE Workshop on Micro Electro Mechanical Systems*, pages 175–180, Amsterdam, the Netherlands, 1995.